International Journal of Comprehensive Engineering

ISSN 2186-2680

Volume 2, Number 1, March 2013

IJCE

Published by
International Association of Comprehensive Engineering (IACE)

http://www.iace-journal.org/

Printed by
Diagnosis Engineering & Technology Corp., Japan

========== International Journal of Comprehensive Engineering (IJCE) ==========

International Journal of Comprehensive Engineering (IJCE) is an international interdisciplinary journal that integrates publication from aspects of research on engineering science. This journal provides a medium of communication among engineers and scientists who have engaged in research and development concerning the fields of comprehensive engineering, while maintaining a healthy balance between fundamental and experimental topics. Now, the journal has three separate fields, the scopes of which are Part A: Maintenance Engineering; Part B: Intelligent Engineering; Part C: Engineering in Agriculture, Ocean and Light Industry shown in flows, and other specialized fields will also be updated in the near future.

Part A: Maintenance Engineering

Topics of interest for submission on the field of maintenance engineering include, but are not limited to:
Condition Diagnosis Engineering and Technology; Sensing Technology; Maintenance Management; Fault Tolerant System; Fault Self-Recovery Engineering; E-Maintenance; Signal Processing; Risk, Health and Safety Management; Structural Health Monitoring; Information and Communication Technology; Data and Information Fusion; Reliability/Quality; Maintenance Robot; Data Quality and Acquisition; Human Factors; Education and Training; Risk Based Engineering; Others on Maintenance.

Part B: Intelligent Engineering

Topics of interest for submission on the field of intelligent engineering include, but are not limited to:
Application of Artificial Intelligence in Engineering; Intelligent Design, Modeling, Planning and Control for Applied Engineering; Intelligent Robot System; Intelligent Fault Diagnosis; Intelligent Signal Processing for Applied Engineering; Others on Intelligent Engineering.

Part C: Engineering in Agriculture, Ocean and Light Industry

Topics of interest for submission on the field of engineering in agriculture, ocean and light industry include, but are not limited to:
Agriculture Engineering: Agricultural Equipment and Mechanical Engineering; Agricultural Bioenvironmental Engineering; Agricultural Renewable Energy Engineering; Agricultural Produce Processing Engineering; Agricultural Information and Electrical Technologies; Others on Agricultural Engineering.
Ocean Engineering: New Ocean Energy; Ocean Maintenance Technology; Ocean Monitoring Technology; Ocean Diagnosis Method; Ocean Experimental Development; Professional Sensor Technology; Observational and Computational Tools Others on Ocean Engineering.
Light Industry Engineering: Agri-food Products Processing/Packaging Technology and Equipment; Comprehensive Utilization of Resource; Preservation; Storage and Packaging of Agri-food Products; Innovative IT Applications in Agri-food Chain; Sensing, Testing, Automation and Internet of Things Technologies; Green Environmental Protection; Energy Saving Technologies; Others on Light Industry.

========== Manuscript Submission ==========

Manuscripts should be submitted online at http://www.iace-journal.org/ by registering and logging in to the website of the IJCE. Once you have registered, please click the “Submit Manuscript” to go to the submission from. Please use the MS Word template file to prepare your manuscript. Manuscript prepared in MS Word must be converted into a single file before submission. The Microsoft Word template file can be downloaded from the website of the IJCE.

========== Submission Declaration ==========

The submission, such as articles, reviews, technical report etc., to the IJCE means these facts that the work described has not been published previously, that it is not under consideration for publication elsewhere, that its publication is approved by all authors and tacitly or explicitly by the responsible authorities where the work was carried out, and that, if accepted, it will not be published elsewhere including electronically in the same form, in English or in any other language, without the written consent of the copyright-holder.

========== Copyright ==========

Authors will be asked to complete a "Copyright Transfer Statement", when submitting the manuscript. Acceptance of the agreement will ensure the widest possible dissemination of information. Permission of the publisher is required for resale or distribution outside the institution and for all other derivative works, including compilations and translations. The "Copyright Transfer Statement" can be downloaded from the website of the IJCE as follows:
http://www.iace-journal.org/views/Copyright_Transfer_Statement.pdf.

========== Review Policy ==========

The following types of contribution to the IJCE are peer-reviewed: Articles, Reviews and Technical Reports. The articles accepted for publishing in the IJCE include regular paper and letter, which will be decided by editors according the reviewing results. All forms of published correction may also be peer-reviewed at the discretion of the editors. Other contributed types to the IJCE, particularly if they present technical information, may be peer-reviewed at the discretion of the editors. For any general questions and comments about the peer-review process, the journal or its editorial policies that are not mentioned here, please contact us using the email: ijce@nifty.com. Questions about a specific submitted manuscript should be directed to the executive editor who is handling the manuscript.

International Journal of Comprehensive Engineering (IJCE)

Volume 2, Number 1, March 2013 (ISSN 2186-2680)

International Journal of Comprehensive Engineering
Part A, 2(1), 1-10, 2013
Doi: 10.14270/IJCE2013.2.1.a1
Regular paper

ISSN 2186-2680
e-ISSN 2186-2656
www.iace-journal.org

Intelligent Diagnosis Method for Rotating Machinery Using Relative Ratio Symptom Parameters and Fuzzy Neural Network

Ke Li [1], Hao Sun [1], Peng Chen [2, #] and Huaqing Wang [3]

[1] School of Mechanical Engineering, Jiangnan University, 1800 Li Hu Avenue, Wuxi, Jiangsu Province, 214122, China
[2] Department of Environmental Science and Engineering, Faculty of Bioresources, Mie University, 1577 Kurimamachiya-cho, Tsu-shi, Mie-ken, 514-8507, Japan
[3]School of Mechanical & Electrical Engineering, Beijing University of Chemical Technology, Beijing, 100029, China

[#] Corresponding author: chen@bio.mie-u.ac.jp; Tel.: +81-59-2329592; Fax: +81-59-2329592

Abstract: This paper proposes a sequential diagnosis method for rotating machinery using the fuzzy neural network called Partially-Linearized Neural Network (PLNN) and relative ratio symptom parameters (RRSPs) in frequency domain, by which the fault types of rotating machinery can be precisely diagnosed on the basis of probability distribution of the RRSPs. The RRSPs in frequency domain are defined for reflecting the features of time signals measured in each state of rotating machinery. Sensitive evaluation method for selecting good symptom parameters using principal component analysis (PCA) is also proposed for detecting and distinguishing faults in rotating machinery. The practical examples of fault diagnosis for misalignment state (M), unbalance state (UN) and looseness state (L) of a rotating shaft verify the effectiveness of the method proposed in this paper.

Keywords: Sequential Diagnosis, Fuzzy Neural Network, Relative Ratio Symptom Parameters, Principal Component Analysis

Received: Apr. 25,2012 / Accepted: Nov. 6,2012 / Published: Apr. 8,2013

1. Introduction

In the field of machinery diagnosis, vibration signals are often used for fault detection and state discrimination. Machinery diagnosis depends largely on the feature analysis of vibration signals measured for condition diagnosis. If we can find good symptom parameters which sensitively reflect the feature of the machine state, automatic diagnosis for mechanical failure is possible [1-2]. However, the feature extraction for the fault diagnosis is difficult since the vibration signals measured at a point of the machine often contains strong noise. Stronger noise than the actual failure signal may lead to misrecognition of useful information for diagnosis. Moreover, because there are a lot of ambiguous relationships between symptom parameters and failure types of plant machinery, failure types of plant machinery cannot be easily identified [3-5]. Many studies have been carried out to investigate the use of neural networks (NNs) for automatic diagnosis of machinery. Most of these methods have been proposed to deal with discrimination of fault types collectively. However, the conventional NN cannot reflect the possibility of ambiguous diagnosis problems, and will never converge when the first layer symptom parameters have the same values in different states [6].

Structural faults, such as misalignment (M), unbalance (UN) and looseness (L) etc., are often occurring in a shaft of rotating machinery. These faults may cause serious machine accidents and bring great production losses. Because the feature spectra of structural faults are resemble closely in low frequency area, they are difficult to be automatically distinguished each other.

For the above reasons, in order to automatically identify the states of rotating machinery in structural faults, this paper proposed a sequential diagnosis method for rotating machinery using the fuzzy neural network called Partially-Linearized Neural Network (PLNN) and relative ratio symptom parameters (RRSPs) in frequency domain, by which the fault types of rotating machinery can be precisely diagnosed on the basis of probability distribution of the RRSPs. The RRSPs in frequency domain are defined for reflecting the features of time signals measured in each state of rotating machinery. Moreover, the principal component analysis (PCA) is also proposed to evaluate the sensitivity of RRSPs for detecting faults. The practical examples of fault diagnosis are provided to verify the effectiveness of the proposed method. The results verify that the faults that often occur in a rotating shaft, such as misalignment state (M), unbalance state (UN) and looseness state (L) are effectively identified by the proposed method.

2. Experimental System for Fault Diagnosis

Fig.1 shows the rotating machinery for diagnosis test, the three accelerometers (PCB MA352A60) with a bandwidth from 5 Hz to 60 kHz and 10 mV/g output were used to measure the vibration signals of the horizontal, vertical and shaft directions in the normal (N), unbalance (UN), misalignment (M) and looseness (L) states, respectively. The vibration signals measured by the accelerometers were transformed into the signal recorder (Scope Coder DL750) after being magnified by the sensor signal conditioner (PCB ICP Model 480C02). The original vibration signals in time domain are shown in Fig. 2. These signals were measured at a constant speed (800 rpm). The sampling frequency of the signal measurement was 5 kHz, and the sampling time was 20 s.

(a)

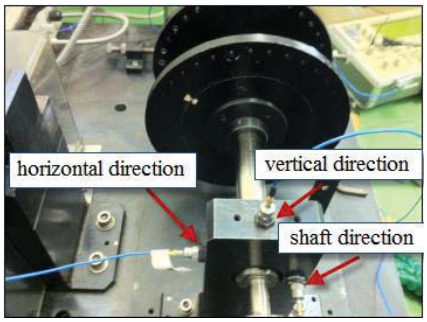

(b)

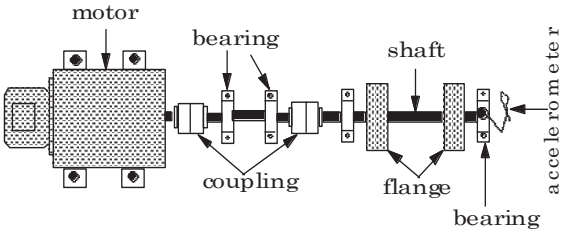

Fig. 1 Experimental equipment for fault diagnosis (a) Illustrate of the rotating machinery, (b) Inspection location

3. Relative Ratio Symptom Parameters for Fault Diagnosis

Many symptom parameters have been defined in the pattern recognition field, in this paper through analyzing the spectral features of structural faults of rotating machinery, the nine RRSPs in the low-frequency domain for structural faults diagnosis of rotating machinery are defined:

$$P_1 = \frac{P_d(f_r) \Big/ \sum_{i=2}^{20} P_d(i \cdot f_r)}{P_n(f_r) \Big/ \sum_{i=2}^{20} {}_n(i \cdot f_r)} \tag{1}$$

$$P_2 = \frac{P_d(2f_r)/P_d(f_r)}{P_n(2f_r)/P_n(f_r)} \tag{2}$$

$$P_3 = \frac{P_d(3f_r)/P_d(f_r)}{P_n(3f_r)/P_n(f_r)} \tag{3}$$

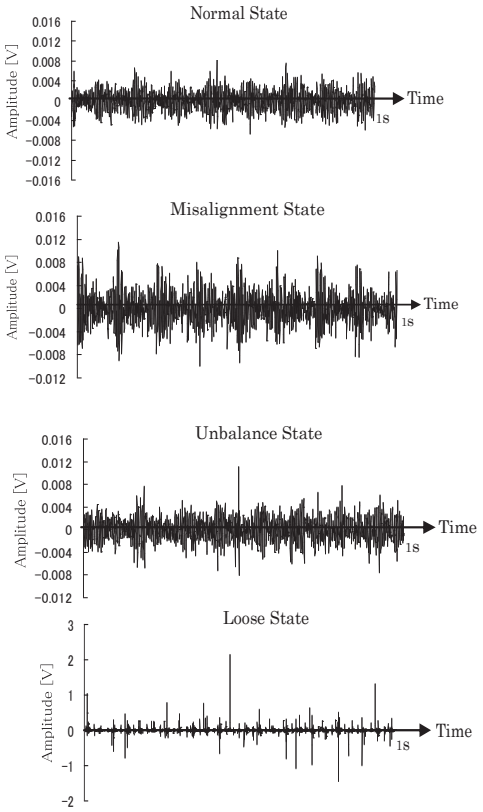

Fig. 2 Original signals in each state

$$P_4 = \frac{\sum_{i=4}^{10} P_d(i \cdot f_r) \Big/ P_d(f_r)}{\sum_{i=4}^{10} P_n(i \cdot f_r) \Big/ P_n(f_r)} \tag{4}$$

Here, f_r is the rotating frequency. $P_n(f_r)$ and $P_d(f_r)$ are the spectrum value at f_r in normal state and abnormal state respectively, $P_n(if_r)$ and $P_d(if_r)$ are the high-order harmonic spectrum value at if_r in normal and abnormal state respectively.

$$P_5 = \frac{\sum_{i \neq i \cdot f_r}^{f_i > 6 f_r} P_d(f_i) \Big/ \sum_{i=1}^{6} P_d(i \cdot f_r)}{\sum_{i \neq i \cdot f_r}^{f_i > 6 f_r} P_n(f_i) \Big/ \sum_{i=1}^{6} P_n(i \cdot f_r)} \tag{5}$$

$$P_6 = \frac{\sum_{>0.6kH}^{<1.5kH} P_d(f) \Big/ \sum_{<0.6kH} P_d(f)}{\sum_{>0.6kH}^{<1.5kH} P_n(f) \Big/ \sum_{<0.6kH} P_n(f)} \tag{6}$$

$$P_7 = \frac{A_{ad}/A_{rd}}{A_{an}/A_{rn}} \tag{7}$$

Here, A_{an} and A_{rn} are the vibration level of shaft direction and radial direction in normal state, respectively, A_{ad} and A_{ad} are the vibration level of shaft direction and radial direction in abnormal state respectively. (vibration level is standard deviation or root mean square value .etc)

$$P_8 = \frac{A_{vd} / A_{hd}}{A_{vn} / A_{hn}} \tag{8}$$

Here, A_{vn} and A_{hn} are the vibration level of vertical direction and horizontal direction in normal state, respectively, A_{vd} and A_{hd} are the vibration level of vertical direction and horizontal direction in abnormal state respectively.

$$P_9 = \beta_d - \beta_n \tag{9}$$

Here, β_n and β_d are the skewness in normal state and abnormal state respectively, and

$$\beta = \frac{\sum_{i=1}^{I} (f_i - \bar{f})^3 \cdot P(f_i)}{\sigma^3 I} \tag{10}$$

I is the number of spectrum line, f_i is frequency and from 0Hz to the maximum analysis frequency, $\bar{f}$ is mean value of the analysis frequency, and

$$\bar{f} = \frac{\sum_{i=1}^{I} f_i \cdot P(f_i)}{\sum_{i=1}^{I} P(f_i)}, \tag{11}$$

σ is standard deviation ， and

$$\sigma = \sqrt{\frac{\sum_{i=1}^{I} (f_i - \bar{f})^2 \cdot P(f_i)}{I}} \tag{12}$$

4. Method of Selecting Good Symptom Parameters

4.1 Sequential Condition Diagnosis Approach

In most practical cases of plant, it is difficult to establish accurate mathematic models of fault states for machinery diagnosis because the fault mechanisms of machinery and the features of fault types cannot be perfectly clarified by a theoretical approach. In addition, due to the complexity of plant machinery conditions, it is very hard to find out one or a few symptom parameters that can perfectly identify all faults simultaneously.

In order to solve these problems, a sequential fuzzy diagnosis method is considered. An example of the sequential diagnosis is shown in Fig.3. In this case, a machine in misalignment state (M), unbalance state (UN) and looseness state (L) should be identified sequentially. The inference of sequential diagnosis is follows.

In the first step, if the possibility grades of normal state (N) and abnormal state (A) are g_N and g_A respectively, and $g_N > g_A$, then the state is judged as normal state (N), else proceed to next step.

In the second step, if the possibility grades of misalignment state (M) and another fault state (UA) are g_M and g_{UA} respectively, and $g_M > g_{UA}$, then the state is judged as misalignment state (M), else proceed to next step.

In the third step, if the possibility grades of unbalance state (UN) and another fault state (UA) are g_{UN} and g_{UA} respectively, and $g_{UN} > g_{UA}$, then the state is judged as unbalance state (UN), else proceed to next step.

In the fourth step, if the possibility grades of looseness state (L) and another fault state (UA) are g_L and g_{UA} respectively, and $g_L > g_{UA}$, then the state is judged as looseness state (L), else it will be judged as unknown abnormal state (UA) .

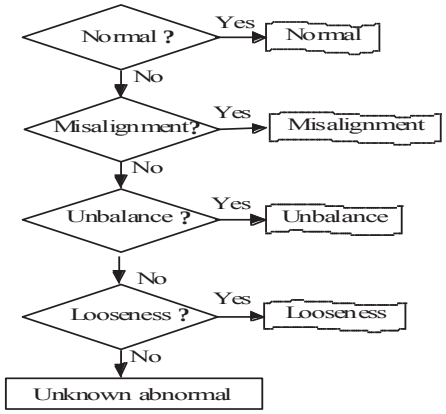

Fig. 3 Flow chart of sequential inference

4.2 Principal Component Analysis (PCA) for Selecting Symptom Parameters

PCA is a mathematical procedure that uses an orthogonal transformation to convert a set of observations of possibly correlated variables into a set of values of uncorrelated variables called principal components. PCA was invented in 1901 by Karl Pearson. Now it is mostly used as a tool in exploratory data analysis and for making predictive models. PCA can be done by eigenvalue decomposition of a data covariance matrix or the singular value decomposition of a data matrix. These decompositions are usually performed after mean centering the data for each attribute. The results of a PCA are usually discussed in terms of component scores and loadings [7]. In the last few years, PCA has been applied to process fault diagnosis (identification) [8-10].

Define a data matrix with size m x n, where m is the number of identifying states and n is the number of symptom parameters, whose covariance matrix has eigenvalue λ_i and eigenvector a_i and i=1-n with $\lambda_1 \geq \lambda_2 \geq \ldots \geq \lambda_n$. Principal components Z_i and the cumulative contribution rate of the principal components η_i can be calculated as follows:

$$\begin{Bmatrix} Z_1 \\ \vdots \\ Z_n \end{Bmatrix} = \begin{bmatrix} a_{11} & \cdots & a_{1n} \\ \vdots & \ddots & \vdots \\ a_{m1} & \cdots & a_{mn} \end{bmatrix} \begin{Bmatrix} P_1 \\ \vdots \\ P_n \end{Bmatrix} = AP \tag{13}$$

$$\eta_i = \frac{\sum_{j=1}^{i} \lambda_j}{\sum_{k=1}^{n} \lambda_k} \tag{14}$$

Where λ_i is the standard deviation of the principal component, a_{ji} is the weight coefficient of the principal component, P_i is a symptom parameter, i=1-n and j=1-m.

Using PCA, original data can be converted into many principal components. The first few principal components contain most of the information and the discriminatory features. The weight coefficient of the principal components can express the importance of the symptom parameters for each principal component. Therefore, the symptom parameters that have high sensitivity for detecting faults can be selected by the weight coefficient for the first few principal components.

In this study, the two best RRSPs that contain the most information and have high sensitivity for each step of the sequential diagnosis are selected by PCA, as shown in Formula13. As an example, parts of the selection results are shown in Table 1. In the first step, P_2 and P_4 are better for distinguishing the normal state (N) and the abnormal states (A). Because the weight coefficients for P_2 and P_4, the first principal component, are larger than those of the other, the contribution rate of the first principal component is 0.88, which contains enough information and discriminatory features to identify the normal state (N) and the abnormal states (A). Similarly, the RRSPs for other diagnostic steps can also be selected.

Table 1 Selection of the RRSPs for each step of sequential diagnosis

	Weight coefficients for each symptom parameter									η_1	Selection results
	P_1	P_2	P_3	P_4	P_5	P_6	P_7	P_8	P_9		
Weight coefficients for the first diagnosis step											
N:M	-0.61	**0.9**	1.0	**0.99**	-1.0	-1.0	0.77	-1.0	-0.87	0.88	
N:UN	-0.65	**1.0**	-0.8	**0.98**	-1.0	0.75	0.69	-1.0	-0.69	0.89	P_2, P_4
N:L	0.99	**0.82**	-0.82	**0.98**	-1.0	-0.9	-1.0	0.65	0.72	0.9	
Weight coefficients for the second diagnosis step											
M:UN	**1.0**	0.89	-1.0	**1.0**	0.69	-0.88	1.0	-0.99	-0.69	0.88	P_1, P_4
M:L	**0.85**	0.80	1.0	**0.99**	-0.91	-0.75	-0.82	0.67	-1.0	0.85	
Weight coefficients for the third diagnosis step											
UN:M	1.0	**0.89**	-1.0	1.0	0.69	-0.88	**1.0**	-0.99	-0.69	0.88	P_2, P_7
UN:L	-1.0	**1.0**	0.66	0.81	-0.78	-0.91	**0.98**	-0.99	0.78	0.91	
Weight coefficients for the fourth diagnosis step											
L:M	0.85	**0.80**	1.0	**0.99**	-0.91	-0.75	-0.82	0.67	-1.0	0.85	P_2, P_4
L:UN	-1.0	**1.0**	0.66	**0.81**	-0.78	-0.91	0.98	-0.99	0.78	0.91	

5. Fuzzy Neural Network

5.1 Partially-linearized neural network (PLNN)

The fuzzy neural network is applied to diagnose the fault types of a machine by the sequential diagnosis algorithm, and realized with a developed back propagation neural network called as the partially-linearized neural network (PLNN) [11-14]. A traditional neural network (NN) is only used for training the non-ambiguous data, and the PLNN can be used for dealing with ambiguous data. Here, the basic principle of the PNN for the fault diagnosis is described as follows.

The neuron number of the *m*-th layer of an NN is N_m. The set $X^{(1)}=\{X_i^{(1,j)}\}$ represents the pattern input to the 1st layer and the set $X^{(M)}=\{X_i^{(M,k)}\}$ is the training data for the last layer (*M*-th layer). Here, $i=1\ to\ P$, $j=1\ to\ N_1$, $k=1\ to\ N_M$, and, $X_i^{(1,j)}$: the value input to the *j*-th neuron in the input (1st) layer; $X_i^{(M,k)}$: the output value of the *k*-th neuron in the output (*M*-th) layer, $k=1\ to\ N_M$.

Even if the NN converges by learning $X^{(1)}$ and $X^{(M)}$, it cannot adequately deal with the ambiguous relationship between the new $X^{(1)*}$ and $X^{(M)*}$, which has not been learnt. In order to predict $X^{(M)*}$ according to the probability distribution of $X^{(1)*}$, partial linear interpolation of the NN is introduced as shown in Fig.4.

In the NN that has converged with the data $X^{(1)}$ and $X^{(M)}$, the following symbols are used.

$X_i^{(m,t)}$: the value of the *t*-th neuron in the hidden (*m*-th) layer, $t=1\ to\ N_m$;

$W_{uv}^{(m)}$: the weight between the *u*-th neuron in the *m*-th layer and the *v*-th neuron in the (*m+1*)-th layer, $m=1\ to\ M; u=1\ to\ N_m; v=1\ to\ N_{m+1}$.

If all these values are memorized by the computer, when new values $X_j^{(1,u)*}$ ($X_j^{(1,u)}<X_j^{(1,u)*}<X_{j+1}^{(1,u)}$) are input into the first layer, the predicted value of the *v*-th neuron (*v=1* to N_m) in the (*m+1*)-th layer (*m=1* to *M-1*) can be estimated by

$$X_j^{(m+1,v)}=X_{i+1}^{(m+1,v)}-\frac{\{\sum_{u=1}^{Nm}W_{uv}^{(m)}(X_{i+1}^{(m,u)}-X_j^{(m,u)})\}(X_{i+1}^{(m+1,v)}-X_i^{(m+1,v)})}{\sum_{u=1}^{Nm}W_{uv}^{(m)}(X_{i+1}^{(m,u)}-X_i^{(m,u)})} \tag{15}$$

Using the operation above, the sigmoid function is partially linearized, as shown in Fig.5. If a function must be learned, the PLNN will learn the points indicated by the ● symbols shown in Fig.5. When new data (s_1', s_2') are input into the converged PNN, the values depicted by the ■ symbols corresponding to the data (s_1', s_2') will quickly be identified as P_e. Thus, the PLNN can be used to deal with ambiguous diagnosis problems.

As shown in Fig.5, the new data (s_1', s_2') input into the converged PLNN, and which are not learnt by the

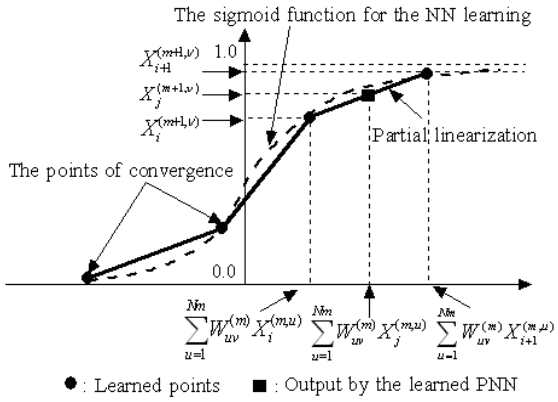

Fig. 4 The partial linearization of the sigmoid function

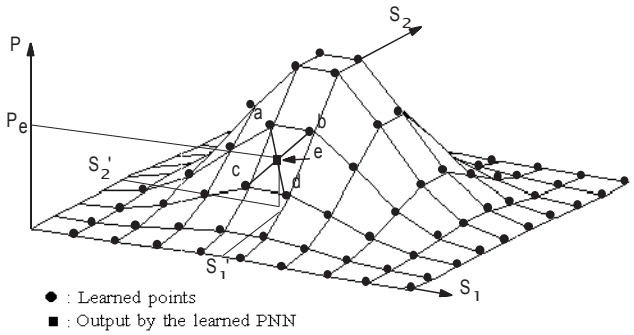

Fig. 5 Interpolation by the PLNN

PLNN for recognizing, must satisfy the following condition.

$$s_{1(\min)} < s_1' < s_{1(\max)} \quad and \quad s_{2(\min)} < s_2' < s_{2(\max)} \tag{16}$$

Here, $s_{1(\min)}$ and $s_{2(\min)}$ are the minimum values, respectively, of s_1 and s_2, which have been learned by the PLNN. Therefore, in this work, the values (P_i^* and P_j^*) of symptom parameters input to the PLNN for fault diagnosis must satisfy the following condition.

$$P_{i(\min)} < P_i^* < P_{i(\max)} \text{ and } P_{j(\min)} < P_j^* < P_{j(\max)} \tag{17}$$

5.2 Diagnosis and Verification by PLNN

Fig.6 shows the PLNN constructed based on an algorithm of sequential diagnosis proposed in this paper, which consists of the first layer, the hidden layer and the last layer. The RRSPs selected by PCA are inputted

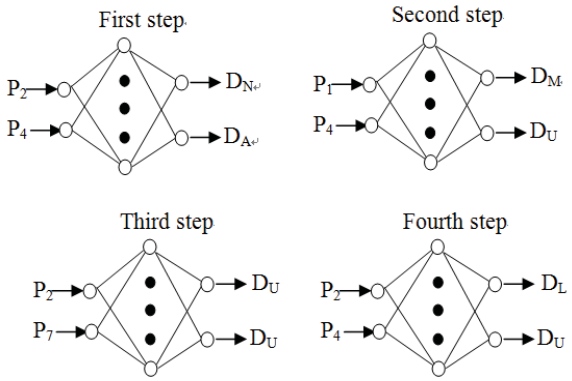

Fig. 6 PLNN for the condition diagnosis

into the neurons in the first layer. The number of neurons in hidden layer is eighty. The outputs in the last layer are D_N, D_A, D_M, D_{UN}, D_L, D_{UA}, which mean the possibility grades of normal (N), abnormal (A), misalignment (M), unbalance (UN), looseness (L) and unknown abnormal state (UA) respectively.

The diagnostic knowledge for the neural network is acquired by the probability theory using the probability distributions of the symptom parameters. An example for obtaining the possibility grade D_N used to judge normal state is shown as follows. p_{iN} is the symptom parameters of normal state (N), its mean value and standard deviation are $\overline{p_{iN}}$ and S_{iN}, the maximum value and the minimum value of p_{iN} are $p_{iN\max}$ and $p_{iN\min}$ respectively. D_{iN} is the possibility grades of normal state. The training data for distinguishing normal state from another state is calculated as follows.

$$\begin{cases} p_{iN} < p_{iN(\min)} \rightarrow D_{iN} = 0.0 \\ p_{iN(\min)} < p_{iN} \le \overline{p_{iN}} - 2S_{iN} \rightarrow D_{iN} = 0.0 \sim 1.0 \\ \overline{p_{iN}} - 2S_{iN} < p_{iN} < \overline{p_{iN}} + 2S_{iN} \rightarrow D_{iN} = 1.0 \\ \overline{p_{iN}} + 2S_{iN} < p_{iN} < p_{iN(\max)} \rightarrow D_{iN} = 0.0 \sim 1.0 \\ p_{iN} > p_{iN(\max)} \rightarrow D_{iN} = 0.0 \end{cases} \tag{18}$$

According to the method for obtaining the training data above, the diagnostic knowledge for the neural network is obtained. Figures7-10 show the acquired training data for distinguishing normal (N), misalignment

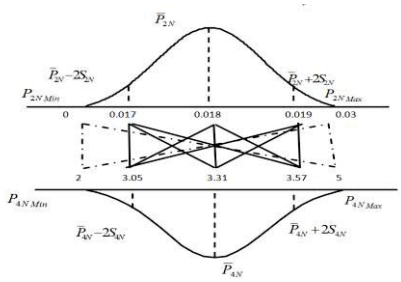

P_2	P_4	N	A
0	2	0	1
0.017	3.05	1	0
0.018	3.31	1	0
0.019	3.57	1	0
0.03	5	0	1
. . .	. . .	. .	. .

Fig. 7 Training data for distinguishing normal state from abnormal states

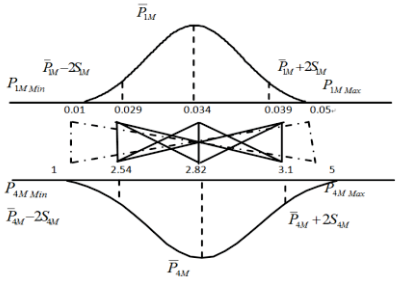

P_1	P_4	M	UA
0.01	1	0	1
0.029	2.54	1	0
0.034	2.82	1	0
0.039	3.1	1	0
0.05	5	0	1
. . .	. . .	. .	. .

Fig. 8 Training data for distinguishing misalignment state from other faults

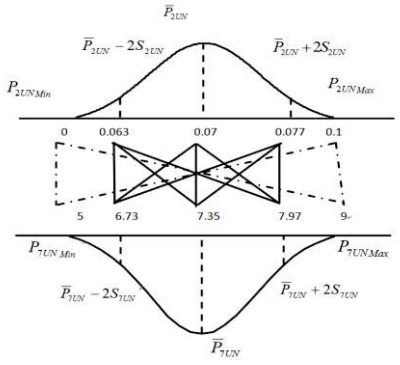

P_2	P_7	UN	UA
0	5	0	1
0.063	6.73	1	0
0.070	7.35	1	0
0.077	7.97	1	0
0.1	9	0	1
. . .	. . .	. .	. .

Fig. 9 Training data for distinguishing the unbalance state from other faults

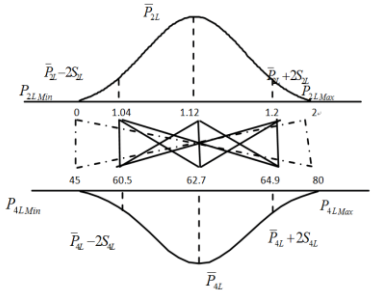

P_2	P_4	L	UA
0	45	0	1
1.04	60.5	1	0
1.12	62.7	1	0
1.20	64.9	1	0
2	80	0	1
. . .	. . .	. .	. .

Fig. 10 Training data for distinguishing looseness state from other faults

(M), unbalance (UN) and looseness (L) states, respectively.

In order to verify the diagnostic capability of the PLNN, we used the test data measured in each state, which had not been learned by the PLNN. When inputting the test data into the learnt PLNNs, they can correctly and quickly diagnose those faults with the possibility grades of the corresponding states. Tables 2-5 show the diagnosis results of each diagnosis step.

Table2 The diagnosis results of normal state and abnormal state

P_2	P_4	N	A	Judge
0.018201	3.367096	0.925368	0.078050	N
0.017363	3.205173	0.910945	0.085984	N
0.062202	2.738114	0.024547	0.987776	A
0.0529439	2.795228	0.099765	0.916373	A
. . . .	. . . .	. . . .	. . . .	. . . .

Table3 The diagnosis results of misalignment state and another state

P_1	P_4	M	UA	Judge
0.034579	2.68127	0.842265	0.198921	M
0.031258	2.79294	0.815564	0.196249	M
0.27014	61.73368	0.218752	0.824733	UA
0.31322	62.03948	0.213242	0.831093	UA
. . . .	. . . .	. . . .	. . . .	. . . .

Table4 The diagnosis results of unbalance state and another state

P_2	P_7	UN	UA	Judge
0.069081	7.35337	0.801245	0.198702	UN
0.073523	7.20199	0.757909	0.241996	UN
0.004438	3.341986	0.149298	0.839746	UA
0.004769	4.207943	0.160381	0.854491	UA
. . . .	. . . .	. . . .	. . . .	. . . .

Table5 The diagnosis results of looseness state and another state

P_2	P_4	L	UA	Judge
1.133676	62.97866	0.801245	0.198702	L
1.112879	63.00435	0.757909	0.241996	L
0.05621	4.017395	0.149298	0.839746	UA
0.05587	4.447923	0.160381	0.854491	UA
. . . .	. . . .	. . . .	. . . .	. . . .

6. Conclusions

Condition diagnosis of rotating machinery depends largely on the feature analysis of vibration signals measured for the condition diagnosis because the signals carry dynamic information about the machine state. However, feature extraction for fault diagnosis is difficult because the signal contains strong noise. Noise stronger than the actual failure signal may lead to misrecognition of useful information for the condition diagnosis, and there are many ambiguous relationships between the symptom parameters and the failure types. In order to effectively diagnose fault and automatically identify the condition of a rotating machine, an intelligent diagnosis method was proposed on the basis of the fuzzy neural network called Partially-Linearized Neural Network (PLNN) and relative ratio symptom parameters (RRSPs) in frequency domain. The main conclusions are summarized as follows:

(1) The nine symptom parameters called "relative ratio symptom parameters" in the low-frequency domain were defined for reflecting the features of vibration signals measured in each state.
(2) A sequential diagnosis technique was proposed through which the fuzzy neural network realized by the partially-linearized neural network (PLNN) could sequentially distinguish fault types.
(3) Sensitive evaluation method for selecting good symptom parameters using principal component analysis (PCA) was also proposed for detecting and distinguishing faults in rotating machinery.
(4) The method proposed in this paper had been successfully applied to fault diagnosis of a rotating shaft and the faults such as misalignment state (M), unbalance state (UN) and looseness state (L) were sequentially and automatically diagnosed on the basis of the possibilities of the RRSPs.

References

[1] P. Chen, T. Toyota and Z. J. He. Automated Function Generation of Symptom Parameters and Application to Fault Diagnosis of Machinery in Variable Operation-conditions, *IEEE Transactions on System, Man, and Cybernetics (Part A)*, Vol. 31, No. 6, pp. 775-781, 2001.

[2] K. Li and P. Chen. Intelligent Method for Diagnosing Structural Faults of Rotating Machinery Using Ant Colony Optimization, *Sensors*, No.11, pp. 4009-4029, 2011.

[3] H. C. Pusey. Machinery Condition Monitoring, *Journal of Sound and Vibration*, Vol. 34, No. 5, pp. 6-7, 2000.

[4] H. Matuyama. Diagnosis Algorithm, *Journal of JSPEl*, Vol. 75, No. 3, pp. 35-37, 1991.

[5] L. Jing, Q. Liangsheng. Feature Extraction Based on Morlet Wavelet and Its Application for Mechanical Fault Diagnosis, *Journal of Sound and Vibration*, Vol. 234, No. 1, pp. 135-148, 2000.

[6] Christopher M. Bishop. *Neural networks for pattern recognition*, Oxford University Press, NY, 1995.

[7] Jolliffe, I. T. *Principal Component Analysis*, Springer, NY, 2002.

[8] M. C. Johannesmeyer, A. Singhal and D. E. Seborg. Pattern Matching in Historical Data, *American Control Conference*. Vol. 5, pp. 3696-3701, June 4-6, 2003, Santa Barbara, CA, USA.

[9] M. Kano, S. Tanaka, S. Hasebe, I. Hashimoto and H. Ohno. Monitoring Independent Components for Fault Detection, *AIChE Journal*, Vol. 49, No. 4, pp. 969-976, 2003.

[10] N. Lu, F. Wang and F. Gao. Combination Method of Principal Component and Wavelet Analysis for Multivariate Process Monitoring and Fault Diagnosis, *Industrial & engineering chemistry research,* Vol. 42, No. 18, pp. 4198-4207, 2003.

[11] B. Samanta and K. R. Al-Balushi. Artificial Neural Network Based Fault Diagnostics of Rolling Element Bearings Using Time-Domain Features, *Mechanical Systems and Signal Processing*, Vol. 17, No. 2, pp. 317-328, 2003.

[12] I. E. Alguindigue, A. Loskiewicz-Buczak and R. E. Uhrig. Monitoring and Diagnosis of Rolling Element Bearings Using Artificial Neural Networks, *IEEE Transactions on Industrial Electronics*, Vol. 40, pp. 209-216, 1993.

[13] R. Q. Li, J. Chen and X. Wu. Fault Diagnosis of Rotating Machinery Using Knowledge-Based Fuzzy Neural Network, *Applied Mathematics and Mechanics,* Vol. 27, No. 1, pp. 99-108, 2006.

[14] K. Li, H. Q. Wang and P. Chen. Intelligent Diagnosis Method Based on Feature Spectra and Fuzzy Neural Network for Distinguishing Structural Faults of Rotating Machinery, *Information*, Vol. 13, No. 3(A), pp. 681-689, 2010.

International Journal of Comprehensive Engineering
Part A, 2(1), 11-19, 2013
Doi: 10.14270/IJCE2013.2.1.a11
Regular paper

ISSN 2186-2680
e-ISSN 2186-2656
www.iace-journal.org

The Application of Dual Tree Complex Wavelet Transform in Mechanical Multi-component Signal Decomposition and Feature Extraction

Binqiang Chen [1], Zhousuo Zhang [1,#], Jie Zhang [1], Chuang Sun [1] and Zhengjia He [2]

[1] School of Mechanical Engineering, Xi'an Jiaotong University,
Xi'an Jiaotong University, Xi'an 710049, PR China
[2] School of Mechanical Engineering, State Key Laboratory for Manufacturing and Systems Engineering,
Xi'an Jiaotong University, Xi'an 710049, PR China

[#] Corresponding author: zzs@mail.xjtu.edu.cn; Tel.: +86-29-82663689; Fax: +86-29-82663689

Abstract: Wavelet transform is a popular tool for mechanical signal processing, while it suffers a few intrinsic defects which cannot be avoided within the scope of Mallat's critically sampled filter bank. Redundancy is beneficial for enhancing the performance of wavelet transform as it allow higher design freedom for wavelet basis construction and improving the filter bank structure. Dual tree complex wavelet transform (DTCWT) is an discrete dyadic wavelet transform with a redundancy factor of 2. The wavelet basis of DTCWT basis is a hybrid one that organically integrates two related dyadic wavelet basis. DTCWT's hybrid basis' two wavelet functions form an pair of Hilbert transform pair, which equips the DTCWT with appealing properties of nearly analytic, nearly shift invariant and reduced spectral aliasing. These advantages of DTCWT are suitable for multi-component signal decomposition in mechanical vibration measurement. In this paper, a feature extraction technique based on DTCWT is proposed for rotating machinery's vibration signal analysis. Numerical simulation and vibration signals from an experimental rotor setup are used to validate the effectiveness of proposed technique. It is shown that DTCWT show robust performance in analyzing multi-component signals, even in low SNR environments.

Keywords: Hybrid Wavelet Tight Frame, Dual Tree Complex Wavelet Transform, Shift Invariant, Multi-component Signal.

Received: May 10,2012 / Accepted: Nov. 6,2012 / Published: Apr. 8,2013

1. Introduction

The manufacturing industry is experiencing rapid development. The averaged speed of rotating machinery is growing annually [1]. In order to make effective monitoring of the operating condition during rotating machinery's service life, testaments of processing variables such as force, acoustic emission, vibration, current, image and etc [2]. Among these available alternatives, vibration measurement is popular by rotating machinery's condition monitoring [3]. For large and complex electromechanical systems, early and incipient fault features are weak in energy and is harassed by other irrelevant vibration contents. In order to extract the critical fault features, a vast variety of signal processing tools are employed. In the past two decades, wavelet analysis distinguishes itself from other techniques due to its time-frequency analyzing ability and explicit physical meaning. Wavelet analysis has been widely applied in massive industrial fields [4,5].

Among the alternatives of wavelet bases, Daubechies' orthonormal bases are very popular [6]. In addition, Swelden's lifting scheme is also an efficient strategy to construct biorthogonal wavelet bases [7]. In spite of their substantial differences in numerical implementation, both DB orthonormal wavelet transform and lifting wavelet bases are within the scope of critically sampled dyadic wavelet transform (CSDWT). CSDWT are sensitive to shift of signals [8] and suffers energy leakage problem [9]. These two problems are intrinsic properties of CSDWT that cannot be avoided by proper selection of wavelet bases. However, researchers have

turned to the construction of wavelet frames, which are indeed redundant wavelet bases for signal representation [10].

By introducing proper redundancy, the wavelet basis can be converted into wavelet tight frame. A wavelet tight frame possesses higher freedom in basis construction. DTCWT is a typical example of wavelet tight frame whose basis is a hybrid integration of two correlated dyadic wavelet basis. Moreover, it utilizes different filters in different decomposition levels. The two wavelet functions of DTCWT form an approximate Hilbert transform pair, which equips the DTCWT with appealing properties of nearly analytic, nearly shift invariant and reduced aliasing. These advantages make DTCWT an enhanced tool for multi-component signal analysis and transient feature extraction. In this paper, numerical simulation signal composing of common fault features in rotating machinery is used to test the performance of DTCWT, classical orthonormal basis and EMD. On the other hand, a rotor kit setup is used to simulate a rub-impact system for the purpose of testing the incipient feature extraction ability of the above methods. The processing results show that DTCWT is much robuster in dealing with multi-component signal, even in very low SNR environments.

2. Theoretical Background

2.1 Brief review of redundant wavelet frame

Discrete wavelet transform is a signal expansion method with respect to a specific wavelet basis. The wavelet basis $\Phi = \{\varphi_i\}_{i\in I}$, where I={1,2,...,M}, is formed by scaling and translations of a scaling function and a wavelet function. Let $x = \{x_i\}_{i=1,2,\cdots,N}$ be a signal in square summable function space $\ell^2(\square)$. In CSDWT, N=M. In the case of N<M, the family of $\Phi = \{\varphi_i\}_{i\in I}$ in a Hilbert space H becomes a redundant wavelet frame if it satisfies the following inequality

$$A\|x\|^2 \leqslant \sum_{i=1}^{M} \left|\langle x, \varphi_i \rangle\right|^2 \leqslant B\|x\|^2$$

Where $0<A\leqslant B<\infty$ are frame bounds. If $A = B = 1$, the basis Φ become a Parseval tight frame, which is noted for its energy preservation property during transform.

Within frame theory, CSDWT is reduced to a special case of wavelet tight frame in with M=N and A=B=1. Thus we can infer that the time-frequency properties of a wavelet basis could be improved by introducing proper redundancy.

2.2 Review of dual tree complex wavelet transform

DTCWT is a type of wavelet tight frame that possesses a redundancy factor of 2. DTCWT basis is a hybrid one composing of two parallel CSDWT bases. In DTCWT's implementation of decomposition and reconstruction process, as shown in Fig. 1, there is no data flow in between the two individual branches. The coefficients are calculated through inner product operation. Taking real branch for example, coefficients are computed via Eq. (1) and (2).

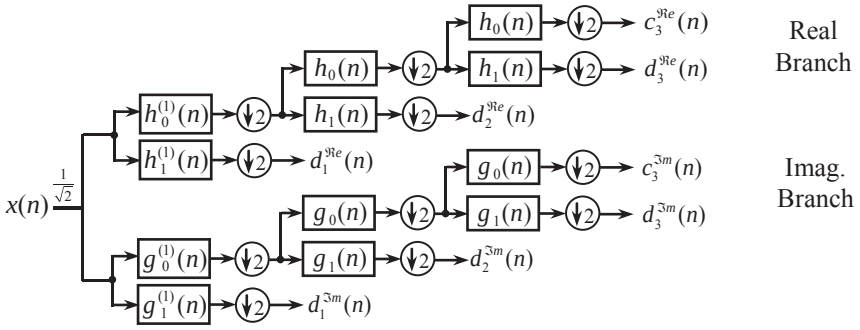

Fig. 1 Implementation of forward DTCWT

$$d_j^{\Re e}(n) = 2^{(j-1)/2} \int_{-\infty}^{+\infty} x(t)\psi^{\Re e}\left(2^j t - n\right)dt \tag{1}$$

$$c_j^{\Re e}(n) = 2^{(j-1)/2} \int_{-\infty}^{+\infty} x(t)\phi^{\Re e}\left(2^j t - n\right)dt \tag{2}$$

As a whole, the energy of the input signal is equal to the energy of wavelet domain, as shown in Eq. 3.

$$\sum_{j\in\mathbb{Z}}\sum_{n\in\mathbb{Z}}\left(\left|d_j^{\Re e}(n)\right|^2+\left|d_j^{\Im m}(n)\right|^2\right)=\sum_{n\in\mathbb{Z}}x^2(n) \tag{3}$$

The wavelet function in DTCWT basis is a complex-valued function $\psi^C(t)=\psi^{\Re e}(t)+\mathrm{j}\cdot\psi^{\Im m}(t)$, in which $\psi^{\Re e}(t)$ and $\psi^{\Im m}(t)$ are wavelet function for real branch and imaginary branch respectively. The principle constraint in constructing DTCWT basis is the self-Hilbertian condition which require the two wavelet function to form an approximate Hilbert transform pairs, as shown in Eq.(4)

$$\psi^{\Im m}(t)=H[\psi^{\Re e}(t)] \tag{4}$$

Where $H[\cdot]$ denotes Hilbert transform operator. An equivalent mathematical expression of Eq.(4) is the celebrated half sample delay condition [11], as shown in Eq.(5).

$$g_0(n)=h_0(n-0.5) \tag{5}$$

In frequency domain, the half sample delay condition is described as magnitude condition and phase condition.

$$\left|G_0(\mathrm{e}^{\mathrm{j}\omega})\right|=\left|H_0(\mathrm{e}^{\mathrm{j}\omega})\right| \tag{6}$$

$$\angle G_0(\mathrm{e}^{\mathrm{j}\omega})=\angle H_0(\mathrm{e}^{\mathrm{j}\omega})-0.5\omega \tag{7}$$

Among the various methods to construct DTCWT bases, Kingsbury's Q-shift solution is widely acknowledged as the constructed bases possess better orthogonality and symmetry properties [8,12]. However it should be noted that the analysis filters $\left\{h_0^{(1)}(n),h_1^{(1)}(n),g_0^{(1)}(n),g_1^{(1)}(n)\right\}$ in the first decomposition level is different from the rest levels as the input signal is not downsampled before the first decomposition level. Theatrically speaking, dyadic wavelet basis satisfying perfect reconstruction condition is applicable in DTCWT's first decomposition level. Kingsbury also designed wavelet filters for the first decomposition level, which has feasible approximation of constraints in Eq. (3) and Eq. (4). The filters of $h_0^{(1)}(n)$ and $h_1^{(1)}(n)$, as well as their synthesis filters for real branch, are displayed in Fig. 2. The filters in imaginary branch are obtained by offsetting real branch filters by one sample.

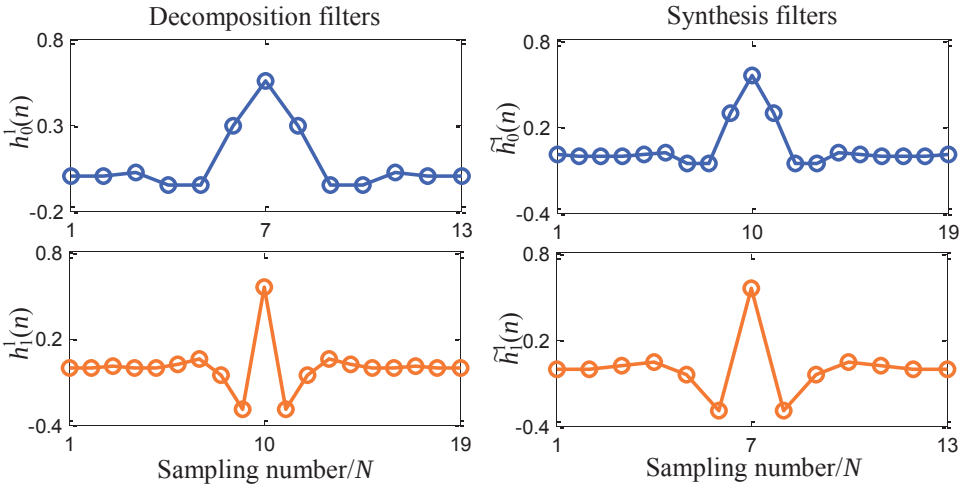

Fig. 2 Implementation of forward DTCWT

3. Time-frequency properties of DTCWT bases

An advantages of DTCWT actually comes form its wavelets approximating Hilbert transform pair. However, it is aware that the magnitude condition in Eq.(6) and the phase condition in Eq.(7) cannot be both exactly satisfied for discrete DTCWT. Q-shift solution can meet magnitude condition while approximate the phase condition with good accuracy. Unlike DB orthonormal basis whose time domain localizability degrades with the incensement of its supports. The family of Q-shift DTCWT bases are self similar, that is to say, the main lobe of a Q-shift DTCWT basis of short length are similar to that of Q-shift DTCWT basis of extremely long support. This property guarantees the performance of short DTCWT basis in engineering applications. Fig. 3 shows the complex scaling function and complex wavelet function of Q-shift DTCWT basis with length of 18 and one vanishing moment. It can be seen in Fig. 3(a) and Fig. 3(b) that the complex scaling function and complex wavelet function is low in oscillation, hence proper for matching localized singularities.

The DB orthonormal basis tries to enhance its basis function's smoothness by increasing its vanishing moment. Fig. 4 shows the time envelop of the complex scaling function and complex wavelet function of DTCWT basis in Fig.3. It can be seen that although the functions are low in vanishing moment number and high in smoothness, which is big difference from DB orthonormal basis.

Fig. 4 shows the frequency response of four level DTCWT decomposition. It can be inferred that the complex wavelet filters are nearly analytic as the energy of its magnitude spectrum are low in negative frequency axis. The analyticity of first level complex wavelet function is relatively as it is derived from sample offset of the wavelet basis in real branch. The near analytic property of DTCWT's frequency response in connected to its better shift invariance and reduced spectral aliasing.

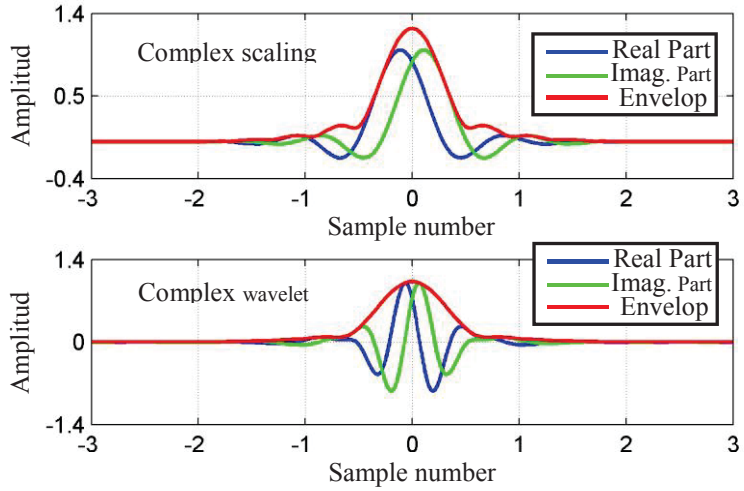

Fig. 3 Complex scaling function and complex wavelet function of DTCWT

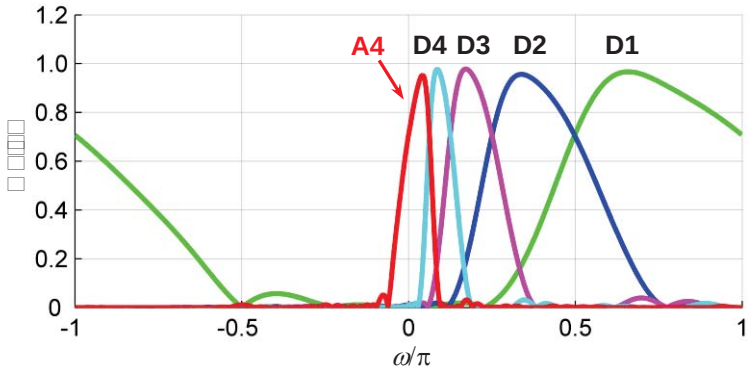

Fig. 4 Frequency response of DTCWT basis

4. Numerical Simulation

DTCWT is a good alternative to classical CSDWT in mechanical fault feature extraction. In this section, DTCWT is compared with classical wavelet transform (DB basis) and empirical mode decomposition (EMD) [13] in multi-component signal decomposition. EMD is also a popular adaptive signal analysis tool. It is reported that EMD shows similar octave band decomposition manner which is similar to wavelet transform.

The simulated signal x is composed of three single side damping and oscillatory components.

$$x(t) = 0.4x_1(t) + 1.5x_2(t) + x_3(t) + 0.2x_4(t)$$

Where

$$x_1(t) = 0.3\cos(2\pi \cdot 700 \cdot t)$$

$$x_2(t) = \cos\left(2\pi \cdot 340 \cdot t + \cos(2\pi \cdot 25 \cdot t)\right)$$

$$x_3(t) = \cos(2\pi \cdot 200 \cdot t) \cdot \left[1 + 0.4\cos(2\pi \cdot 15 \cdot t)\right]$$

$$x_4(t) = \cos(2\pi \cdot 120 \cdot t)$$

The time domain wave and spectrum of the simulation signal $x(t)$ are given in Fig. 5. The colored areas in Fig. 5(b) show the pass band of each wavelet subband, the four components in the simulation signal are

supposed to be separated into four distinct subbands. $x_1(t)$ and $x_4(t)$ are harmonic contents which are different in frequency, while $x_2(t)$ is an amplitude modulation content and $x_3(t)$ is a frequency modulation content. The time domain wave of the each component is shown in Fig. 6.

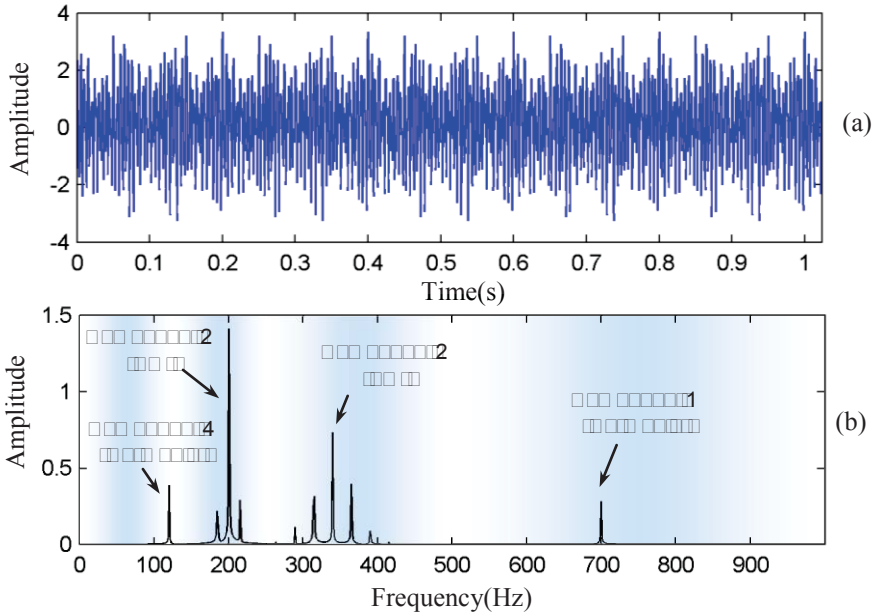

Fig. 5 Time domain wave of spectrum of simulation signal (a) Time domain wave (b) Its Fourier spectrum

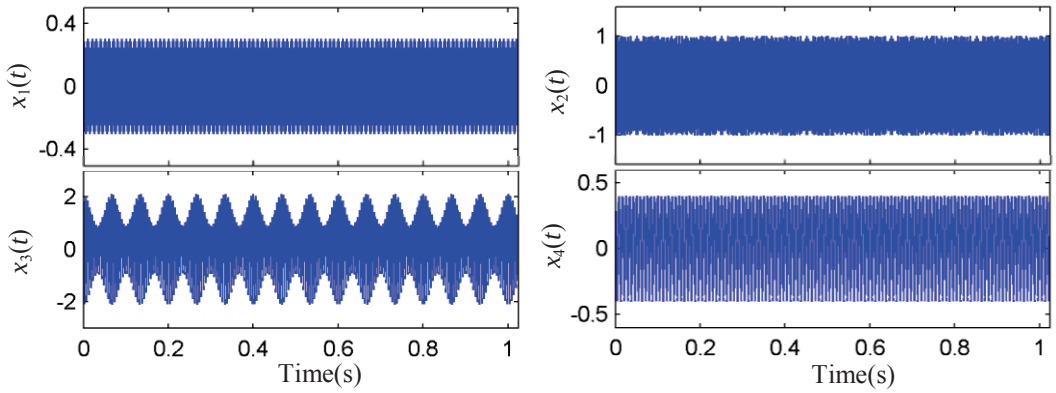

Fig. 6 Time domain wave of four simulation componets

By performing four level DTCWT on the simulation signal, we obtain the wavelet subbands are shown in Fig. 7. It can be observed that the signal in each subband is very similar to their original signal. Only the low oscillatory harmonic component shows attenuation in amplitude. This phenomenon actually comes from the fact that the frequency of low oscillatory harmonic is located in transition band of two adjacent wavelet subbands.

As comparison, the simulation signal is processed by DB9 orthonormal basis and EMD. The decomposition results of DB9 basis is shown in Fig. 8. It can be seen that signal in each wavelet subband show evident distortion with different severity, especially the low extracted low oscillatory harmonic display false modulation effect.

In order to make a quantitative analysis of results in Fig. 7 and Fig. 8, the index of correlation coefficient (CC), which can make precise assessment of the similarity between two series, is employed here. Fig. 9 show the correlation coefficients of wavelet subbands by the above two basis to the orginal signal $\{x_i(t)\}_{i=1,2,3,4}$. It can be inferred form Fig.9 that the CC derived from DTCWT are greater to that of DB basis, indicating that the decompostion results by DTCWT is superior.

The four intrinsic mode functions (IMF) by EMD are plotted in Fig. 10. The decompostion results by EMD show severe mode cracking. None of the IMFs recover the feature of the four signal contents. The spectrum of the four IMFs are also given in Fig. 11, it can be seen that features of $\{x_i(t)\}_{i=1,2,3}$ mix in IMF1, while in other IMFs, the features are severly distorted. In the analysis of the simulation signal, EMD show poor performance in separating four distinct signal contents.

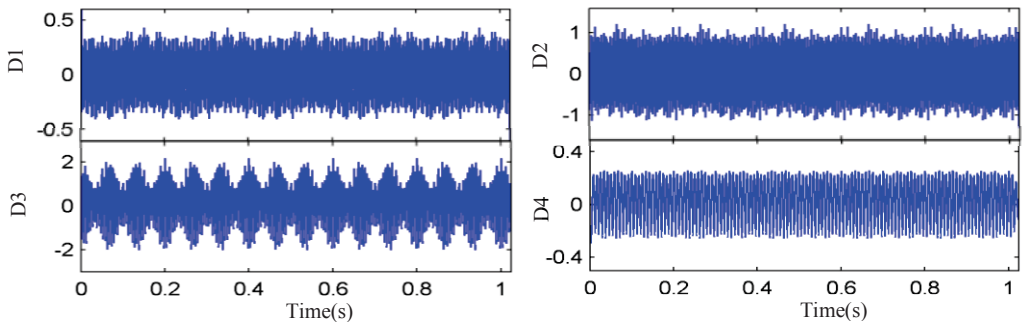

Fig. 7 Decomposition results by DTCWT basis

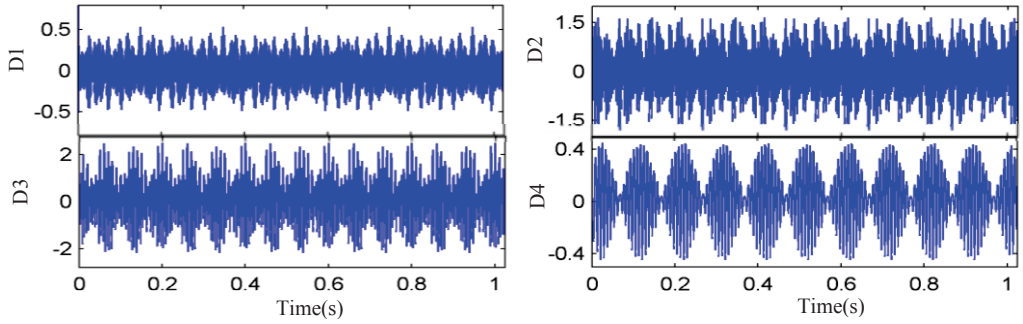

Fig. 8 Decomposition results by DB orthonormal basis

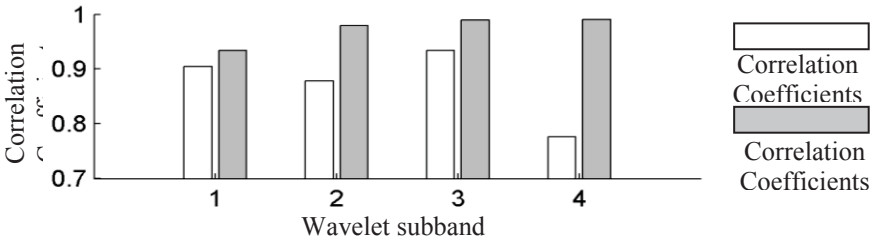

Fig. 9 Correlation coefficients of two wavelet basis to the orignal signal contents

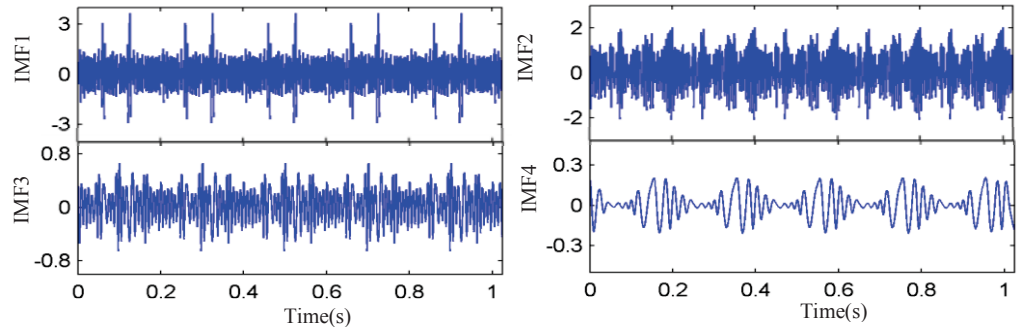

Fig. 10 Four IMFs of the simulation signal by using EMD

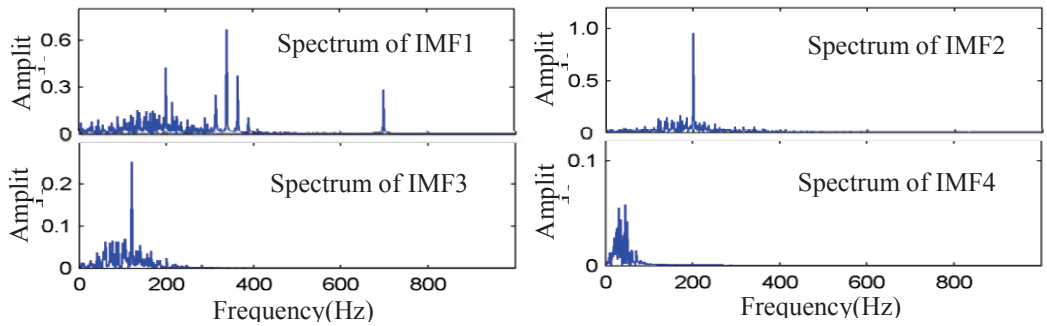

Fig. 11 Fourier spectrum of the four IMFs

5. Experimental Test

The schematic draw of Bently RK4 Rotor kit is given in Fig. 12. The rotor system is formed by one DC motor, two bearing supports and a rotor mass. The signals are collected by two proximity induction sensors. A Rub screw is utilized as the source of periodical rub source. The rotating speed of the DC motor is 2200r/m, and the vibration signals are acquired at the sampling frequency of 2000Hz. Each record of measured signal is of length 1024. The signal collected from sensor 1 is plotted in Fig. 13(a) and its spectrum in Fig. 13(b).

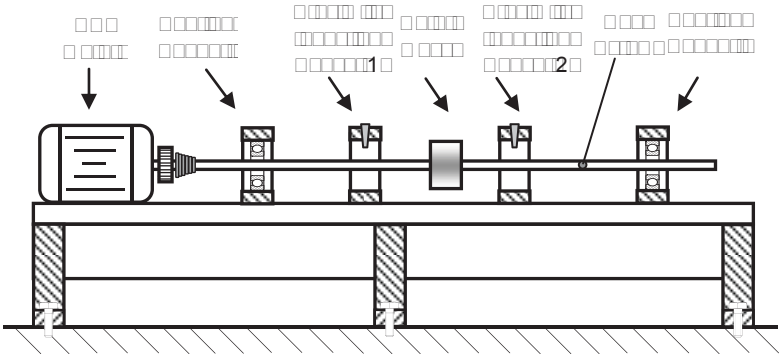

Fig. 12 Schematic draw of Bently RK4 Rotor Kit

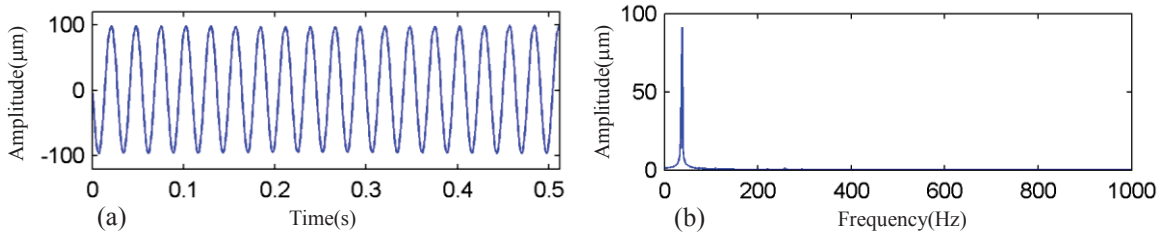

Fig. 13 Vibration signal from sensor 1. (a) Time domain wave. (b) Fourier spectrum.

It can be observed from Fig. 14(a) and Fig. 14(b) that the harmonic content related to the rotating speed of the DC motor is the dominant content in the vibration signal. The vibration content caused by the rub screw is so incipient that it is not detected by conventional FFT method. By performing a 3 level DTCWT decomposition, the four wavelet subbands are shown in Fig. 13. D1 subband is very weak in energy, and its messy waveform reveals that it is mainly irrelevant background noises. D3 subband successfully extracts the periodical impulses caused by rub-impact effect. Comparing D3 subband with D4 subband, we can find that the critical features of rub impact is quite small. The energy ration of D3 and D4 is 1.19%. The analysis results show that DTCWT display robust performance in extracting incipient fault features from low SNR environment. Fig. 15 plots the wavelet subbands derived from DB9 orthonormal basis. Only the D4 subband is comparable to that of DTCWT. The important feature in D3 subband is not so explicit. Fig. 16 shows the zoom-in plot of D3 subbands from DTCWT and DB9 basis. The result of DTCWT is much better, because the periodical single side oscillatory and damping impulses are fairly manifest and its averaged period is 0.0272s (36.745Hz) which is very close to DC motor's rotating frequency (36.667Hz). However, the D3 subband of DB 9 basis only shows a few irregular localized singularities.

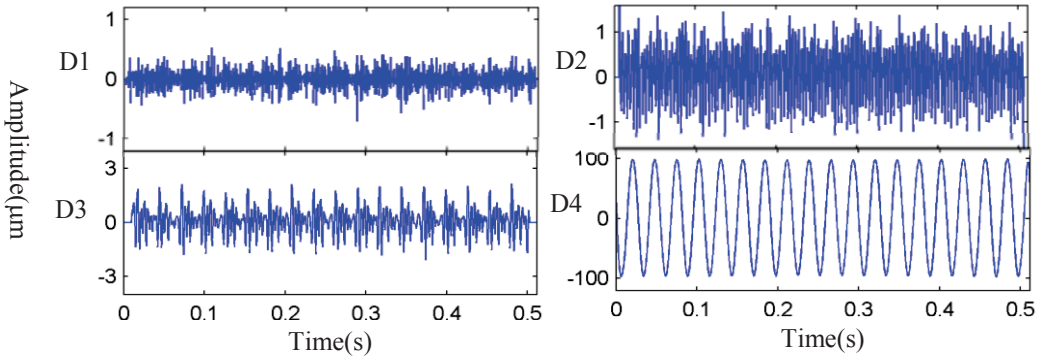

Fig. 14 Decomposition results of DTCWT

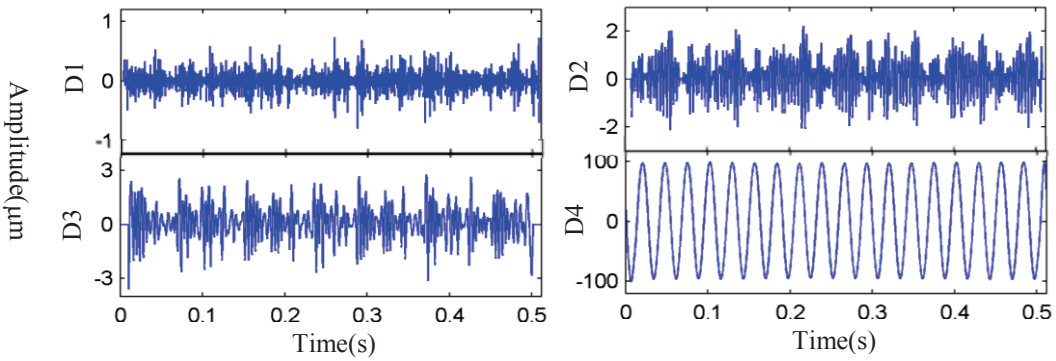

Fig. 15 Decomposition results of DB9 basis

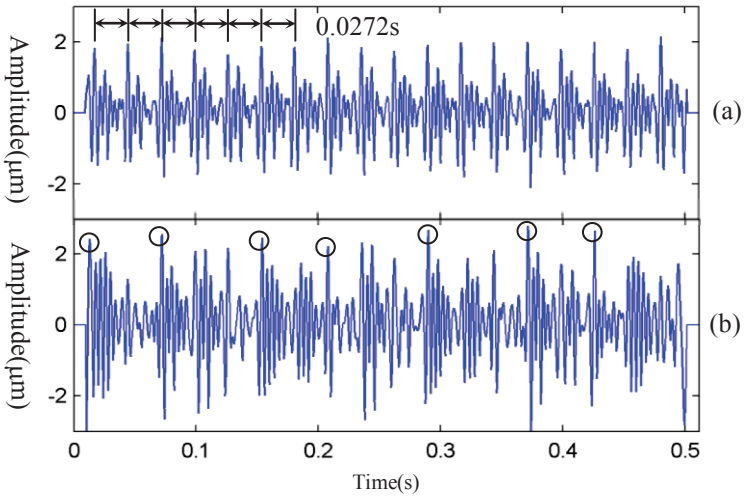

Fig. 16 Zoom-in plots of D3 subband form two wavelet transform

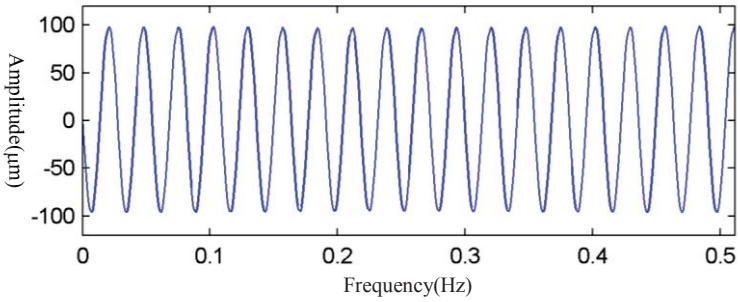

Fig. 17 Decomposition result of EMD

EMD shows very poor performance in revealing the hidden fault features of the rub-impact system. Fig. 17 shows its decomposition result. As mentioned in the analysis of DTCWT's decomposition results, the critical features in the signal is so weak that they do not affect the local monotony of the vibration signal, and the signal exactly satisfy Huang's two necessary condition of IMF, so EMD refuse to make further decomposition to the signal.

6. Conclusion

In this paper, the characteristics of DTCWT's wavelet basis and its time-frequency properties are investigated for explanations of its advantages. The DTCWT's wavelet basis is actually a hybrid one which integrated 2 dyadic wavelet bases. Moreover, it employs special filters in its first level decomposition. The hybrid wavelet basis equips DTCWT with appealing properties of nearly analytic, nearly shifts invariant and reduced spectral aliasing.

A simulation signal containing common mechanical fault feature characteristics, including harmonics and amplitude/frequency modulation contents, is used to test the multi-component signal analysis ability of DTCWT

as well as that of DB wavelet basis and empirical mode decomposition. A quantitative analysis by using correlation coefficient index is made and shows that the performance of DTCWT is superior. On the other hand, an experimental rotor kit system is used to simulate rub-impact system. DTCWT successfully extracts the hidden incipient periodical impulses in very low SNR environments where DB orthonormal basis and EMD do not acquire so satisfying results. DTCWT as well as other hybrid wavelet tight frame will become useful supplement to classical wavelet analysis methods.

Acknowledgment

This research is supported financially by National Natural Science Foundation of China (No. 111760245), the key project of National Natural Science Foundation of China (No. 51035007), National Basic Research Program of China(No. 2010ZX04014-016) and the Specialized Research Fund for the Doctoral Program of Higher Education (no 20110201130001).

References

[1] S. R. Singiresu. *Mechanical Vibrations*, *5th ed*. Prentice-Hall, New Jersey , 2011.

[2] K. P. Zhu, Y. S. Wong and G. S. Hong. Wavelet Analysis of Sensor Signals for Tool Condition Monitoring: a Review and Some New Results, *International Journal of Machine Tools and Manufacture*, Vol. 49, No. 7-8, pp. 537-553, 2009.

[3] J. S. Mitchell. From Vibration Measurements to Condition Based Maintenance - Seventy Years of Continuous Progress, *Sound And Vibration*, Vol. 41, No. 1, pp. 62-78, 2007.

[4] Z. K. Peng and F. L. Chu. Application of the Wavelet Transform in Machine Condition Monitoring and Fault Diagnostics: a Review With Bibliography Review Article, *Mechanical Systems and Signal Processing*, Vol. 18, No. 2, pp. 199-221, 2004

[5] H. Kim and H. Melhem. Damage Detection of Structures by Wavelet Analysis, *Engineering Structures*, Vol. 26, No. 3, pp. 347-362, 2004.

[6] I. Daubechies. *Ten Lectures on Wavelets*, SIMA, Philadelphia, 1992.

[7] W. Sweldens. The Lifting Scheme: a Custom-Design Construction of Biorthogonal Wavelets, *Journal of Applied and Computational Harmonic Analysis*. Vol. 3, No. 2, pp. 189-200, 1996.

[8] N G Kingsbury. Complex Wavelets for Shift Invariant Analysis and Filtering of Signals, *Journal of Applied and Computational Harmonic Analysis*, Vol. 10, No. 3, pp. 234-253, 2001.

[9] Z. K. Peng, M. R. Jackson, J. A. Rongong, F. L. Chu and R. M. Parkin. On the Energy Leakage of Discrete Wavelet Transform, *Mechanical Systems and Signal Processing*, Vol. 23, No. 2, pp. 330-343, 2009.

[10] J. Kovacevic and A. Chebira. Life Beyond Bases: The Advent of Frames (Part I), *IEEE Signal Processing Magazine*, Vol. 24, No. 4, pp. 86 - 104, 2007.

[11] I. W. Selesnick. The Design Of Approximate Hilbert Transform Pairs of Wavelet Bases. *IEEE Transaction on Signal Processing*, Vol. 50 No. 5:1144-1152, 2002.

[12] F. Yeganli. A Design of Q-shift Filter for Dual-Tree Complex Wavelet Transforms, Eastern Mediterranean University, 2010.

[13] N. E. Huang, Shen Z, Long S R, et al. The Empirical Mode Decomposition and the Hilbert Spectrum for Nonlinear And Non-Stationary Time Series Analysis, *Proceedings of the royal society of London series a-mathematical physical and engineering sciences*, Vol. 454, No. 1971, pp. 903-995, 1998.

International Journal of Comprehensive Engineering
Part A, 2(1), 20-27, 2013
Doi: 10.14270/IJCE2013.2.1.a20
Regular paper

ISSN 2186-2680
e-ISSN 2186-2656
www.iace-journal.org

Extract Method of Flue Gas Generator Set State Feature Weak Information Based on Birgé-Massart Threshold

Xiaoli Xu [1, 2 #], Zhanglei Jiang [1], Bin Ren [1] and Tao Chen [2]

[1] School of Mechanical and Vehicle Engineering, Beijing Institute of Technology, Beijing 100081,china
[2] Key Laboratory of Modern Measurement & Control Technology，Ministry of Education, Beijing Information Science and Technology University, Beijing 100192,china

[#] Corresponding author: xuxiaoli@bistu.edu.cn; Tel.: +86-010-82426991-613
author: Jiang_Zhanglei@126.com

Abstract: Flue gas generator set is a kind of large high-speed rotating machinery in petrochemical industry, which function is transfer the energy in catalytic cracking regeneration flue gas into mechanical energy. The operational status monitoring in order to ensure safe and stable operation of the flue gas generator set needs to resolve problem in the extraction of state feature weak information under large amount of background noise. To this end, the research is on noise suppression algorithms on the basis of Birgé-Massart penalty function strategy to obtain signal wavelet transform modulus maximum of threshold. Obtain the threshold through Penalization Strategy Provided by Birgé-Massart; construct different modulus maximum vertex neighborhood on different wavelet transform decomposition scales to influence the search process of modulus maximum point; obtain the appropriate modulus maximum points sequence on various wavelet decomposition scales; highlight state feature information; finally use Mallat staggered projection to reconstruct signals. In order to validate the effectiveness of the algorithm, it was compared with four kinds of threshold noise suppression methods namely Rigrsure, Sqtwolog, Heursure, Minimaxi, and the results show that this algorithm has a better signal to noise ratio and mean-square error. Apply the algorithm to extract state features weak information of vibration signals collected on the Industrial scene, the results show that the signals after processing has good smoothness while retaining the mutation point and can be used for state feature information extraction of exhaust gas generator set.

Key words: Flue Gas Generator Set, Weak Information Extraction, Modulus Maximum, Punishment Strategies.

Received: May 25,2012 / Accepted: Nov. 6,2012 / Published: Apr. 8,2013

1. Introduction

Most failure of large mechanical and electrical equipment is predictable tendency failure, and its failure development is normally characterized by long course. The factors non-equipment fault information such as working condition, load and environment during the long operational course will result in changes in vibration signal energy, which will result in the information on failure development overwhelmed by non-fault information. Aiming at the difficult prediction problems and facing to the long course variable working condition equipment, it is necessary to make study on the new way of failure prediction based on data, and study on the new failure prediction method based on multi-transform domain non-linear fault trend forecasting，that is a new method to extract sensitive feature information in long history state development[1]. In order to effectively extract equipment status feature information, it is necessary to carry out noise suppression processing for the data.

Flue gas generator set is a kind of large high-speed rotating machinery in petrochemical industry, whose vibration signals are featured by low signal to noise ratio, complex diversity in the long history of equipment operation, variable working condition, and non-stationary state background. The collected vibration signal data

of flue gas generator set is mixed with a lot of noise, so it interfered the extraction of state feature information of the flue gas generator set. How to reduce background noise in vibration signal and effectively extract the flue gas generator set feature from data information becomes the key factor affecting the fault diagnosis and fault prediction of flue gas generator set. Measurement and Control Technology Key Laboratory of the Ministry of Education has made a beneficial exploration in this area [2-5]. Since the status signal to noise ratio is low during operation of flue gas generator set, in this paper the theory of state feature weak information extraction is used to carry out vibration signal noise suppression, so as to acquire signals after extraction of state features.

2. The basic theory of extraction methods of state feature weak information

To the singularity of signals means that signal at somewhere is intermittent or n-order derivative is discontinuous. The singular point (i.e., catastrophe point) usually contains an important feature of the signal, which corresponds to the state features of the signal. In mathematics, the singularity of signals can often be measured through Lipschitz exponent index number (or singular exponent). Wavelet transform is characterized by time-frequency localization and is capable to effectively analyze the singularity of the signals and to determine the location of singular points and the size of singularity. S. Maallat associates Lipschitz index with local maximum of coefficient modulus after wavelet transform and decay rate of local maximum after wavelet transform in different scales is used to measure local singularity of signals [6].

If the wavelet $\psi(x)$ is real function and continuously differentiable, with order- n vanishing moments $(n \in Z^+)$, $f(x) \in L^2(R)$, then function $f(x)$ has Lipschitz exponent at α, if and only if constant K exists, $\forall x \in Bx_0$, its wavelet transform meets

$$\left|W_{2^j} f(x)\right| \le K 2^{j\alpha} \tag{1}$$

Suppose that x_0 is the local mutation point of function $f(x)$, then modulus maximum is selected for $f(x)$ wavelet transform at this point. Eq. (1) shows if $\alpha > 0$, along with the decomposition scale increase, Wavelet transform coefficient modulus maxima increases; if $\alpha < 0$, along with the decomposition scale increases, Wavelet transform coefficient modulus maxima reduces [7].

Suppose that $n(x)$ is white noise whose variance is σ^2, then wavelet transform coefficients $Wn(s,x)$ on scale s meets

$$\left|Wn(s,x)\right|^2 = \int_{-\infty}^{+\infty} \int_{-\infty}^{+\infty} n(u)n(r)\psi_s(x-u)\psi_s(x-r)d_u d_r \tag{2}$$

Resulting from $E\left[n(u)n(r)\right] = \sigma^2\delta(u-r)$, in

$$E(\left|Wn(s,x)\right|^2) = \int_{-\infty}^{+\infty} \int_{-\infty}^{+\infty} E\left[n(u)n(r)\right]\psi_s(x-u)\psi_s(x-r)d_u d_r = \frac{\sigma^2 \left\|\psi\right\|_2^2}{s} \tag{3}$$

Eq.(3) shows, $E(\left|Wn(s,x)\right|^2)$ is inversely proportional to scale s, i.e., along with decomposition scale increase, the model at modulus maximum point of wavelet coefficients controlled by noise will be dramatically reduced.

The average density of modulus maximum point of wavelet transform is

$$d_s = \frac{1}{s\pi}\left(\frac{\left\|\psi^{(2)}\right\|_2}{2\left\|\psi^{(1)}\right\|_2} + \frac{\left\|\psi^{(1)}\right\|_2}{\left\|\psi\right\|_2}\right) \tag{4}$$

Of which, $\psi^{(1)}$, $\psi^{(2)}$ are respectively first and second derivatives of the wavelet ψ. Eq.(4) shows the density d_s of the wavelet coefficient modulus maximum is also inversely proportional to scales. Therefore, if

scale $s = 2^j$, $j = 1, 2, 3, \cdots$, along with decomposition scale increases, at least half of the modulus maximum point can't be delivered to a larger scale, these maximum points mainly belong to noise maximum points.

Normal vibration signals of flue gas generator set without noise should be continuous or discontinuous but bounded in a certain neighborhood, so that its Lipschitz exponent α should be greater than or equal to zero, as the wavelet decomposition scale increases, maximum of coefficient modulus after the wavelet transform also increases; and the Lipschitz exponent α of noise is usually less than 0 [8], along with increases of the wavelet decomposition scale, maximum of coefficient modulus after wavelet transform reduces. Use the different propagation characteristics that modulus maximum of signal and noise increases along with increase of decomposition scale increase in multi-scale space to achieve effective noise suppression for noise vibration signals of flue gas generator set, so as to achieve signals after extraction of state features.

3. The threshold determination method through Penalization Strategy Provided by Birge-Massart

Threshold by Birgé-Massart penalty strategy is obtained from penalty standard in minimization Eq. (5) [9]

$$crit(t) = \sum_{k \le t} c^2(k) + 2\sigma^2 t[\alpha + \ln(\frac{n}{t})], \quad t = 1, 2, \cdots n \tag{5}$$

Of which, in Eq.(5) $c(t)$ is the threshold value needed; $c(k)$ is wavelet coefficient which is stored in descending order of absolute value; σ represents the estimated standard deviation of Gaussian white noise which results from obtaining mid-absolute value of high-frequency coefficient, then expanding coefficient appropriately, for example, as:

$$\sigma = median(|W_{h,v,d}|) / 0.6745 \tag{6}$$

Among them, $W_{h,v,d}$ represents the high-frequency coefficients in horizontal, vertical and diagonal directions, $median$ is median filter function; α is tuning parameters (penalty factor), its typical value is 2; n represents the number of coefficients. Obviously Eq.(5) is the function about t, suppose that when $t = t_{\min}$, $crit(t)$ get the minimum value, then threshold T can be expressed as $|c(t_{\min})|$.

Threshold obtained from Birgé-Massart penalty strategy is adaptive to noise level and is capable to change and adjust the parameters to obtain a suitable threshold.

4. State feature Weak Information Extraction Algorithm under Birgé-Massar Strategy

Based on the above analysis, the State feature Weak Information Extraction Algorithm based on Birgé-Massart penalty strategy so as to achieve threshold is proposed. Firstly carry out binary wavelet decomposition for noisy vibration signals to obtain modulus maximum points corresponding to wavelet transform coefficients on each decomposition scale, and then use Birgé-Massart threshold penalty function strategy to obtain threshold, retain only the points whose maximum modulus is greater than threshold on the maximum wavelet transform decomposition scale J, and construct modulus maximum point neighborhood at modulus maximum point on scale J, which is used as starting point to search modulus maximum point falling inside neighborhood on $J-1$ scale, and the remaining modulus maximum points are zero. Repeatedly build up modulus maximum point neighborhood on the $J-1$ scale, and repeatedly search modulus maximum points on the last decomposition scale. Ultimately, appropriate modulus maximum point sequence on various wavelet transform decomposition scales can be acquired, and finally use Mallat alternative projection to reconstruct signals.

4.1 Steps to Carry out Algorithm

Specific steps based on Birgé-Massart Penalty Strategy to extract state feature weak information are as follows:

(1) dyadic wavelet decomposition of noisy vibration signals.

Determination principles of decomposition layer number is, make sure that the dominant number of modulus maximum value points of signals at the maximum decomposition scale has no loss of important singular point of signals [10]. If the number of wavelet decomposition scale is too small, modulus maximum attenuation

corresponding to noise is inadequate and thus it is difficult to distinguish signal and noise; if the number of wavelet decomposition scale is too large, some important local features of signals will be lost. Since the flue gas generator set vibration signal to noise ratio is relatively small, decomposition scale number is determined as 5.

In order to effectively highlight various singularity characteristics of the signal, db3 wavelet basis with good compact support, orthogonality and relatively high vanishing moment is adopted[11].

(2)work out modulus maximum points corresponding to wavelet transform coefficients on each scale $W_{2^j} f(n_i)$, $j = 1, \cdots 5$ and position of modulus maximum point.

(3)Choose the largest-scale of wavelet decomposition J, and regard threshold T as search threshold on this scale, retain points with the modulus maximum greater than T, remove points with the modulus maximum less than T to get new modulus maximum point $W'_{2^j} f(n_i)$, $j = 1, \cdots$ on scale J.

(4)On scale $J-1$, search set of sequences whose modulus maximum points fall within the limit neighborhood on scale J.

It is difficult to search for the modulus maximum points--- if the searching neighborhood is too large, the candidate spread points are too much excessive, and inevitably mixed with the noise modulus maximum points; if the searching neighborhood is too small, signal modulus maximum may be lost [12]. Therefore parameter ε_j is introduced, that is to influence modulus maximum point searching process through construction of different maximum point neighborhood, so as to obtain the appropriate modulus maximum points sequence on various wavelet decomposition scales.

Use position of maximum point i on scale J as the center, construct a neighborhood $o(n_{j,i}, \varepsilon_j)$, where $n_{j,i}$ is No. i maximum point position on scale J, ε_j is the constant only has relation with the scale. On scale $J-1$, only reserve maximum points falling within this neighborhood. In order to overcome the problem that when the scale is relatively large, the candidate spread points mostly result in that operation speed slows down, value of ε_j can be adaptively adjusted. Repeat the above process till $J = 2$.

(5)For the scale $J = 1$, reserve corresponding maximum points which falling within the modulus maximum points neighborhood on the $J = 2$, but set zero for maximum points at the remaining positions.

Through the above steps, maximum point sequence of new various scale wavelet coefficient modulus $W'_{2^j} f(n_i)$, $j = 1, \cdots 5$ is obtained. Use Mallat staggered projection [13] to reconstruct wavelet coefficients through modulus maximum and its location on various scales, then use the resulting wavelet coefficients inverse transform to obtain reconstructing signals.

4.2 Signal weak information extraction experiments verification

In order to verify the validity of state features weak information extraction algorithm, use MATLAB to carry out simulation signal verification.

Choose 1024 point noisy leleccum signal as verification object to carry out the simulation process based on this algorithm (wavelet basis function selects db3, 5-level signal wavelet decomposition, threshold valued is 0.28) and four kinds of threshold noise suppression methods of Rigrsure, Sqtwolog, Heursure and Minimaxi [14] for noisy signal. After noise suppression process, signal to Noise Ratio R_{sn} and mean-square error σ_{mse} are used for quantitative evaluation of noise suppression results. i.e.:

$$R_{sn} = 10 \lg \left\{ \frac{\sum_{n=1}^{N} s^2(n)}{\sum_{n=1}^{N} \left[s(n) - \hat{s}(n) \right]} \right\}, \tag{7}$$

$$\sigma_{mse} = \frac{1}{N} \sqrt{\sum_{n=1}^{N} \left[s(n) - \hat{s}(n) \right]^2} \tag{8}$$

In Eq.（7）and Eq.（8）, $s(n)$ is the original signal, $\hat{s}$ is estimate signal after noise suppression, N is sampling point.

The time-domain waveform after noise suppression processing is shown in Figure 1. Change the number of modulus maximum points on the wavelet transform maximum scale by adjusting threshold T, influence neighborhood $o(n_{j,i},\varepsilon_j)$ structure of modulus maximum points on all wavelet transform scales by adjusting parameter ε_j so as to enhance the ability of retaining signal catastrophe point. Figure 1 shows that compared with four kinds of threshold noise suppression methods, the state feature weak information extraction algorithm based on Birgé-Massart penalty strategy has better retained signal catastrophe point and achieved the purpose to extract state features.

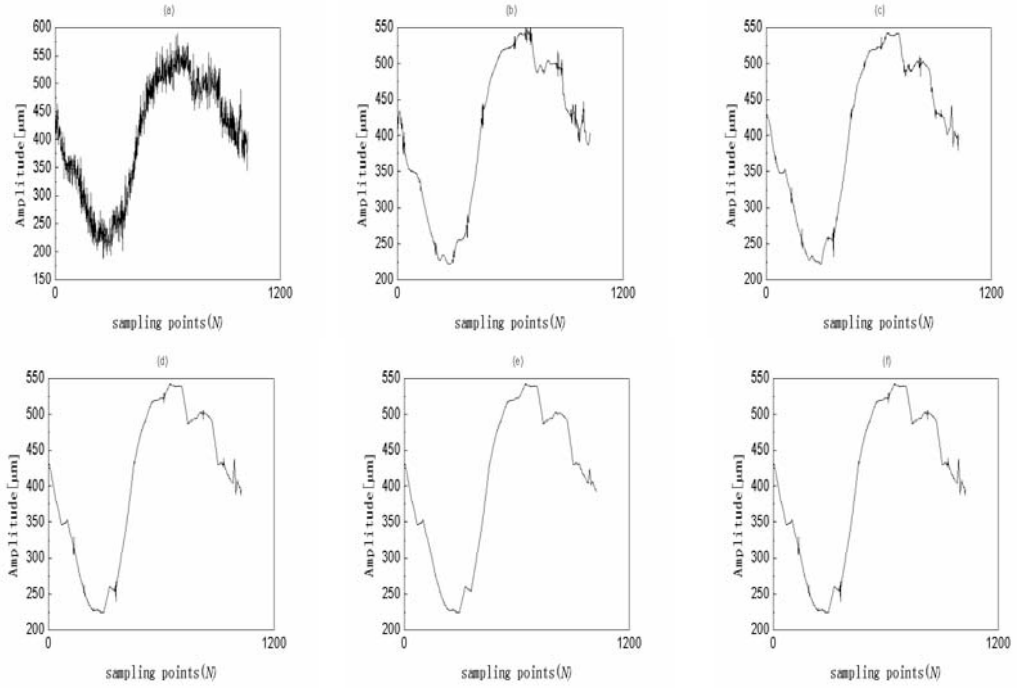

Fig.1 The original signal waveform and signal waveform after noise suppression by different noise suppression methods(a) Original signal time-domain waveform threshold noise suppression(b) Feature information extraction algorithm based on Birgé-Massart penalty strategy (c) Rigrsure threshold noise suppression (d) Heursure threshold noise suppression(e) Sqtwolog threshold noise suppression(f) Minimaxi threshold noise suppression

Table.1 The signal to noise ratio and mean square error after noise suppression by different methods

Noise suppression methods	Signal to noise ratio （R_{sn}）	Mean square error (σ_{mse})
State feature weak information extraction algorithm based on Birgé-Massart penalty strategy	27.354dB	0.55975
Rigrsure threshold noise suppression method	27.324 dB	0.56171
Heursure threshold noise suppression method	26.889 dB	0.59.56
Sqtwolog threshold noise suppression method	26.84 dB	0.59392
Minimaxi threshold noise suppression method	27.053 dB	0.57949

Table 1 shows the noise ratio and mean square error to signal after noise suppression by different noise suppression methods. Table 1 shows that indicators of signal to noise ratio and mean square error by the state feature weak information extraction algorithms are better than those by Rigrsure threshold noise suppression method, Heursure threshold noise suppression method, Sqtwolog threshold noise suppression method, Minimaxi threshold noise suppression method, i.e., after signal noise suppression based on this method can achieve a higher signal to noise ratio under the premise to get a smaller mean square error, and obtain a good noise suppression performance index.

From the view of waveform and signal to noise ratio and mean square error after simulation signal noise suppression, the state feature weak information extraction algorithms not only retain catastrophe point but also has a good performance index.

5. Applications and analysis of state weak feature information extraction algorithm facing to flue gas generator set

Apply the state feature weak information extraction algorithms to flue gas generator set for feature extraction. Flue gas generator set vibration signal data is provided by No. # 1 three catalysis Station of Sinopec, Yanhua Branch, and fault-sensitive YT7701 channel vibration data is selected for analysis. db3 is selected for wavelet basis function for 5 level wavelet decomposition of signals, threshold selection is 0.28. Waveform of reconstructed signal after noise suppression and the original signal are shown in Figure 2,.various scale wavelet transform modulus maximum distribution of original signal of the flue gas generator set is shown in Figure 3. SNR Rsn of flue gas generator set vibration signal after noise suppression is 5.3523dB, mean-square error σ_{mse} is 0.09837. Figure 3 shows the state feature weak information extraction algorithms based on Birgé-Massart penalty strategy to achieve threshold after 5-layer wavelet decomposition has gradually filtered out noise components in the original signals, highlighting state feature information. On $j=5$ scale, signal modulus maximum distribution has been very clear. The searching process of modulus maximum points starting from the 5th layer will more retain the signal singular point, and provide protection for improving accuracy of equipment failure prediction. It can be seen from Figure 3 that the processed signal has a good smoothness.

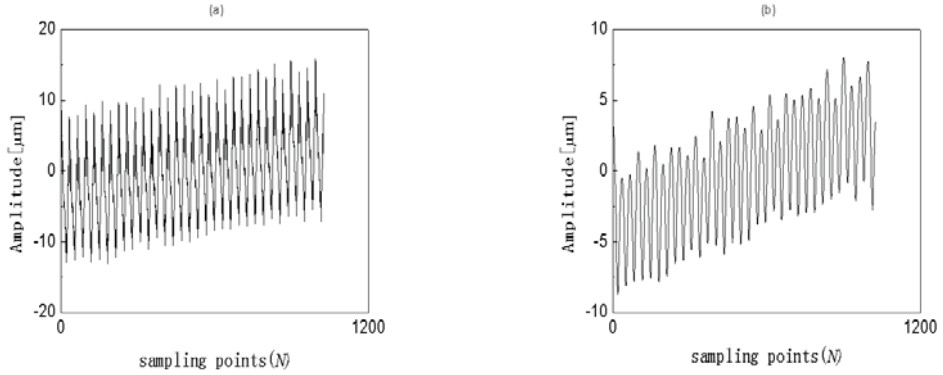

Fig.2 Comparison chart of signal time-domain waveform after processed and original vibration signal time-domain waveform.

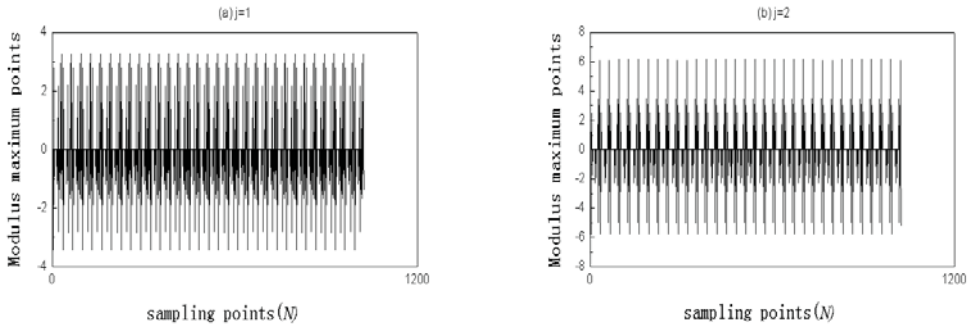

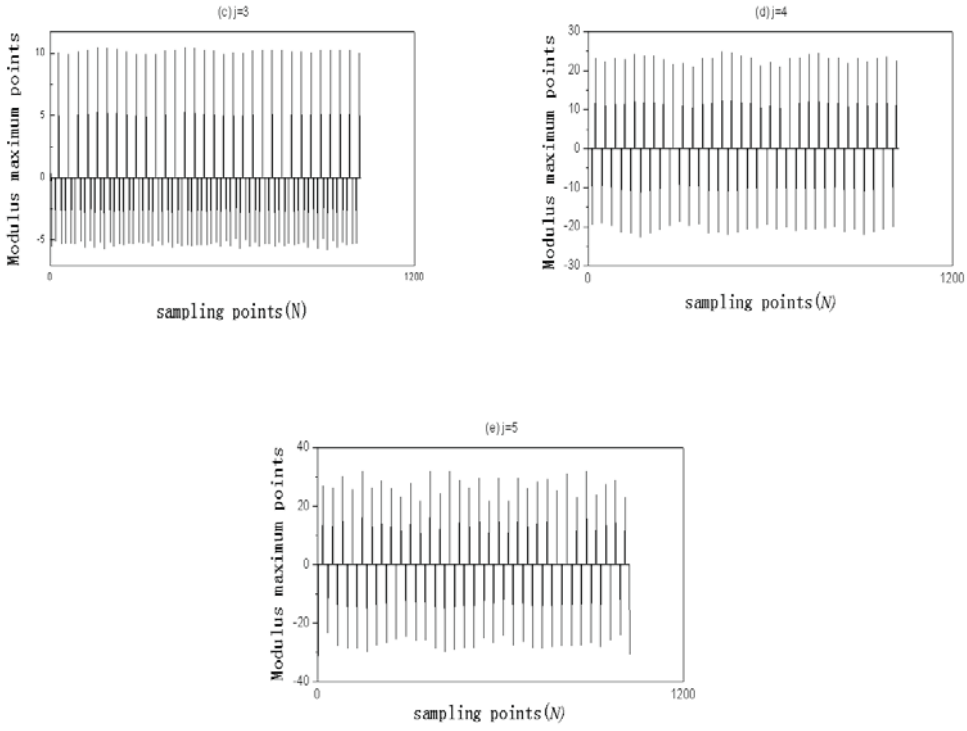

Fig.3 The original signal various scale wavelet transform modulus maximum distribution

6. Conclusion

In this paper, we have researched signal features of flue gas generating set under long course and variable working condition, proposed the state feature weak information extraction algorithm based on Birgé-Massart penalty strategy to achieve threshold, used this method to compare with four kinds of threshold noise suppression methods namely Rigrsure、Sqtwolog、Heursure、Minimaxi, and verified its advantages. The result from applying this algorithm to actual vibration signal feature extraction of flue gas generating set shows that signals after processing by this algorithm not only is retained with the signal singular point but also has a good smoothness, which provides reliable theory reference for flue gas generator fault diagnosis and forecast.

Acknowledgment

This work is partially supported by The National Natural Science Foundation of China（50975020）, and Funding Project for Academic Human Resources Development in Institutions of Higher Learning Under the Jurisdiction of Beijing Municipality（PHR20090518）and Open projects of Key Laboratory of Modern Measurement & Control Technology，Ministry of Education（20111123206、20111123203）.

References

[1] Xiaoli Xu and Tao Chen. ISOMAP Algorithm-based Feature Extraction for Electromechanical Equipment Fault Prediction, *Proceedings of the 2009 2nd International Congress on Image and Signal Processing*, pp. 4622-4625, IEEE Press, Sept., 2009.

[2] Xiaoli Xu and hongjun Wang. *Large Rotating Machinery Running State Trend Forecasting*, Science Press, Beijing, 2011.

[3] Baojie XU, Xiaoli XU and Guoxin WU. Fault diagnosis based on immune algorithm, *Journal of Beijing Information Science and Technology University*, Vol. 24, No. 2, pp. 24-28, 2009.

[4] Tao Chen. Study on Key Technologies of Nonlinear and Nonstationary Fault Prediction for Large Rotating

Machinery, 2010.

[5] X. L Xu, C. M Zhu and J. M Zhang. Tend Prediction Method Based on the Largest Lyapunov Exponent for Large Rotating Machine Equipments, *Journal of Beijing Institute of Technology*, Vol. 18, No. 4, pp. 433-436, 2009.

[6] Z. L Chen, H. X Wang and Y. Luo. *Wavelet Theory and Application*, Science Press, Beijing, 2004.

[7] Mallat S and Zhong S. Characterization of Signals from Multiscale Edges, *IEEE Transactions on pattern analysis and machine intelligence*, Vol. 14, No. 7, pp. 710-732, 1992.

[8] Burley S and Darnell M. Robust. Impulse Noise Suppression Using Adaptive Wavelet Denoising, *IEEE International Conference on Acoustics，Speech and Signal Processing*, pp. 3417-3420, 1997.

[9] W. Zhou. *MATLAB Wavelet Analysis Advanced Technology*, Xi'an University of Electronic Science and Technology Press, 2006.

[10] Y. Q Li, P. Li, X. P Yan and H. M Chen. Wavelet Transform Modulus Maximum Denoising Method for Radio Fuze Signal Processing, *Acta Armamentarii*, Vol. 29, No. 10, pp. 1172-1176, 2008.

[11] H. P Gong. Reserch on Several Issues of Wavelet Transform In Rotor Fault Diagnosis, 2008.

[12] C. Q Hua, Z. Ren and M. H Zhang. The Wavelet Maxima Denoising Based on the Adaptive Bayes Shrink Threshold, *Aerospace Control*, Vol. 29. No. 1, pp. 37-47, 2010.

[13] Mallat S. A Theory of Multiresolution Signal Decomposition: The Wavelet transform, *Pattern Analysis and Machine Intelligence*, Vol. 11, No. 7, pp. 673-693, 1989.

[14] T. Chen, X. L Xu and S. H Wang. Method of Wavelet Packet-Based Penalty Function Soft-Threshold to De-Noise Vibration Signals for Flue Gas Turbine, *Transactions of Beijing Institute of Technology*, Vol. 30, No. 8, pp. 906-914, 2010.

International Journal of Comprehensive Engineering
Part A, 2(1), 28-38, 2013
Doi: 10.14270/IJCE2013.2.1.a28
Regular paper

ISSN 2186-2680
e-ISSN 2186-2656
www.iace-journal.org

Intelligent Condition Diagnosis Method for Rotating Machinery Using Principal Component Analysis and Ant Colony Optimization

Hao Sun [1], Ke Li [2, #], Peng Chen [2, #]

[1] School of Mechanical Engineering, Jiangnan University, 1800 Li Hu Avenue, Wuxi, Jiangsu Province, 214122, China
[2] Graduate School of Bioresources, Mie University, Mie, 514-8507, Japan

[#] Corresponding author: dayanlv@live.cn, chen@bio.mie-u.ac.jp; Tel.: +81-592-319-592; Fax: +81-592-319-592

Abstract: This paper proposes a new intelligent fault diagnosis method for plant machinery developed by using principal component analysis (PCA) and ant colony optimization (ACO). The non-dimensional symptom parameters in the frequency domain are defined to reflect the features of vibration signals measured in each state. Sensitive evaluation method for selecting good symptom parameters using principal component analysis (PCA) is also proposed for detecting and distinguishing faults in rotating machinery. Moreover, to shorten the convergence time and improve the efficiency of ACO, the method of local search for the ACO is also presented here. Practical examples of diagnosis for V-belt driving equipment used in a centrifugal fan are provided to verify the effectiveness of the proposed method. The verification results show that the faults that often occur in V-belt driving equipment, such as pulley defect state, belt defect state, belt looseness state, etc., are effectively identified by the proposed method.

Keywords: Fault Diagnosis, Non-dimensional Symptom Parameter, Ant Colony Optimization, Synthetic Detection Index.

Received: May 12,2012 / Accepted: Nov. 6,2012 / Published: Apr. 8,2013

1. Introduction

In the field of condition-based maintenance, vibration diagnosis is often used for fault detection and state discrimination for rotating machinery. The condition diagnosis of rotating machinery depends largely on the feature analysis of vibration signals measured for the condition diagnosis because the signals carry dynamic information about the machine state [1]-[3]. The vibration signals in different states show different features, that is, when plant machinery is in an abnormal state, it will output sign sets corresponding to different faults [4]. If the vibration signals in each state can be automatically identified and classified using these features, intelligent condition diagnosis for plant machinery can be achieved.

In recent years, many studies on intelligent condition diagnosis for plant machinery using vibration signals have been reported, such as neural networks, support vector machines, etc. [5]-[10]. However, if the rotation speed and load of the plant machinery vary while vibration signals are being measured and a fault is in an early stage, the signal contains strong noise. Stronger noise than the actual failure signal may lead to misrecognition of useful information for the condition diagnosis, and there exist many ambiguous relationships between symptom parameters and failure types. Under such circumstances, the method for fault diagnosis using conventional intelligent methods, such as neural networks, support vector machines, etc., cannot judge state and reflect failure types correctly. In many cases, the neural networks or support vector machines never converges when learning with teacher data that have ambiguity [11].

Ant colony optimization (ACO) is a new simulative evolutionary algorithm that is also called ant colony system (ACS) [12]. ACO was firstly used for solving the traveling salesman problem (TSP) [13], and it has been

successfully applied to a large number of difficult problems, like the quadratic assignment problem (QAP) [14], routing in telecommunication networks, graph coloring problems, scheduling, etc. In recent years, ACO also has been applied to the clustering analysis problem and achieved excellent results. ACO is a kind of simulated evolutionary algorithm based on the positive feedback principle of information. It is strong in terms of robustness and can collect and classify all data according to the amount of information around the clustering center [15]-[18]. If the state identification for the condition diagnosis is converted to a clustering problem on the feature patterns of vibration signals under different states of rotating machinery, the condition diagnosis by ACO is possible.

For these reasons, this paper proposes a novel method of intelligent condition diagnosis for plant machinery developed by using principal component analysis (PCA) and ant colony optimization (ACO). The NSPs in the frequency domain are defined to reflect the features of vibration signals measured in each state. Sensitive evaluation method for selecting good symptom parameters using principal component analysis (PCA) is also proposed for detecting and distinguishing faults in rotating machinery. The PCA can be used to indicate the fitness of an NSP for ACO. Moreover, to reduce the convergence time of ACO to increase the processing efficiency, the method of local search for the ACO is also presented in this paper. Practical examples of diagnosis for V-belt driving equipment used in a centrifugal fan verify that the method is effective. The flowchart of the condition diagnostic procedure proposed in this paper is shown in Fig. 1.

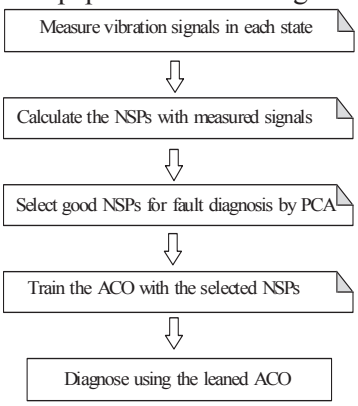

Fig. 1 Flowchart of the condition diagnosis

2. Non-Dimensional Symptom Parameters in The Frequency Domain for Condition Diagnosis

When a computer is used for condition diagnosis of plant machinery, symptom parameters (SPs) are required to express the information indicated by a signal measured for diagnosing machinery faults. A good symptom parameter can correctly reflect states and the condition trend of plant machinery [19]-[22]. Many symptom parameters have been defined in the pattern recognition field. In this study, through analyzing the spectral features of V-belt driving equipment in abnormal states, the eight NSPs in the frequency domain for the condition diagnosis of V-belt driving equipment are defined.

$$p_1 = \sum_{i=1}^{I} F(f_i)/I \tag{1}$$

$$p_2 = \sqrt[I]{\prod_{i=1}^{I} F(f_i)} \tag{2}$$

$$p_3 = \frac{\sum_{i=1}^{I} (f_i - \bar{f})^3 \cdot F(f_i)}{\sigma^3 I} \tag{3}$$

$$p_4 = \frac{\sum_{i=1}^{I} (f_i - \bar{f})^4 \cdot F(f_i)}{\sigma^4 \cdot I} \tag{4}$$

$$p_5 = \sqrt{\frac{\sum_{i=1}^{I} f_i^4 \cdot F(f_i)}{\sum_{i=1}^{I} f_i^2 \cdot F(f_i)}} \tag{5}$$

$$p_6 = \frac{\sum_{i=1}^{I} f_i^2 \cdot F(f_i)}{\sqrt{\sum_{i=1}^{I} F(f_i) \sum_{i=1}^{I} f_i^4 \cdot F(f_i)}} \tag{6}$$

$$p_7 = \frac{\sum_{i=1}^{I} \sqrt{(f_i - \bar{f})} \cdot F(f_i)}{\sqrt{\sigma} \cdot I} \tag{7}$$

$$p_8 = \sqrt{\sum_{i=1}^{I} F^2(f_i)} \tag{8}$$

Here, $\bar{f}$ is the mean value of the analysis frequency

$$\bar{f} = \frac{\sum_{i=1}^{I} f_i \cdot F(f_i)}{\sum_{i=1}^{I} F(f_i)} \tag{9}$$

σ is the standard deviation

$$\sigma = \sqrt{\frac{\sum_{i=1}^{I} (f_i - \bar{f})^2 \cdot F(f_i)}{I}} \tag{10}$$

3. Synthetic Detection Index for Evaluating Symptom Parameters

PCA is a mathematical procedure that uses an orthogonal transformation to convert a set of observations of possibly correlated variables into a set of values of uncorrelated variables called principal components. PCA was invented in 1901 by Karl Pearson. Now it is mostly used as a tool in exploratory data analysis and for making predictive models. PCA can be done by eigenvalue decomposition of a data covariance matrix or the singular value decomposition of a data matrix. These decompositions are usually performed after mean centering the data for each attribute. The results of a PCA are usually discussed in terms of component scores and loadings [23]. In the last few years, PCA has been applied to process fault diagnosis (identification) [24-26].

Define a data matrix with size m x n, where m is the number of identifying states and n is the number of symptom parameters, whose covariance matrix has eigenvalue λi and eigenvector ai and i=1-n with $\lambda 1 \geq \lambda 2 \geq \ldots \geq \lambda n$. Principal components Zi and the cumulative contribution rate of the principal components ηi can be calculated as follows:

$$\begin{Bmatrix} Z_1 \\ \vdots \\ Z_n \end{Bmatrix} = \begin{bmatrix} a_{11} & \cdots & a_{1n} \\ \vdots & \ddots & \vdots \\ a_{m1} & \cdots & a_{mn} \end{bmatrix} \begin{Bmatrix} P_1 \\ \vdots \\ P_n \end{Bmatrix} = AP \tag{11}$$

$$\eta_i = \frac{\sum_{j=1}^{i} \lambda_j}{\sum_{k=1}^{n} \lambda_k} \tag{12}$$

Where λi is the standard deviation of the principal component, aji is the weight coefficient of the principal component, Pi is a symptom parameter, i=1-n and j=1-m.

Using PCA, original data can be converted into many principal components. The first few principal components contain most of the information and the discriminatory features. The weight coefficient of the principal components can express the importance of the symptom parameters for each principal component. Therefore, the symptom parameters that have high sensitivity for detecting faults can be selected by the weight coefficient for the first few principal components.

4. Intelligent Condition Diagnosis Method Using Ant Colony Optimization (ACO)

In order to effectively and automatically distinguish faults for condition monitoring of rotating machinery, a new intelligent condition diagnosis method is proposed based on the NSPs and the ACO, that is, the problem of state identification for the condition diagnosis is converted into the clustering problem of the NSPs calculated by vibration signals measured in different states, which will be solved by the ACO.

4.1. Ant Colony Optimization (ACO)

The ACO algorithm introduced by Marco Dorigo in his PhD thesis is a population-based meta-heuristic that can be used to find approximate solutions to difficult optimization problems. The ACO algorithm is inspired by the behavior of ants while finding paths from the colony to food.

Ants have no sight and are capable of finding the shortest route between a food source and their nest by chemical materials called pheromone that they leave when moving [27]. A moving ant lays some pheromone on the ground, thus making a trail of this substance. While an isolated ant moves practically at random, an ant encountering a previously laid trail can detect it and decide with high probability to follow it and reinforce the trail with its own pheromone. What emerges is a form of an autocatalytic process through which the greater the number of ants that follow a particular trail makes that trail more attractive to be followed. The process is thus characterized by a positive feedback loop, during which the probability of choosing a path increases with the number of ants that previously chose the same path.

ACO is a kind of heuristic algorithm with global optimization, which combines distributed computing and positive feedback mechanisms and has the following virtues:

(1)Stronger robustness: ACO can transplant other problems, especially all kinds of assembled optimized problems.

(2)Greater ability to find the better result: The algorithm adopts the positive feedback principle, which quickens the evolution processing and does not become trapped in local optima.

(3)Distributing parallelism calculating: ACO is an evolution algorithm based on ant colonies and has parallelism base on them. The individual ants can continue to exchange and transfer the information (pheromone), which can lead to a better result.

(4)It is easy to combine ACO with other methods: The algorithm can integrate other enlightened methods to improve the performance of the algorithm.

4.2. ACO for Condition Diagnosis

Assume that N is the number of sample sets of vibration signals measured in m different states, the length of which is n, $N = \{x_1, x_2 \cdots x_n\}$.Every sample signal has t indentified symptoms (in this paper, P1~P8). Then, the clustering analysis is to divide n sample data into m states, such that the objective function F shown in Formula (19) is minimized.

$$\min F = \sum_{j=1}^{m}\sum_{i=1}^{n}\sum_{k=1}^{t} a_{ij}\left\|x_{ik} - c_{jk}\right\|^2 \tag{13}$$

Here, cjk is the clustering center, and

$$c_{jk} = \frac{\sum_{i=1}^{n} a_{ij} x_{ik}}{\sum_{i=1}^{n} a_{ij}} \qquad (j = 1,2\cdots m; k = 1,2\cdots t) \tag{14}$$

$$a_{ij} = \begin{cases} 1 & if\ x_i \in state\ j \\ 0 & if\ x_i \notin state\ j \end{cases} \qquad (i = 1,2\cdots n; j = 1,2\cdots m) \tag{15}$$

In this paper, the procedure for applying the ACO for the condition diagnosis is proposed as shown in Fig. 2, and the procedure is explained as follows:

(1) NSPs used for reflecting the features of sample signals are inputted into the ACO.
(2) Sample signals are randomly classified by artificial ants (artificial ants construct solutions), and the pheromone matrix is initialized.
(3) According to the solutions, clustering centers are calculated by Formula (20), and the object function of every solution is calculated by Formula (19).
(4) Local search (refer to section 4.4).
(5) The pheromone matrix is updated (refer to section 4.5).
(6) According to pheromone matrix, artificial ants update the solutions (refer to section 4.3).
(7) Step (3)-(6) are looped until the ending condition is satisfied.

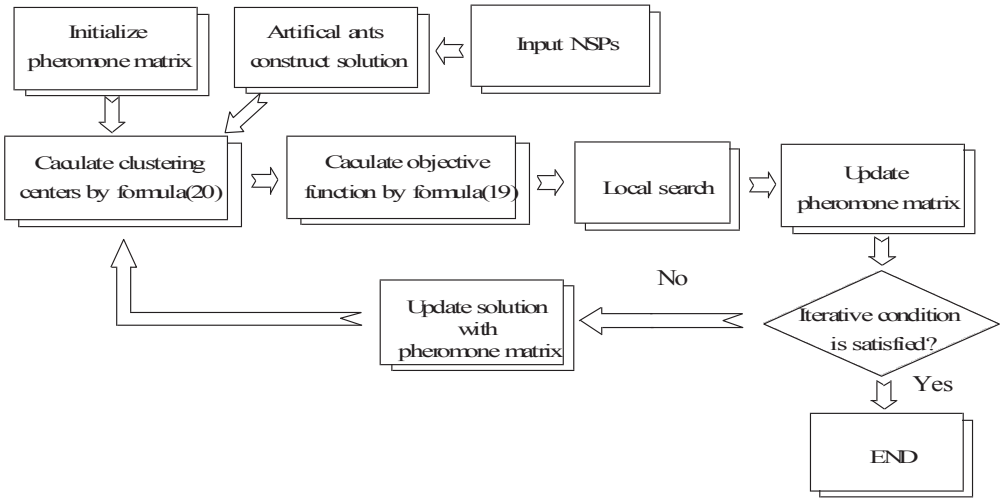

Fig. 2 Flowchart of ACO for condition diagnosis

4.3. Construction and Update of Solutions

In the ACO, every artificial ant will construct the solution S with a length of n and $S = \{c_i | i = 1,2\cdots n\}$ $c_i \in \{1,2\cdots m\}$, where ci is the classification result of sample xi. That is, if ci =j, then xi is the output vibration data in state j. At the start of the ACO, the solutions S are randomly constructed by artificial ants, and with the increase of the iteration number, artificial ants update the solutions incessantly according to the pheromone matrix information, followed by the principles given as follows:

$$S = \arg\max\{\tau_{ij} \times [\eta_{ij}]^{\beta}\} \quad if\ q \le q_o \tag{16}$$

$$\eta_{ij} = \frac{1}{d_{ij}} \tag{17}$$

where , dij is the Euclidean distance between clustering center j and sample xi, and

$$d_{ij} = \sqrt{\sum_{k=1}^{t} (x_{ik} - c_{jk})^2} \tag{18}$$

Here, q is a value chosen randomly with a uniform probability between 0~1, qo is constant, 0<qo<1, τij represents the pheromone concentration of sample xi associated with the state j and β is a parameter that determines the relative importance of heuristic information (the choice of β is determined experimentally, and β > 0).

If qo<q, the artificial ants choose the state for sample xi by the conversion probability pij given as follows:

$$p_{ij} = \frac{\tau_{ij} \times [\eta_{ij}]^{\beta}}{\sum_{s=1}^{m} \tau_{is} \times [\eta_{is}]^{\beta}} \tag{19}$$

4.4. Local Search

To improve the efficiency and accelerate the convergence speed of the ACO, the method of local search for the ACO is presented. The local search method is conducted on all solutions or some solutions [28] [29]. In this paper, the latter is applied, that is, local search is implemented only for the ten solutions with smaller objective functions. The execution process of the local search for the ACO is as follows:

(1) All solutions are arranged in ascending order according to the values of the objective function.
(2) Random data Wi $\{i = 1,2 \cdots n\}$ for every sample are produced automatically.
(3) A weight P is set, and 0< P <1.
(4) P is compared with Wi , if P> Wi, and then the sample xi is reclassified.
(5) The Euclidean distance between sample xi and every clustering center is calculated, and the shortest distance is for the class of sample xi.
(6) Formula (19) is used to compute the objective function again and compare it with the former objective function values. If the new one is lower than the former one, the new solution sets are kept, or the former solution sets are reduced.
(7) Steps (2)-(6) are looped until the ten solutions are calculated.

4.5. Update Pheromone Matrix

M.Dorigo proposed three different models: the ant-cycle system, the ant-quantity system and the ant-density system [30]. In this research, the ant-cycle system is used to update the pheromone. In the ant-cycle system, the pheromone is released after the artificial ant builds all information. It utilizes all information. However, the other two systems utilize only partial information. Thus, this system is better than the ant-quantity system and the ant-density system. The pheromone will be updated by the ten artificial ants that have smaller object functions, and the updating principle is as follows:

$$\tau_{ij}(l+1) = (1-\rho)\tau_{ij}(l) + \sum_{a=1}^{10} \Delta\tau_{ij(a)} \tag{20}$$

$$\Delta\tau_{ij(a)} = \begin{cases} \dfrac{1}{F_a} & x_i \in statej \\ 0 & otherwire \end{cases} \tag{21}$$

$$F_a = \sum_{j=1}^{m} \sum_{i=1}^{n} \sum_{k=1}^{t} \left\| x_{ik} - c_{jk} \right\|^2 \tag{22}$$

Here, τij represents the pheromone concentration of sample xi associated with the state j, ρ is the decay parameter of the pheromone and, to prevent pheromone excessive accumulation 0<ρ<1, Δτij(a) is the pheromone values of artificial ant a.

From Formulas (26)-(28), if sample xi $\in$ state j, with increasing iteration number, then the pheromone τij becomes greater and finally approaches the saturation level. On the contrary, if sample xi $\notin$ state j, with increasing iteration number, then the pheromone τij becomes smaller and finally approaches 0.

5. Condition diagnosis for V-Belt Driving Equipment Using the ACO

In this section, the condition diagnosis for V-belt driving equipment using the ACO is shown to verify that the method proposed in this paper is effective.

5.1. Experimental System

Fig.3 shows the V-belt driving equipment used in the centrifugal fan for the diagnosis test, and an accelerometer (PCB MA352A60) with a bandwidth from 5 Hz to 60 kHz and 10 mV/g output was used to measure the vibration signals of the vertical direction in normal (N), pulley defect (PD), belt defect (BD) and belt looseness (L) states. The vibration signals measured by the accelerometer were transformed into the signal

recorder (Scope Coder DL750) after being magnified by the sensor signal conditioner (PCB ICP Model 480C02). The original vibration signals in each state were measured at a constant speed (800 rpm). The sampling frequency of the signal measurement was 50 kHz, and the sampling time was 20 s. The necessary information about the V-belt driving equipment is listed in Table 1.

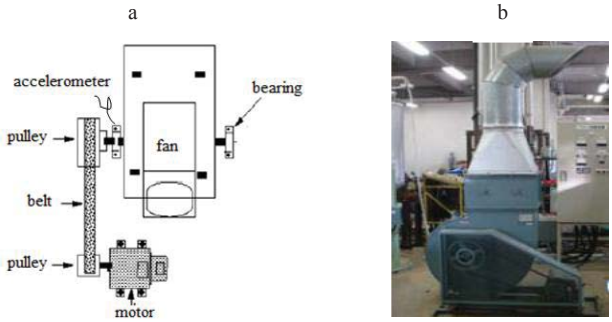

Fig. 3 The centrifugal fan for the condition diagnosis: (a) illustration of the centrifugal fan and (b) photograph of the centrifugal fan.

Table 1 V-belt driving equipment information for diagnosis test

Contents	Parameters
Pulley radius (small) ra	70 mm
Pulley radius (large) rb	140 mm
Belt span L	701.5 mm
Contact angle (small pulley) âa	169°

In this study, using the method of PCA, NSPs that contain the most information and have high sensitivity for detecting and distinguishing faults in rotating machinery are selected. As an example, parts of the selection results are shown in Table 2. From Table 2, P2, P7 and P8 are better for distinguishing the normal (N), pulley defect (PD), belt defect (BD) and belt looseness (L) states. Because the weight coefficients for P2 , P7 and P8, the first principal component, are larger than those of the other, the contribution rate of the first principal component is 85.68%, which contains enough information and discriminatory features to identify the normal (N), pulley defect (PD), belt defect (BD) and belt looseness (L) states.

Table 2 Selection results of NSPs

NSPs	Component1	Component2	Component3
P1	-0.4768	0.6784	0.0321
P2	0.9976	-0.9547	0.1293
P3	-0.2680	0.0753	0.0745
P4	0.3012	0.0599	0.0344
P5	-0.9210	0.2312	0.3136
P6	-0.9785	-0.1752	-0.1092
P7	0.9904	0.1365	0.0205
P8	0.9924	0.0657	0.1041
η	0.8568	0.1249	0.0183

5.2. Diagnosis by the proposed method

The main procedure for fault diagnosis using NSPs and ACO was introduced in Section 1 (refer to Fig.1). First, the vibration signals are measured in each known state. Second, the NSPs are calculated using Formulas (7)-(14). The highly sensitive NSPs (P2, P7, P8) are selected for condition diagnosis by PCA. Third, the ACO is trained with P2, P7, P8, and the optimal clustering centers are obtained. Lastly, the condition of the V-belt driving equipment can be diagnosed by the trained ACO and NSPs.

In this study, the state identification for the condition diagnosis is converted to a clustering problem for the values of the NSPs calculated from vibration signals under different states of the V-belt driving equipment. The ACO automatically finds the optimal clustering centers and classify all sample data according to the amount of information around the clustering centers. The purpose of training the ACO is the acquisition of optimum clustering centers. P2, P7 and P8 calculated using the vibration signals measured in each known state were input

into the ACO. After about 150 iterations, the ACO converged to the optimum clustering centers. Fig. 5 shows the change of the clustering centers while training the ACO for the condition diagnosis of the V-belt driving equipment.

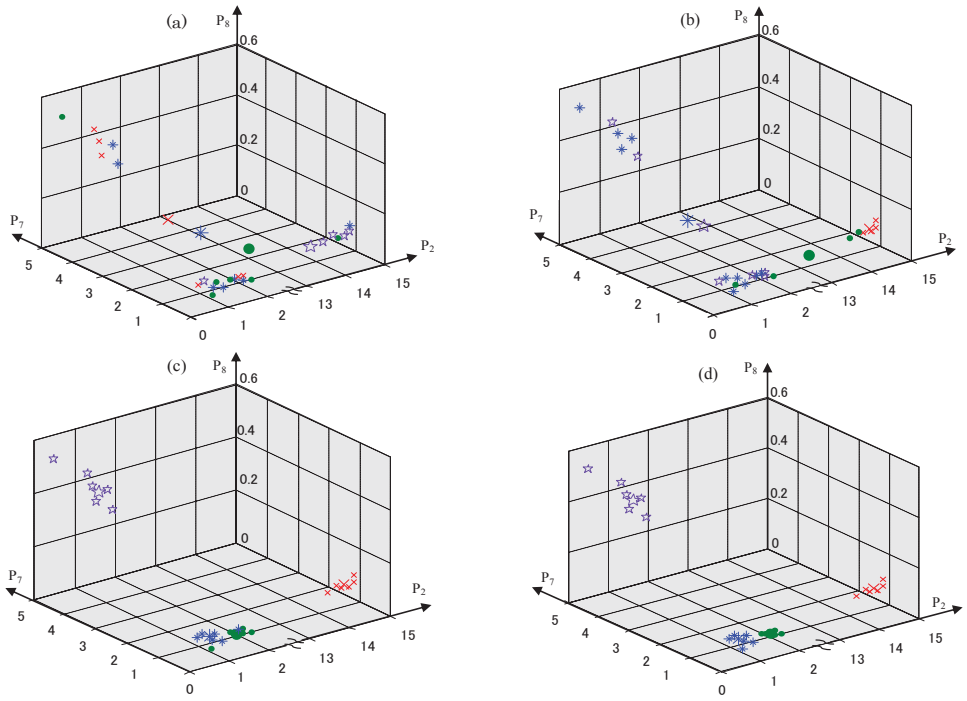

Fig. 5 The change of the clustering centers while training the ACO for the condition diagnosis of the V-belt driving equipment. (a) At the start of the ACO, (b) after 50 iterations, (c) after 100 iterations and (d) after 150 iterations.

Here, the symbols ☆, ✳, × and ○ express the value samples of NSPs in the normal state, pulley defect state, belt defect state and belt looseness state, respectively, and the big symbols represent their clustering centers.

In the training process of the ACO, at first, the sample data are classified into normal, pulley defect, belt defect and belt looseness states randomly. The clustering centers and the sum of the spatial distance between every sample data and the clustering centers are calculated by Formulas (19)-(21). With increasing iterations, the pheromone is updated incessantly, and according to the pheromone information, the classification of the sample data and clustering centers are also updated by artificial ants. Finally, the optimal clustering centers with a minimum sum of spatial distances are calculated. As an example, parts of the training data and their clustering centers are shown in Table 3.

Table 3 Parts of acquired knowledge of diagnosis for the ACO

(a) Normal state

NSPs			Clustering Center		
P2	P7	P8	x	y	z
0.786	0.677	0.078	0.851	0.680	0.080
0.899	0.678	0.080			
0.831	0.696	0.083			
……	……	……			

(b) Pulley defect state

NSPs			Clustering Center		
P2	P7	P8	x	y	z
0.331	3.518	0.377	0.471	3.660	0.501
0.417	3.783	0.497			
0.537	3.637	0.519			
……	……	……			

(c) Belt defect state

NSPs			Clustering Center		
P2	P7	P8	x	y	z
14.56	0.63	0.15	14.98	0.61	0.14
15.13	0.60	0.14			
14.78	0.58	0.14			
……	……	……			

(d) Belt looseness state

NSPs			Clustering Center		
P2	P7	P8	x	y	z
1.255	0.768	0.060	1.177	0.740	0.064
1.187	0.747	0.067			
1.323	0.707	0.058			

Here, x is the coordinate value of the clustering center on the P2 axis, y is the coordinate value of the clustering center on the P7 axis, and z is the coordinate value of the clustering center on the P8 axis.

After training the ACO, to verify the diagnostic capability of the method proposed in this paper, the test data measured in each known state that had not been used to train the ACO were used. When inputting the test data into the trained ACO, the ACO classified the test data according to the information of the optimum clustering centers shown in Table 3 and correctly and quickly output identification results based on the pheromone values of the corresponding states. As an example, Fig. 6 shows the parts of the test data classified according to the information of the optimum clustering centers shown in Table 3. Fig. 7 shows the change of the pheromones for distinguishing the normal state from abnormal states with increasing iterations. Fig. 7 shows that the pheromone of the normal state gradually increases and finally approaches the saturation level. On the contrary, the pheromones of each abnormal state gradually decrease and finally approach 0. Some diagnosis results are listed in Table 4. These results verified the efficiency of the intelligent diagnosis method using NSPs and the ACO proposed in this paper.

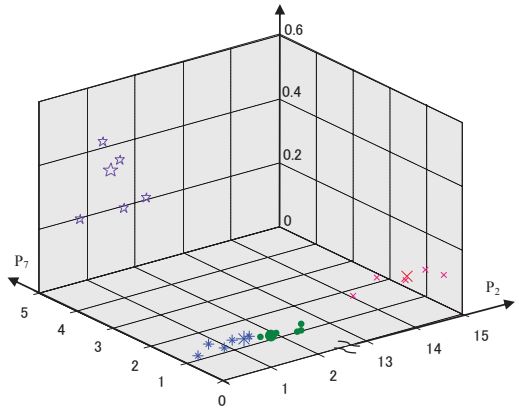

Fig. 6 Classification of the test signals

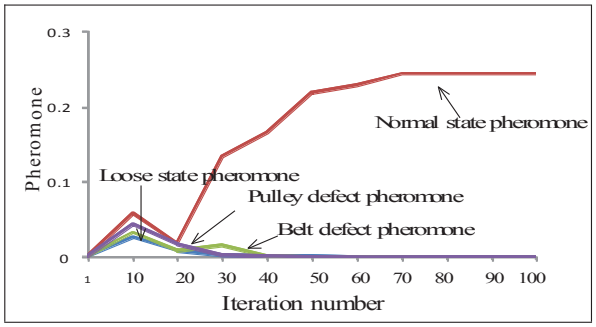

Fig. 7 Pheromones for distinguishing the normal state from abnormal states

Table 4 Diagnosis results using the proposed method

NSPs			Pheromone				Judge
P2	P7	P8	N	PD	BD	L	
0.846	0.678	0.077	0.2445115	0.0000284	0.0005955	0.0000063	N
0.895	0.694	0.081	0.2439221	0.0000667	0.0011466	0.0000063	N
0.483	3.784	0.500	0.0000108	0.2451184	0.0000063	0.0000063	PD
0.537	3.595	0.457	0.0001432	0.2449803	0.0000118	0.0000063	PD
13.909	0.602	0.143	0.0000063	0.0003846	0.2447445	0.0000063	BD
14.751	0.619	0.146	0.0000063	0.0000063	0.2451228	0.0000063	BD
1.323	0.751	0.066	0.0000064	0.0000063	0.0000063	0.2451227	L
1.035	0.731	0.063	0.0000063	0.0000063	0.0000063	0.2451228	L
……	……	……	……	……	……	……	……

6. Conclusion

In this research, the state identification for the condition diagnosis of rotating machinery was converted to a clustering problem of the values of the non-dimensional symptom parameters (NSPs) in the frequency domain, as calculated from vibration signals in different states of the machine, and ant colony optimization (ACO) was introduced for this purpose. The eight non-dimensional symptom parameters in the frequency domain were defined and could reflect the characteristics of vibration signals measured for the fault diagnosis of rotating machinery. Sensitive evaluation method for selecting good symptom parameters using principal component analysis (PCA) is also proposed for detecting and distinguishing faults in rotating machinery. The PCA can be used to indicate the fitness of an NSP for ACO. Moreover, to reduce the convergence time of the ACO to increase the processing efficiency, the method of local search for the ACO was also presented in this paper. Practical examples of diagnosis of V-belt driving equipment verified the effectiveness of the proposed method.

The diagnosis results showed the faults that often occur in V-belt driving equipment, such as the pulley defect state, belt defect state, belt looseness state, etc., were automatically and effectively identified by the proposed method.

References

[1] B. Liu and S. F. Ling. On the Selection of Informative Wavelets for Machinery Diagnosis, *Mechanical Systems and Signal Processing*, Vol. 13, pp. 145-162, 1999.

[2] L. Jing and Q. Liangsheng. Feature Extraction Based on Morlet Wavelet and Its Application for Mechanical Fault Diagnosis, *Journal of Sound and Vibration*, Vol. 234, pp. 135-148, 2000.

[3] Q. B. Zhu. Gear Fault Diagnosis System Based on Wavelet Neural Networks, *Dynamics of Continuous Discrete and Impulsive Systems-series A-Mathematical Analysis. Part 2 Suppl. S*, Vol. 13, pp. 671-673, 2006.

[4] P. Chen, Toshio Toyota and Z. J He. Automated Function Generation of Symptom Parameters and Application to Fault Diagnosis of Machinery in Variable Operation-conditions, *IEEE Transactions on System, Man, and Cybernetics (Part A)*, Vol. 31, pp. 775-781, 2001.

[5] B. Samanta and K. R. Al-Balushi. Artificial Neural Network Based Fault Diagnostics of Rolling Element Bearings Using Time-Domain Features, *Mechanical Systems and Signal Processing*, Vol. 17, pp. 317-328, 2003.

[6] A. C. McCormick and A. K. Nandi. Real-Time Classification of the Rotating Shaft Loading Conditions Using Artificial Neural Networks, *IEEE Transactions on Neural Networks*, Vol. 8, pp. 748-756, 1997.

[7] B. Samanta, K. R. Al-Balushi and S. A. Al-Araimi. Artificial Neural Networks and Genetic Algorithm for Bearing Fault Detection, *Soft Computing*. Vol. 10, pp. 264-271, 2006.

[8] R. Q. Li, J. Chen and X. Wu. Fault Diagnosis of Rotating Machinery Using Knowledge-Based Fuzzy Neural Network, *Applied Mathematics and Mechanics*, Vol. 27, pp. 99-108, 2006.

[9] V. Schetinin and J. Schult. Learning Polynomial Networks for Classification of Clinical Electroencephalograms, *Soft Computing*, Vol. 10, pp. 397-403, 2006.

[10] R.M. Fang. Fault Diagnosis of Induction Machine Using Artificial Neural Network and Support Vector Machine, *Dynamics of Continuous Discrete and Impulsive Systems-series A-Mathematical Analysis. Part 2 Suppl. S*, Vol. 13, pp. 658-661, 2006.

[11] C. Bishop, M. I. *Neural Networks for Pattern Recognition*, Oxford University Press, 1995.

[12] Dorigo M. *Optimization*, *Learning and Natural Algorithms*, PhD thesis, Dipartimento di Elettronica, Politecnico di Milano, Italy, 1992.

[13] Dorigo M, Maniezzo Vand Colorni A. The Ant System: Optimization by a Colony of Cooperating Agents, *IEEE Transaction on Systems, Man, and Cybernetics-Part B*, Vol. 26, pp. 29-41, 1996.

[14] Maniezzo V and Colorni A . The Ant System Applied to the Quadratic Assignment Problem, *IEEE Transaction on Knowledge and Data Engineering*, Vol. 11, pp. 769-778, 1999.

[15] Dorigo M and Gambardellal M. A Study of Some Properties Of Ant-Q, *In proceedings of the 44th International Conference on Parallel Problem Solving from Natural, Springer-Verlag* , 1996.

[16] Dorigo M and Gambardellal M. Ant Colony System : A Cooperative Learning Approaches to The Traveling Sales Man Problem , *IEEE Transaction on Evolutionary Computation*, Vol. 1, pp. 53-66, 1997.

[17] Dorigo M, Boeabeau E and Theraola G. Ant Algorithms and Stigmergy, *Future Generation Computer System.* Vol. 16, pp. 851- 871, 2000.

[18] D Costa and A Hertz. Ants Can Color Graphs, *Journal of the operational Research Society*, Vol. 48, pp. 295-30, 1997.

[19] J. J. RICHARDSON. *Artificial Intelligence in Maintenance*, Noyes Publications, N. J. , 1985.

[20] H. Matuyama. Diagnosis Algorithm, *Journal of JSPE*, Vol. 75, pp. 35-37, 1991.

[21] P. Chen, T. Toyota. Fuzzy Diagnosis and Fuzzy Navigation for Plant Inspection and Diagnosis Robot, *Proc. of FUZZ-IEEE/IFES'95*, Vol. 1, pp. 185-193, 1995.

[22] Fukunaga, K. *Introduction to Statistical Pattern Recognition*, Academic Press: San Diego, CA, USA, 1972.

[23] Jolliffe, I. T. Principal Component Analysis, *Springer-Verlag*. pp. 487, doi:10.1007/b98835, 1986.

[24] Johannesmeyer, M.C., Singhal, A. and Seborg, D. E.. Pattern Matching in Historical Data, *AIChE journal,* Vol. 48, pp. 2022-2038 , 2002.

[25] Kano, M., Tanaka, S., Hasebe, S., Hashimoto, I. and Ohno, H.. Monitoring Independent Components for Fault Detection, *AIChE journal*, Vol. 49, pp. 969-976, 2003.

[26] Lu, N., Wang, F. and Gao, F.. Combination Method of Principal Component and Wavelet Analysis for Multivariate Process Monitoring and Fault Diagnosis, *Industrial & engineering chemistry research,* Vol. 42, pp. 4198-4207, 2003.

[27] Bonabeau E, Dorigo M and Theraulaz G. *Swarm Intelligence: from Natural to Artificial Systems*, Oxford University Press, New York, 1999.

[28] Stfitzle T and Hoos H. The MAX-MIN ant system and local search for the traveling salesman problem, *IEEE International Conference on Evolutionary Computation*. pp. 309-314, 1997.

[29] F. J Qin, W. F Tian and An Li . Decision-making in Multi-fault State Complex System Based on Ant Colony Algorithm. *Journal of Chinese Inertial Technology*, Vol. 4, pp.12-15, 2004.

[30] M Dorigo, V Maniezzo and A Colorni. "Positive Feedback as a Search Strategy," Dipartimento di Elettronica, Politecnico di Milano, Italy, Technical Report. pp. 91-016,1991.

International Journal of Comprehensive Engineering
Part A, 2(1), 39-44, 2013
Doi: 10.14270/IJCE2013.2.1.a39
Regular paper

ISSN 2186-2680
e-ISSN 2186-2656
www.iace-journal.org

Research of Reducing Unbalanced Vibration in Rotating Machinery by Damping Technology

Jian Chang [#], Lidong He, Wei Hao, Mei Liu and Zhenkun Zhang

[1] School of Mechanical & Electrical Engineering, Beijing University of Chemical Technology, Beijing, 100029, China

[#] Corresponding author: he63@263.net; Tel.: +86-13910766781; Fax: +86-010-64446043

Abstract: The research of the unbalanced vibration controlling method has largely concentrated on changing the system's quality and stiffness or optimizing the bearing's damping parameters. In this paper, a newly designed damping device was utilized on an experimental rig to decrease the rotor's vibration. The aim of the study was to investigate the influence of damping liquid on reducing the vibration amplitude. After changing a series of damping liquid, the experiment reached the aim of proving that the new device could decrease the vibration obviously. It was demonstrated that the viscosity of the damping liquid was a key element to control the unbalance vibration. Furthermore, in order to prove that the damping device could be utilized at different unbalanced working situations, six different kinds of counterweight were designed to test the adaptability of the new design. This, in turn, is found that the damping device has a profound effect to amounts of unbalanced working situations. And a series of conclusions and findings could be harvested from the experiments. The reported findings are backed by the evidence from the test fig.

Keywords: Rotating Machinery, Unbalanced Vibration, Damping Liquid, Counterweight.

Received: May 16,2012 / Accepted: Nov. 6,2012 / Published: Apr. 8,2013

1. Introduction

The vibration problem existing in modern high-speed rotating machinery has become an extremely prominent and intractable problem. And the vibration amplitude is one of the key elements to decide the reliability of most rotating mechanical productions [1]. For the unbalance rotors, the ordinary method is to balance the rotor on dynamic balancing machines. In order to avoid disassemble the rotor, it's allowed to use field dynamic balancing technology. But mostly, that method would cost too much resource and expenditure [2]. Although magnetic bearing can decrease vibration through active power control, its reliability would be the main problem in factory [3-4]. All these traditional ideas of solutions attend to reduce vibration from changing the distribution of the unbalance mass on the rotor.

The typical example of utilizing damping force to decrease rotating machinery vibration is Squeeze-film damper (SFD) technology, which is widely used on aircraft engines' rotors. Squeeze-film damper (SFD) can effectively restrain the vibration of the rotor and improve the stability of the whole system, at the same time decrease the exciting force exporting from the bearings. But this technology only has remarkable effect at the critical speed of the rotor, does little to the other range of the speed [5-7].

Meanwhile, the traditional damping technology receives a series of success in other non-rotating equipment area, such as architecture and petrochemical fields. Tuned mass damper (TMD) is studied to minimize wind-induced vibration on the towering equipment [8-10]. Some scholars already use damping devices to solve the vibration problems happening on the pipelines of compressors [11-12].

The research method in this article tries to add a new particular damping device onto the rotating machinery, expecting the new damping device could be applicable on whole rotating speed range. The vibration energy generated in the system could be transferred to the damping device. Through changing parameters, including

viscosity of the damping liquid and the counterweights on the rotor, the study receives a series of data to analysis the damping technology's effect to the rotor. Results can provide some experimental basis and explore a new way to solve the unbalanced vibration problem in rotating machinery.

2. Damping Technology Theory

In rotor system, because of the existing of exciting force, the dynamic equation of the system becomes a non-homogeneous equation as follows:

$$m\ddot{x} + c\dot{x} + kx = F_0(t) \tag{1}$$

In Eq.(1), *m*, *c*, *k* are the system's mass, damping, and stiffness; $\ddot{x}$, $\dot{x}$, x are acceleration, speed and displacement; $F_0(t)$ is the outer harmonic exciting force of the rotor.

Generally, the primary method of vibration reduction in rotating machinery is concentrating on changing system's mass and stiffness. There are two paths to reach the aim, one is increasing the quality of the rotating parts to increase m, and the other is improving the stiffness at support location to increase *k*. These two ways decrease $\ddot{x}$, $\dot{x}$, x, getting the result of reducing rotor's vibration.

In the meantime, several researchers discuss the theory of Squeeze-film damper (SFD) which has great effect to restrain the system's vibration at the critical speed. These studies intend to optimize the bearing's various parameters but not to reduce the damping value of the whole system. In order to estimate the effect of whole system's damping on the vibration, it is assumed that after installing damping device the additional damping force has uniform influence as system's existing damping. Both sides of Eq.(1) are divided by m, a standard motion Eq.(2) could be received as follows:

$$\ddot{x} + 2\zeta\omega_0\dot{x} + \omega_0^2 x = \frac{1}{m}F_0(t) \tag{2}$$

$\omega_0 = \sqrt{k/m}$ is system's natural frequency, $\zeta = c/2\sqrt{km}$ is damping ratio. Equation's right side is assumed to be unchangeable. Meanwhile, *k* and *m* are definite values. The only way to decrease system's acceleration, speed and displacement is improving ζ. Because damping ratio ζ is proportional to damping value *c*, in theory analysis, improving damping liquid viscosity could decrease vibration of the rotating machinery. In this research, the experiment concentrates on increasing system's damping value, using damping device to control the unbalanced vibration.

3. Test Apparatus

Fig. 1 is a rotor vibration control system schematic diagram. Whole system was composed by a rotor speed controller, a driving motor, a rotor test rig, two sensors, a damping device, an OR38 dynamic signal analyzer and a computer.

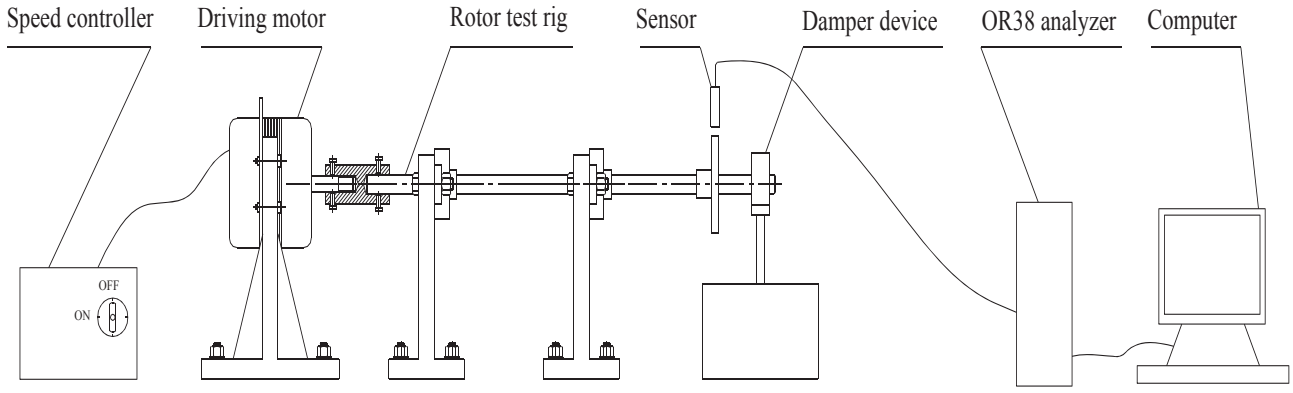

Fig. 1 Principle sketch of the rotor vibration control system

In this article, a new experimental rig had been built, as in Fig. 2. The rotor system was supported by the driving motor and the two bearing seats. The diameter of the rotating shaft was 10mm, the length of it was 270mm, bearings span was 102mm, and a disk with 50mm diameter was fixed on the shaft which was next to

bearing2 with 57mm. The disk had eight thread holes homogeneously distributing on the edge so as to fix counterweight to simulate unbalance mass on it. The damping device was placed on the shaft having 40mm distance to the end. The authors installed two Bently eddy current sensors to collect vibration data of the X and Y directions, then analyzed the effect of the damping device.

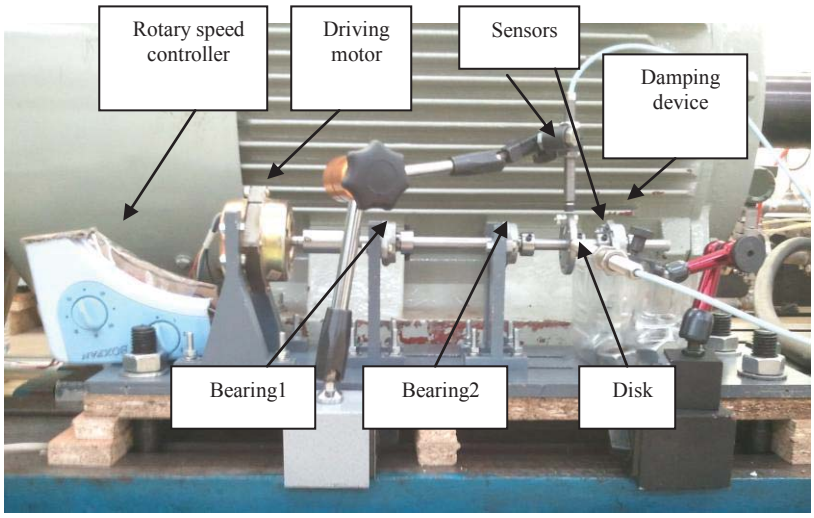

Fig. 2 A new experimental rig of damping vibration control system

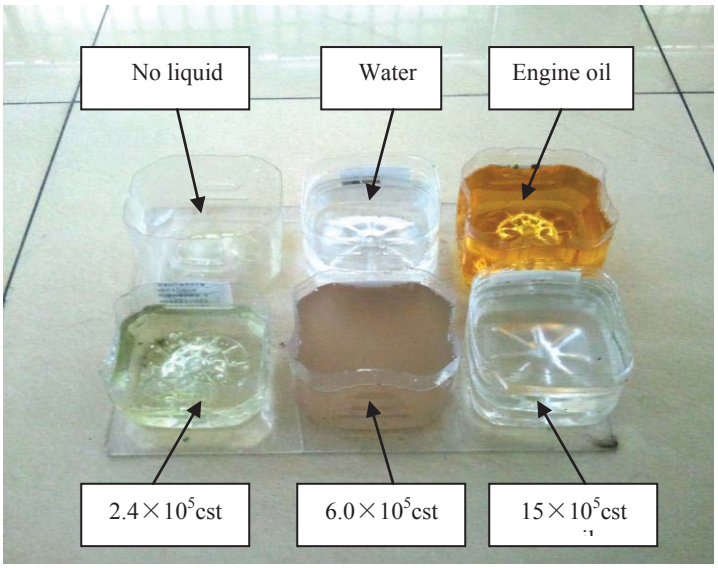

Fig. 3 Six experiment damping situations

4. Experiment Analysis and Results

4.1 Effect of Damping Liquid Viscosity on Rotor's Vibration

The damping device was constituted by a rolling bearing and a pair of high strength organic glass bars which immersing in the damping liquid. The experiment designs six different damping situations, including no liquid as the basis comparing group. The other five ones can be divided into two parts. First part is the common liquid, including water and engine oil whose viscosity values are 1cst and 32cst respectively. And the second part includes three polymeric liquid whose viscosity values are 2.4×10^5cst, 6.0×10^5cst and 15×10^5cst respectively. The six damping situations are shown in Fig. 3. And for easy to note, they are numbered in Table 1. Rotor speed was 1320rpm, the experiment were taking without balance weight on the disk. Each situation could be tested five times, each time lasted 60 seconds. Without changing the structure of the rotor system and counterweight, the research compared the rotor's different vibration data causing by the six different kinds of damping situations. Fig. 4 shows the damping viscosity's effect to rotor's vibration.

Comparing with no liquid situation, water caused vibration a little bit more in X direction, all the other damping liquid reduced vibration amplitude obviously. The 15×10^5cst damping liquid reduced vibration amplitude from 87um to 70um at X direction and it also reduced vibration amplitude from 112um to 82um at Y

direction, which separately decreased approximately 19.5% and 26.8%. Curves in Fig. 4 certified that, water and engine oil are low viscosity damping liquid which do little effect to the vibration, even could play an opposite role. That is because both water and engine oil have very low viscosity, their c value are too less to affect the vibration. In contrast, fluid-solid coupling phenomenon may happen, and influence the vibration severely. 2.4×10^5cst, 6.0×10^5cst, and 15×10^5cst damping liquid have extremely higher viscosity compared with water and engine oil whose viscosity values are 1cst and 32cst, so that they could offer much higher damping force to control the vibration and consume the heat and energy causing by vibration. The experiment shows that viscosity of the damping liquid has prominent effect to rotor's vibration, guiding the research to go further on it.

Table 1 Damping situation

Damping situation	No liquid	Water	Engine oil	2.4×10^5cst damping liquid	6.0×10^5cst damping liquid	15×10^5cst damping liquid
Number	1	2	3	4	5	6

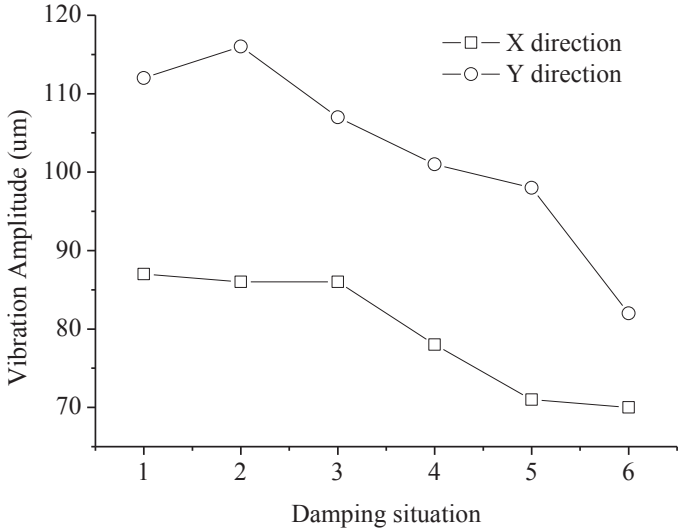

Fig. 4 Comparison of X and Y directions with different damping situations

4.2 Effect of Damping Device in Different Counterweight Conditions on Rotor's Vibration

In order to analyze the phenomenon more clearly, the 15×10^5cst viscosity damping liquid was chosen to be compared with the no liquid situation. To change the counterweight on the disk, several bolts and nuts were fixed at 0 degree and 45 degree phase on the disk which is described in Fig. 5. Each bolt is 3.04g and each nut is 1.04g. The disk is described in Fig. 5. Six different working conditions were setting by vector synthesis method to test the effect of damping technology, as they are listed in table 2. The vibration curves are drawing in Fig. 6.

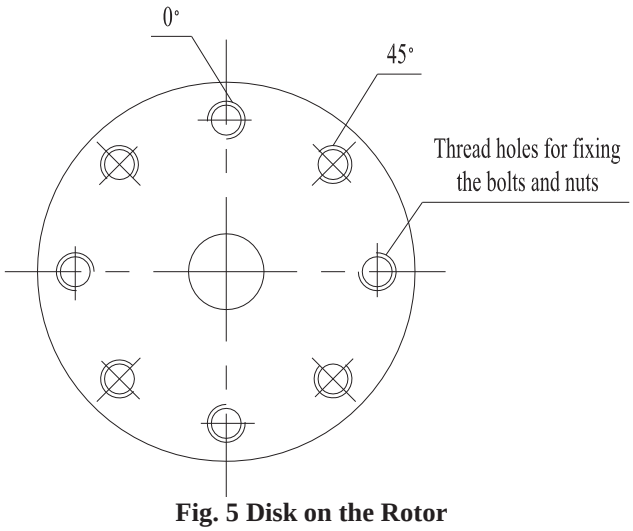

Fig. 5 Disk on the Rotor

Table 2 Six counterweight conditions

Condition Number	C.1	C.2	C.3	C.4	C.5	C.6
Specific Condition	0° fixed one bolt.	0° fixed one bolt and one nut.	0° fixed one bolt and two nuts.	0° fixed one bolt and two nuts, 45° fixed one bolt.	0° fixed one bolt and two nuts, 45° fixed one bolt and one nut.	0° fixed one bolt and two nuts, 45° fixed one bolt and two nuts
Unbalance Value	60.8 g • mm Phase is 0°	81.6 g • mm Phase is 0°	102.4 g • mm Phase is 0°	151.6 g • mm Phase is 16.5°	170.2 g • mm Phase is 19.8°	189.2 g • mm Phase is 22.5°

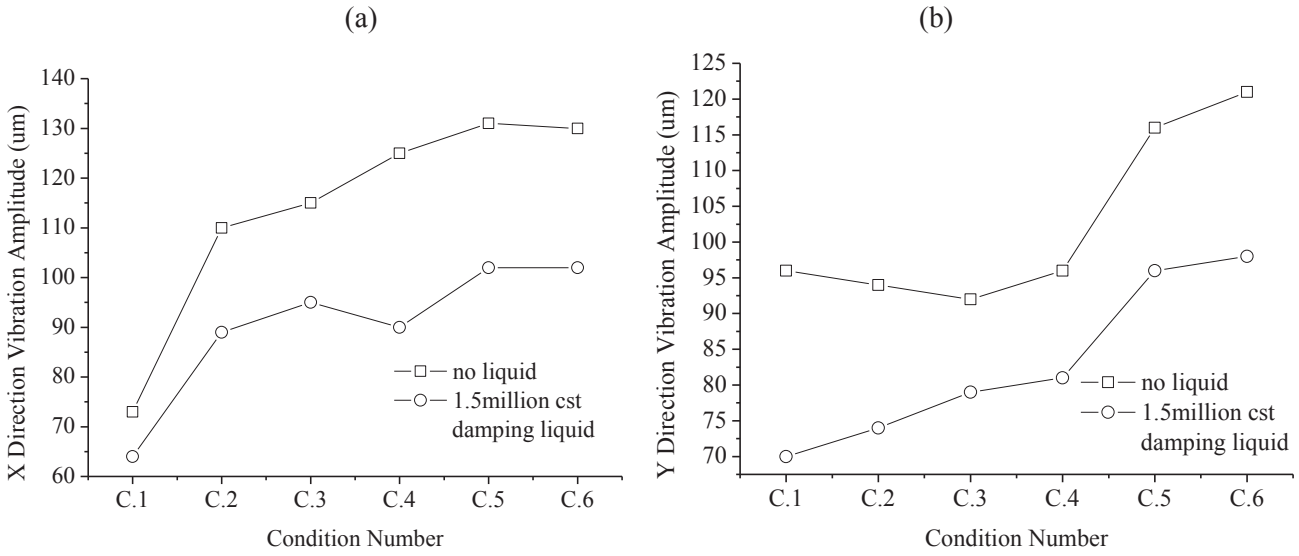

Fig. 6 Vibration results in different working conditions. (a) Vibration on X direction. (b) Vibration on Y direction

Fig. 6 shows that in all six different working conditions, the high viscosity damping fluid could make significant results on rotor's vibration. Especially in condition 4, the vibration amplitude reduced from 125um to 90um in the X direction, and in condition 1, the vibration amplitude reduced from 96um to 70um in the Y direction. The vibration decreased about 28.0% and 27.1% separately. This method is adjustable to various counterweights and different phases mainly because the damping liquid transferred the rotor's kinetic energy into damping liquid's thermal energy. No matter what kind of counterweight is, the rotor generates energy, and the polymeric liquid absorbs it and turns into heat in the liquid, and the heat will dissipate in the outer air. This method concentrates on reducing the vibration energy, avoids complex calculation caused by the unbalance mass, and greatly improves the damper's adaptability to unbalanced working conditions.

5. Conclusions

A recently developed damping device has been applied to an experimental rig which has a rotating rotor on the shaft. The design of the device exploited a particular innovation way to use damping liquid to control rotor's unbalanced vibration. Through changing the different parameters in a series of experiment, the following conclusions are harvested in the end. All the reported findings are supported by experimental evidence collected from the test rig.

(1) By comparing the six vibration results obtained from the different damping liquid respectively, it is demonstrated that the high viscosity ones have the ability to consume the energy causing by rotor and reduce the amplitude of vibration. And higher the viscosity, the reduction is more obvious. In contrast, the low viscosity ones do little on controlling the vibration. In this research, 15×10^5cst viscosity damping liquid decreased the vibration 19.5% and 26.8% in X and Y direction separately.

(2) Based on the first experiment, the high viscosity damping liquid was expected to influence the vibration in different unbalanced situations. Then the authors fixed several bolts and nuts to be the counterweight to simulate the unbalance mass. The experiment of changing different counterweight on the disk demonstrates that the damping device can be utilized to various unbalanced vibration. The high viscosity damping liquid absorbs the energy generated by the vibration and transfers it into heat which could dissipate in the outer air.

From the two experiments before, it is thus concluded that damping device designed in this article has great adaptability compared with the former techniques, and it has prominent meaning for the unbalanced vibration controlling technology field.

Acknowledgment

The authors gratefully acknowledge the financial support provided by Joint Project Special Fund of Education Committee of Beijing and the Ph. D. Programs Foundation of Ministry of Education of China (Item No.: 20110010110009) and National Basic Research Program of China (973 program) (Item No.: 2012CB026000).

References

[1] S. B Xia, G. H Liu, Y. Li and G. F Xu. Rotation Mechanical Automatic Dynamic Balance Review, *China Mechanical Engineering*, Vol. 10, No. 4, pp. 459-462, 1999.

[2] C. B He, Y. J Gu and Z. Q Chen. Coupled Flexural-Torsion Vibration of Rotors with Unbalance Mass, *Proceedings of the CSEE*, Vol. 26, No. 14, pp. 134-139, 2006.

[3] X. X Wang and S. Zeng. The Study of an On-Line Automatic Dynamic Balancing System and Its Dynamic Balancing Method When Used on a Flexible Rotor, *Journal of engineering for thermal energy and power*, Vol. 18, No. 1, pp. 53-57, 2003.

[4] H. B Ouyang, Y. B Zhao and X. X Wang. Experiments and Applications of Online Auto-Balancing With Electromagnetic Auto- Balancing Head, *Journal of Vibration and Shock*, Vol. 21, No. 1, pp. 24-26, 2002.

[5] N. Xia, G. Meng. Retrospect and Prospect to The Research On Squeeze Film Damper Bearing(Sfdb) and on Dynamic Characteristics of Rotating Machinery Rotor—Sfdb System, *Journal of Mechanical Strength*, Vol. 24, No. 2, pp. 216-224, 2002.

[6] M. Zarzour and J. Vance. Experimental Evaluation of a Metal Mesh Bearing Damper, *Journal of Engineering for Gas Turbines and Power*, Vol. 122, No. 21, pp. 326-329, 2000.

[7] M. Zhou, W. D Ni, W. H Yu. Investigation on Adjusting Frequency and Relieving Vibration of a Gas Turbine by Flexible Support and PSFD, *Journal of Tsinghua University (Science and Technology)*, Vol. 39, No. 3, pp. 34-36, 1999.

[8] R. X Huang, A. Q Li and Z. Q Zhang. TMD Vibration Control of Beijing Olympic Center Broadcast Tower under Fluctuating wind Load, *Journal of Southeast University (Natural Science Edition)*, Vol. 39, No. 3, pp. 519-524, 2009.

[9] J. Ren, J. Teng and L. P Ye. Research on Vibration Control of Hybrid Mass Damper for Diwang Tower under Wind Loading, *Earthquake engineering and Engineering vibration*, Vol. 23, No. 6, pp. 187-193, 2003.

[10] M. Wang and P. Gu. Damping Suppression of Vibration for Half-Through Steel Truss Bridges Using TMD, *Journal of Shijiazhuang Railway Institute*, Vol. 19, No. 1, pp. 14-17, 2006.

[11] F. T Tang, L. D He, Y. Jiang and W. Wu. Research of Vibration Occurred in Piping Connected with Centrifugal and Reciprocating Compressor and Damping Technology, *Process Equipment & Piping*, Vol. 46, No. 4, pp. 33-35, 2009.

[12] Y. Jiang, L.D He and W. Wu. Research on Damping Technology in Air Cooler Concentrated Pipe of Propane Tower, *Petrochemical Equipment Technology*, Vol. 32, No. 2, pp. 19-24, 2011.

International Journal of Comprehensive Engineering
Part A, 2(1), 45-51, 2013
Doi: 10.14270/IJCE2013.2.1.a45
Regular paper

ISSN 2186-2680
e-ISSN 2186-2656
www.iace-journal.org

Research on Fluctuating Forces Occurred in Components of Reciprocating Hydrogen Compressors

Yoshifumi Mori [1, 3 #], Takehisa Aoki [1], Katsuhide Fujita [2], and Takashi Saito [1]

[1] Systems Design and Engineering, Graduate School of Science and Engineering, Yamaguchi University, 2-16-1, Tokiwadai, Ube- City, Yamaguchi, 755-8611, Japan
[2] Ube National College of Technology
[3] Tokuyama Factory, Tokuyama Corporation, 1-1, Mikagechou, Shunan-City, Yamaguchi, 745-8648, Japan
[#] Corresponding author:yoshifumi-mori@tokuyama.co.jp ; Tel.: +81-834-34-2221; Fax: +81-834-33-3585

Abstract: Reciprocating compressors have much repetition of maintenance as compared with other compressors and long-term continuous operation is desired. In practice, Breakdown troubles have occurred in the connecting parts during operation. Thus, it is important to understand the effects of the rigidity of the connecting parts on the dynamic behavior in reciprocating compressors. To this end, the present study treated the multi-body dynamics of the crankshaft-piston system using an analytical model with variable spring constants at the connecting parts. The results show that the sliding crosshead and piston rod could be a great factor when the spring constant of the connecting parts was changed in analysis of the multi-body dynamics [1].

Keywords: Multi Body Dynamics, Reciprocating Compressor, Numerical Simulation, Piston-crank Mechanism.

Received: May 31,2012 / Accepted: Nov. 6,2012 / Published: Apr. 8,2013

1. Introduction

Reciprocating compressors are widely used, particularly in petroleum refining and petrochemical processing, efficiently to compress low-molecular-weight gases such as hydrogen [2], because, they have very high compression ratio. However, in contrast to ordinary rotating machinery, which is prone mainly to rotating unbalance, misalignment, and contacting, stress in reciprocating compressors is developed mainly due to changes in load and the inertia of the piston. Thus, it is necessary to investigate the dynamic characteristics at each flexible connecting part between components to elucidate the possible failure mechanisms. However, it is difficult to measure dynamic forces experimentally in an operating machine, where the casing obstructs easy access and each moving part experiences rapid changes in acceleration. Furthermore, the influence on machine operation of damage stemming from the dynamic behavior of moving parts has not been elucidated yet.

This study explored the influence of the rigidity of the connecting parts on the dynamic behavior using a rigid body model comprising the crankshaft, connecting rod, crosshead, piston rod, and cylinder, with elastic springs between them to account for flexibility, as shown in Fig. 1. In addition, the model was validated by comparison with experimental measurements of casing acceleration for an actual compressor operating at same speeds.

2. Multi-body dynamics analysis

2.1 Proposed model

Here we assume that the crankshaft rotates at a constant speed and this rotation is converted into reciprocation of the crosshead through the connecting rod, which can move in the in-plane directions (i.e., horizontally and vertically) and can rotate. The other elements can mainly move horizontally, although the crosshead is assumed to be supported with springs vertically on both sides. The piston rod is allowed to be in-plane motion and supported with the springs at an interim. Furthermore, each connecting part is provided

horizontal and vertical springs corresponding to the allowable motion. From this, we obtain a system with a total of nine degrees of freedom.

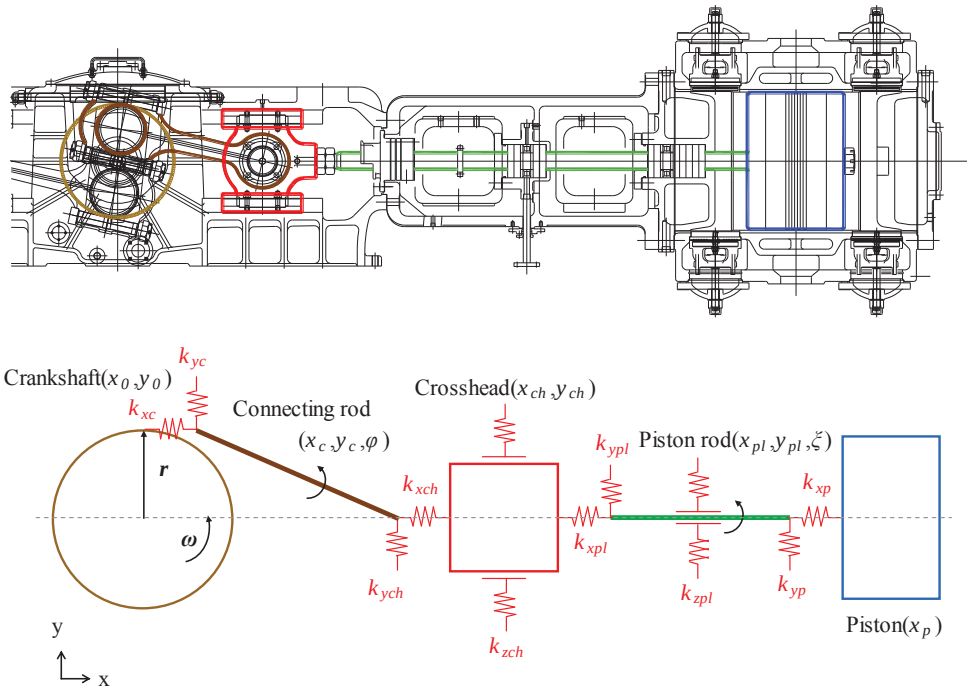

Fig. 1 Simulation model

2.2 Equations of motions

We employ a Cartesian coordinate system with its origin at the rotational axis of the crankshaft, as shown in Fig. 1. The horizontal and vertical directions correspond to coordinates of x and y axes, respectively. The position of the crankshaft (x_0, y_0) can be denoted as,

$$x_0 = r\sin\omega t \quad , \quad y_0 = r\cos\omega t \quad , \tag{1}$$

where ω is the constant angular velocity and r is the rotating radius. From this, the equations of motion for the crosshead (x_{ch}, y_{ch}) are

$$\left.\begin{aligned} m_{ch}\ddot{x}_{ch} &= -k_{xch}\left(x_{ch} - \frac{l_{ch}}{2} - x_c - \frac{l_c}{2}\cos\varphi\right) + k_{xpl}\left(x_{pl} - \frac{l_{pl}}{2}\cos\xi - x_{ch} + \frac{l_{ch}}{2}\right) \quad , \\ m_{ch}\ddot{y}_{ch} &= -k_{ych}\left(y_{ch} - y_c - \frac{l_c}{2}\sin\varphi\right) + k_{ypl}\left(y_{pl} - \frac{l_{pl}}{2}\sin\xi - y_{ch}\right) - k_{zch} * y_{ch} \quad . \end{aligned}\right\} \tag{2}$$

Here, the vertical external forces are yielded by the spring supports. The forces (f_{x2}, f_{y2}) between the connecting rod and crosshead are as

$$f_{x2} = k_{xch}\left(x_{ch} - \frac{l_{ch}}{2} - x_c - \frac{l_c}{2}\cos\varphi\right) \quad , \quad f_{y2} = k_{ych}\left(y_{ch} - y_c - \frac{l_c}{2}\sin\varphi\right) \quad . \tag{3}$$

Thus, the equations of motion for the connecting rod (x_c, y_c) can be written as

$$\left.\begin{aligned} m_c\ddot{x}_c &= -k_{xc}\left(x_c - \frac{l_c}{2}\cos\varphi - x_0\right) + k_{xch}\left(x_{ch} - \frac{l_{ch}}{2} - x_c - \frac{l_c}{2}\cos\varphi\right) \quad , \\ m_c\ddot{y}_c &= -k_{yc}\left(y_c - \frac{l_c}{2}\sin\varphi - y_0\right) + k_{ych}\left(y_{ch} - y_c - \frac{l_c}{2}\sin\varphi\right) \quad , \end{aligned}\right\} \tag{4}$$

$$I_c\ddot{\varphi} = -\frac{l_c}{2}\sin\varphi\cdot f_{x2} + \frac{l_c}{2}\cos\varphi\cdot f_{y2} - \frac{l_c}{2}\sin\varphi\cdot f_{x1} + \frac{l_c}{2}\cos\varphi\cdot f_{y1} \quad .$$

The forces (f_{x1}, f_{y1}) between the connecting rod and crankshaft in the horizontal and vertical directions are

$$f_{x1} = k_{xc}\left(x_c - \frac{l_c}{2}\cos\varphi - x_0\right) \quad , \qquad f_{y1} = k_{yc}\left(y_c - \frac{l_c}{2}\sin\varphi - y_0\right) \quad . \tag{5}$$

The equations of motion of the piston as follows:

$$m_p\ddot{x}_p = -k_{xp}\left(x_p - \frac{l_p}{2}\cos\zeta - x_{pl} - \frac{l_{pl}}{2}\cos\xi\right) = -f_{x4} \quad ,$$

$$m_p\ddot{y}_p = -k_{yp}\left(y_P - \frac{l_p}{2}\sin\zeta - y_{pl} - \frac{l_{pl}}{2}\sin\xi\right) - k_{zbp}\left(y_p - \left(x_p - x_{zbp_{t=0}}\right)\sin\xi\right) - k_{zbpl}\left(y_{pl} + \left(x_{zcp_{t=0}} - x_{pl}\right)\sin\xi\right) \quad . \tag{6}$$

And the equations of motion of the piston rod can be written as

$$\left.\begin{aligned} m_{pl}\ddot{x}_{pl} &= -k_{xpl}\left(x_{pl} - \frac{l_{pl}}{2}\cos\xi - x_{ch}\right) + k_{xp}\left(x_p - x_{pl} - \frac{l_{pl}}{2}\cos\xi\right) \quad , \\ m_{pl}\ddot{y}_{pl} &= -k_{ypl}\left(y_{pl} + \frac{l_{pl}}{2}\sin\xi - y_{ch}\right) + k_{yp}\left(0 - y_{pl} - \frac{l_{pl}}{2}\sin\xi\right) - k_{zpl}\left(y_{pl} - \left\{x_{pl} - x_{pl}(0)\right\}\cdot\sin\xi\right) \quad , \\ I_{pl}\ddot{\xi} &= -\frac{l_{pl}}{2}\sin\xi\cdot f_{x4} + \frac{l_{pl}}{2}\cos\xi\cdot f_{y4} - \frac{l_{pl}}{2}\sin\xi\cdot f_{x3} + \frac{l_{pl}}{2}\cos\xi\cdot f_{y3} + \left(x_{pl} - x_{pl}(0)\right)\cdot\cos\xi\cdot f_{y5} \end{aligned}\right\} \tag{7}$$

The forces (f_{x3}, f_{y3}) between the connecting rod and cylinder in the horizontal and vertical directions are

$$f_{x3} = k_{xpl}\left(x_{pl} - \frac{l_{pl}}{2}\cos\xi - x_{ch} + \frac{l_{ch}}{2}\right) \quad , \quad f_{y3} = k_{ypl}\left(y_{pl} + \frac{l_{pl}}{2}\sin\xi - y_{ch}\right) \quad . \tag{8}$$

And the vertical external force is borne by the spring supports as follows:

$$f_{y5} = k_{zpl}\left(y_{pl} - \left\{x_{pl} - x_{pl}(0)\right\}\cdot\sin\xi\right) \quad . \tag{9}$$

2.3 Numerical simulation

For the simulating the mechanism, typical values for the physical parameters of the various components were used, as shown in Table 1. Furthermore, the equivalent spring constant was used for the piston rod: Assuming

Table 1 Parameters

Component	Mass [kg]		Length [m]	
Crankshaft	-	800	-	0.125
Connecting rod	m_c	88	l_c	0.565
Crosshead	m_{ch}	100	-	0.400
Piston rod	m_{pl}	55	l_{pl}	1.589
Piston	m_p	180	-	0.377

	Moment of inertia [$kg*m^2$]	
Connecting rod	I_c	12.3
Piston rod	I_{pl}	22.2

Table 2 Parameters of sliding constants

Spring	$k\times10^8$ [N/m]
k_{xch}	18.0
k_{ych}	18.0
k_{xc}	18.0
k_{yc}	18.0
k_{xpl}	4.3
k_{ypl}	0.025
k_{xp}	4.3
k_{yp}	0.025
k_{zch}	18.0
k_{zpl}	18.0

that the horizontal spring constant between the piston rod and the crosshead is the equivalent one to the longitudinal motion of the piston rod, we use Eq. $k = \frac{EA}{l}$ (10) [3].

The vertical spring constant is determined using the equivalent one to the vertical deflection of a beam. In addition, the supporting spring constants of the sliding parts are assumed to be equal to the maximum value among all. The values of the other spring constants for a rigid piston rod are listed in Table 2. Thus, by changing the spring constant k of the junction between piston rod and crosshead, we can understand the behavior of the piston rod.

2.4 Simulation results

The dynamic motions of each element were calculated by numerical simulation for a constant crankshaft speed of 480 *rpm*. For the piston rod, we plotted the time histories of the vertical acceleration f_{y3}, f_{y4}, and y_{pl} when all springs are rigid bodies (Fig. 2) and when the values of k_{xpl}, k_{zch}, k_{ypl}, and k_{zpl} multiplied by a factor of *1/10 and *10 (Figs. 3, 4, and 5 respectively). We see that the f_{y3} and f_{y4} waveform increased when the spring constant k_{zch} and k_{xpl} of the crosshead was reduced by the same factor. The reason for this increase is the fact that the stress of the piston rod is accompanied by an increase in crosshead motion due to the rigid spring. Under these conditions, crosshead has a high frequency resonant peak, high-order frequency is excited by the stiffness degradation to the side of the crosshead. By contrast, when changing the vertical direction spring constant k_{ypl} between the crosshead and the piston rod is reduced, the acceleration waveform y_{pl} , f_{y3} and f_{y4} decreased. This is because of the change of the force transmittance character between the crosshead and piston rod. In addition, for the piston rod, we have confirmed that the frequency of 320 *Hz* is reduced by change in k_{zch} and k_{ypl} are involved in the rigidity in the vertical direction as shown in the results of frequency analysis ”Table 3”. Then we also confirmed that the frequency of 380 *Hz* is reduced by the change in the horizontal direction of the piston rod. Further, when the crosshead is rigid a peak appears at 1 *kHz*, but not otherwise. This is due to a change in resonance peak of crosshead. When the spring constant in the vertical direction of the piston rod is decreased, it was confirmed that the vertical f_{y3} of force of the crosshead is the maximum. Thus, the crosshead has a high resonance frequency, but the piston rod has a significantly lower frequency. Each peak frequency appears in amplitude modulation by the sidebands of 8 *Hz*.

Table 3 Results of frequency simulation

		Peak frequency [Hz]			
		Crosshead (y_{ch})	Pistion rod (y_{pl})	Pistion rod (f_3)	Pistion rod (f_4)
Rigid body	1	75	318	273	33
	2	240	512	315	83
	3	318	640	512	3316
	4	640	1073	641	512
	5	1073	-	1073	-
k_{zch} *1/10	1	104	104	32	31
	2	252	512	104	72
	3	512	632	252	105
	4	632	1074	632	-
	5	1074	-	1074	-
k_{ypl} *1/10	1	243	512	82	26
	2	317	641	315	-
	3	641	-	641	-
	4	1073	-	1073	-
	5	-	-	-	-
k_{xpl} *1/10	1	32	317	32	32
	2	230	512	226	316
	3	317	1073	318	512
	4	641	-	641	-
	5	1073	-	1074	-

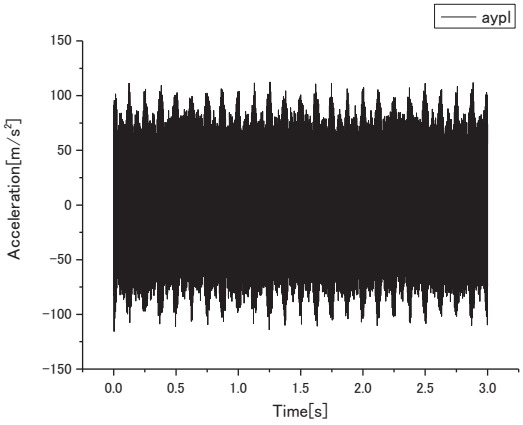

Fig. 2 Simulation results for rigid body

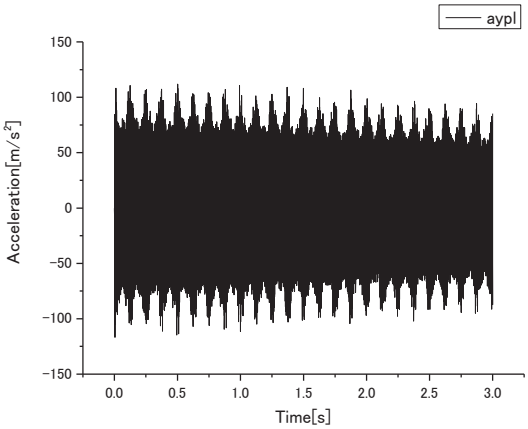

Fig. 3 Simulation results for k_{zch}*1/10

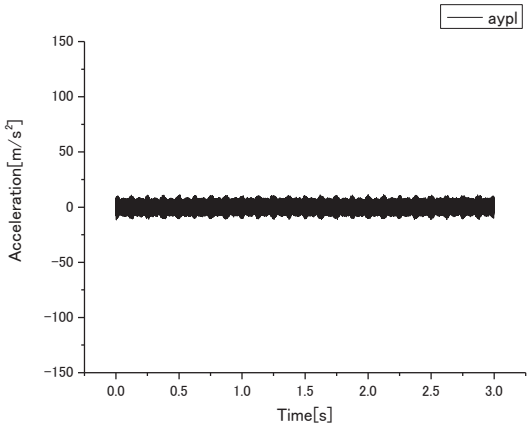

Fig. 5 Simulation results for k_{xpl}*1/10

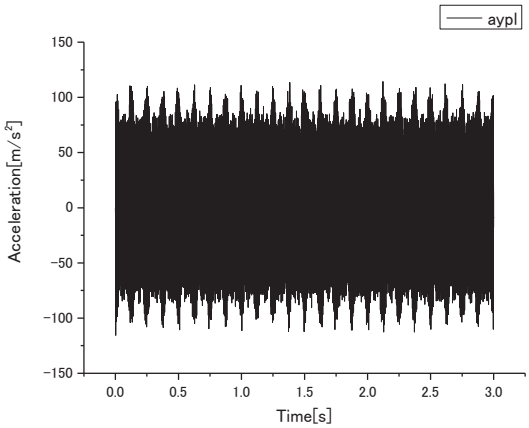

Fig. 4 Simulation results for k_{ypl}*1/10

3. Model validation

3.1 Measurements

We measured the acceleration at the casing for a reciprocating hydrogen compressor with a two double-acting vertically oriented cylinders (Φ540 *mm*) operating at 440 *rpm* (brake shaft power, 488 *kW*) for a maximum piston speed of 3.7 *m/s*, as shown in Fig. 5. We used a three-axis accelerometer for a total of 30 *s* with a sampling period of 15 μs.

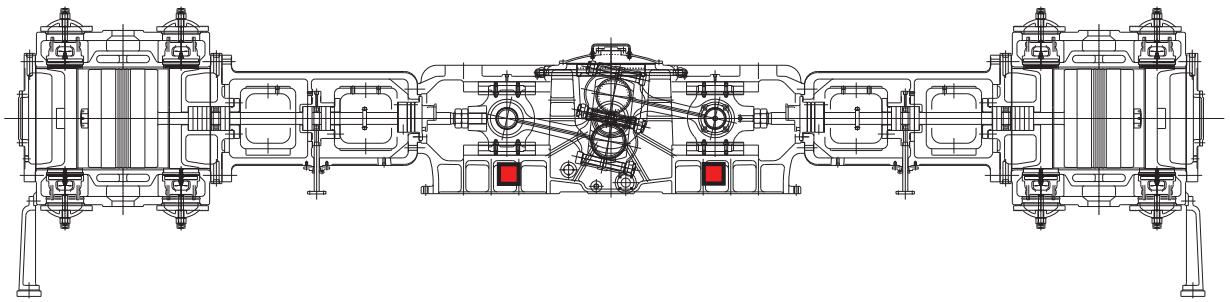

Fig. 5 Structure and measurement position

3.2 Experimental results

Conditions of the analysis conducted the arithmetic averages of 19 measurements, further; this data was arithmetic average of measured data by the machine of 6. As a result, the resonance peak 241 *Hz*, 593 *Hz*, 974 *Hz* and 110 *Hz* were appeared. Furthermore, high-order resonance peak appeared. Compared with the results of numerical simulation, it was confirmed that the resonance peak are the same, as shown in Fig. 6.

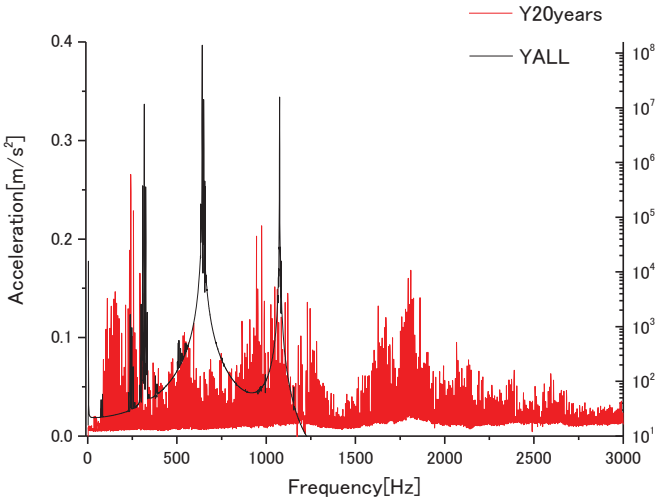

Fig. 6 YALL line is Average frequency along y-axis, Y20years line is All data of simulation results for rigid body

4. Modal analysis

4.1 Modal analysis condition

Using the commercial software of ANSYS, we analyzed the natural frequency and Modes for the piston and crosshead bonded to the piston rod, crosshead and double nut as shown in Fig. 7（3-D）.
The grounds are considered as a constraint in the position of the contact with the piston rod. Then, conditions of this analysis were carried out in the top position of the piston. In addition, the analysis element is "20-NODES SOLID ELEMENT of H METHOD". The extraction method was extracted until the fifth mode by block Lanczos method. The coordinate of the axis direction, the circumferential direction and the radial direction are represented by r, θ and z.

4.2 Modal analysis results

Table 4 shows the natural frequencies corresponding to each mode; we found the stretch mode and bending mode and torsion mode. Then, Table 5 shows the peak list of experimental results. From the results of experimental, the maximum peak appear at 241 *Hz*. This is considered the second bending mode from the results of modal analysis. In addition, we have confirmed that the peak frequency of First and Third bending mode have appeared. Therefore, we have confirmed that the bending mode of the piston rod has appeared in the experimental results.

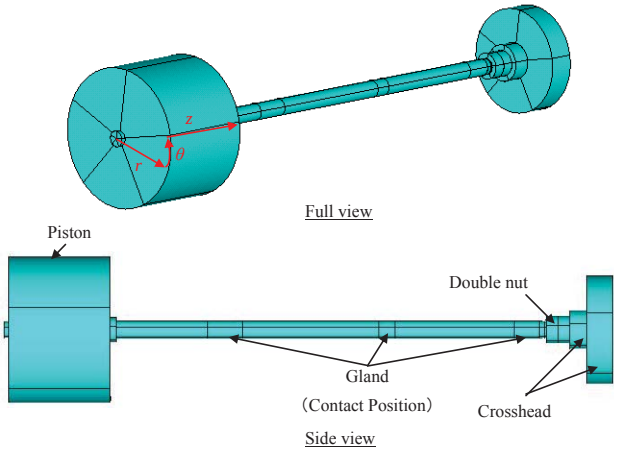

Fig. 7 Crosshead-Piston Analysis model (20-NODES SOLID ELEMENT of H METHOD)

Table 4 Results of modal analysis

Mode	Natural frequency [Hz]	Form of the mode
1	37	Torsional mode
2	105	First bending mode
3	288	Second bending mode
4	367	Stretch mode
5	559	Third bending mode

Table 5 Peak list of experimental results

No	Frequency [Hz]	Acceleration [m/s^2]
1	110	0.14
2	241	0.27
3	593	0.11
4	974	0.22

5. Conclusions

In this paper, we have implemented the analysis of the dynamical characteristic using dynamic model for the influence of the rigidity of the connection parts on the dynamic behavior of reciprocating compressors. In both the experimental and simulation results, we have confirmed that the resonance peaks are same. Thus, we were able to build a dynamic model that is effective to understand the physical phenomena inside.

(1) In the state of a rigid body, high-order frequency has been induced toward the crosshead side.
(2) Reduction in the vertical stiffness of the crosshead makes the frequency of 104 *Hz* appeared and the force of the connecting parts of the piston rod is increased.
(3) The force for the piston rod side of the connecting part of crosshead is largest, and the force has been increased or decreased by changes in the stiffness of the connecting part.

References

[1] Mori Y., Aoki T., Fujita K. and Saito T.. *Dynamic analysis of crosshead–cylinder system in reciprocating compressors*, Proceedings of the 3rd ISDM2011, pp.119-124, 2011.

[2] Naoki AKAGE, "R&D" Kobe Steel Engineering Reports, Vol. 59, No.3, Dec.2009, 55.

[3] Hideo SAITO, Kougyo Kiso Shindogaku and Yokendo, 2004, ISBN4-8425-0137-5 C3053.

International Journal of Comprehensive Engineering
Part B, 2(1), 52-60, 2013
Doi: 10.14270/IJCE2013.2.1.b52
Regular paper

ISSN 2186-2680
e-ISSN 2186-2656
www.iace-journal.org

Design and Realization of an Embedded Bearing Fault Diagnosis System

Rui Zhao, Ruqiang Yan [#] and Yaolei Li

School of Instrument Science and Engineering, Southeast University, Nanjing, 210096, China

[#] Corresponding author: ruqiang@seu.edu.cn; Tel.: +86-135-8405-4760; Fax: +86-25-8379-4158

Abstract: This paper presents an embedded fault diagnosis system designed for bearing defect detection, in which the capability of bearing fault identification has been realized through an analytic wavelet envelope spectrum algorithm. In this design, the ARM9 chip works together with the FPGA chip to serve as the microprocessors and replaces traditionally used PC system. The fault diagnosis algorithm and system control are enabled by the ARM9 chip, while the FPGA chip controls the data sampling and A/D conversion. The software, including the application program and the driving programs, is designed in the embedded Linux system, and implemented using the programming language of C++. The designed system allows for monitoring the bearing defect condition and displaying the diagnosis result on a LCD touch screen. It is envisioned that the designed system can contributes directly to the development of a next generation of portable device for bearing fault diagnosis.

Keywords: Wavelet Envelope, Defect Diagnosis, Embedded System.

Received: May 10,2012 / Accepted: Nov. 6,2012 / Published: Apr. 8,2013

1. Introduction

Since bearings are essential elements in all rotating machine systems, unexpected fault of them often causes rotating machine to work abnormally, affecting productivity as well as maintenance cost. Considering their fault status directly reflects upon machine systems' performance, a reliable and effective bearing fault diagnosis system is highly desired to capture the occurrence of defect at its early stage to ensure continuous, safe operation.

Over the past years, various bearing fault diagnosis systems have been implemented using the PC system [1-4]. The vibration signal is processed by the PC system that runs different fault diagnosis algorithms. The Visual C++ 6.0 is used to write the signal analysis program [1-2]. In [3], it is claimed that the Matlab software is utilized for processing the vibration data from sensors. And with the development of the virtual instrument, its implementation is discussed in [4] as a practicable solution for detecting fault features. Although these systems are automatic and reliable, they are all based on the PC system and require the matched data acquisition card, which implies these PC-based bearing fault diagnosis systems are neither portable nor economical to be used in the actual factory environment.

To overcome these existing limitations, the embedded system has been increasingly investigated [5-10]. Compared to traditional PC-based systems, the major advantage of an embedded system is its flexibility. An embedded system can be dedicated to handle a particular task, which allows our designers to optimize it in order to reduce the size and cost of the product and increase the reliability and performance [11-12]. So the embedded system can be a new choice for the bearing fault diagnosis system. Considering its powerful computing power, a digital signal processor (DSP) is adopted to process the vibration signal instead of the PC [5]. However, it is claimed in [5] that the user-machine interface is based on a PC platform. In [6], the DSP is utilized both for signal processing and the diagnosis system control. DSP and CPLD work together to control the keyboard and the LCD screen instead of a PC. As another embedded microprocessor, the Advanced RISC Machines (ARM) has the advantage of system control. It has sufficient I/O ports and can enlarge peripheral devices easily. Therefore, ARM chips have been adapted as the core microprocessors for many applications in entertainment, manufacturing and biomedical fields [13-18]. With the advancement of the chip technology, some ARM chips, such as ARM9 and ARM11, have improved their computing power, which can be applied in not only system

control, but also signal processing. In this paper, an embedded bearing fault diagnosis scheme is proposed and implemented using two core microprocessors (S3C2440A ARM9 and EP2C8Q208C FPGA). The ARM chip is employed to run the signal processing algorithm and control the system, while the FPGA is used to control the data acquisition. In this design, a QT-based graphical user interface is operated on a LCD touch screen, replacing the traditional combination of a keyboard and a screen, thus reducing the hardware cost. In addition, a wavelet-based enveloping analysis algorithm is implemented as the core bearing fault diagnosis algorithm in the design [19].

The paper is organized as follows: After introducing the system configuration in Section II, the wavelet-based enveloping analysis algorithm, the embedded hardware and software design for the bearing fault diagnosis system are discussed in details in Section III. An experiment conducted on a testing bearing using the embedded bearing fault diagnosis system is performed on Section IV. Finally, some conclusions are drawn in Section V.

2. System configuration

The embedded bearing fault diagnosis system consists of two parts: the ARM control and algorithm module and the FPGA data acquisition module which is shown in Figure 1. As can be seen in Figure 1, acceleration sensors are used to acquire vibration signals from outside surface of the bearing. Then, amplifying circuits are used to amplify these weak electric signals. Subsequently, an A/D converter transforms the amplified charge signals into their digital equivalents to make them suitable for inputting to a FPGA chip, which is used to control the process of data sampling and store these digital data. At last, the digital data from the FPGA chip are sent to an ARM chip where the core fault diagnosing algorithm will run. At the same time, the ARM chip, as the main control core, manages the SDRAM, FLASH and DPRAM storage, displays the final enveloping spectrum result on the LCD touch screen and handles the communication with the FPGA chip through the serial port following the RS-232 communication protocol. The users can operate the whole system and monitor the working status of the bearing on the LCD touch screen.

3. System Design

3.1 The multi-scale enveloping spectrogram

Considering non-stationarity of the bearing vibration signal, the signal processing algorithm, termed multi-scale enveloping spectrogram (MuSEnS), is adopted in the system. As we all know, spectrum analysis of the envelope of a vibration signal has been proved to be more effective in detecting bearing fault than that of the vibration signal itself [20-21], and wavelet transform can provide an effective means (i.e. a time-scale domain analysis) to extracting a weak signal component out of strong noise. Therefore, the MuSEnS algorithm combines the advantage of wavelet transform and envelope specturm analysis to enhance the performance of detecting the bearing fault. In order to achieve effective feature extraction for detecting bearing fault, the complex Morlet wavelet, which has been proved to be an appropriate wavelet function for bearing defect identification [22-23], is used in this study. The complex Morlet wavelet has an explicit expression in the frequency domain:

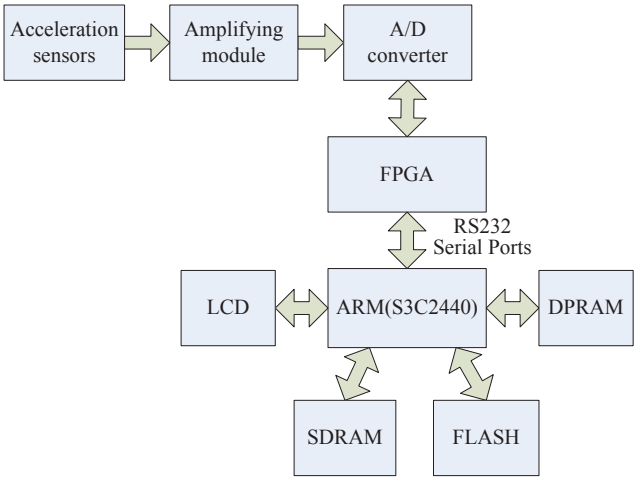

Fig. 1 System architecture of the embedded bearing fault diagnosing system

$$\Psi(f)=\frac{1}{f_b}e^{-\frac{\pi^2(f-f_c)^2}{f_b^2}} \tag{1}$$

where f_b is the bandwidth parameter and f_c is the wavelet center frequency. The computational process of the MuSEnS algorithm is shown in Figure 2. Firstly, the signal $x(t)$ is processed using the Fast Fourier transform. Then, the wavelet coefficients of the signal in the frequency domain is formed by performing the inner product operation between $X(f)$ and $\Psi(f)$. Through an inverse Fast Fourier transform, the wavelet coefficients are converted back into the time domain. The absolute values (i.e. modulus) of the wavelet coefficients are taken to extract the wavelet envelopes. Eventually, the envelope spectrum is obtained by performing the Fast Fourier transform on the wavelet envelope.

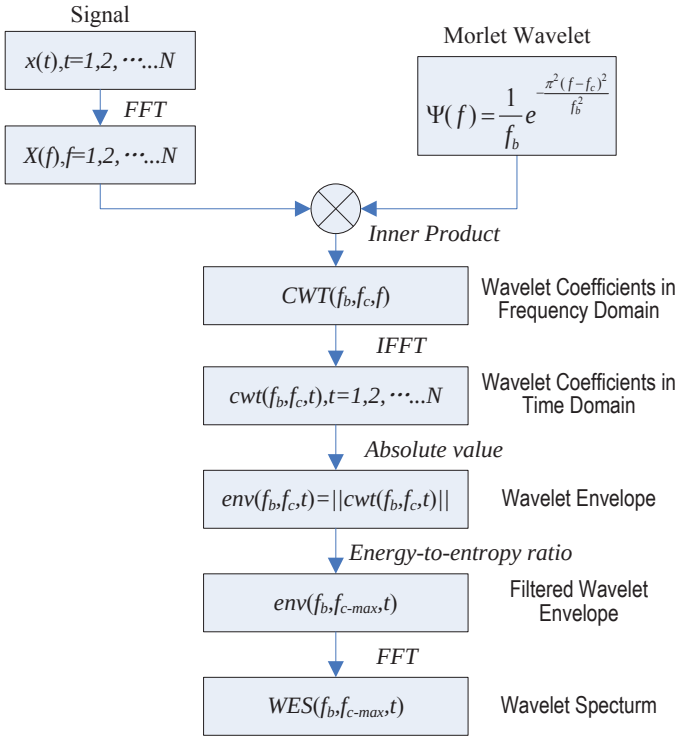

Fig. 2 Procedure for the core fault diagnosing algorithm

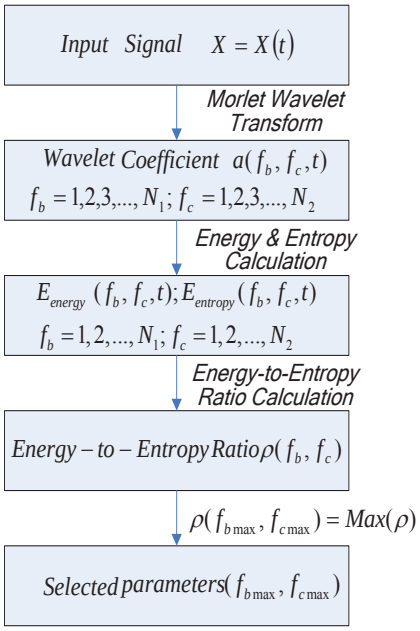

Fig. 3 Illustration of the maximum energy-to-entropy ratio criterion

To ensure effective signal filtering, a scale of the Morlet wavelet needs to be chosen before applying the algorithm to process the vibration signal. A maximum energy-to-entropy ratio criterion is used in this study [24], and the procedure about the criterion is shown in Figure 3. Specifically, the input signal is first decomposed by the Morlet wavelet transform, and a series of wavelet coefficients with different fc are obtained. The corresponding energy and Shannon entropy content for each fc are then calculated to formulate the energy-to-entropy ratio matrix. Then, Fourier transform is performed on the envelope signal at the fc , whose corresponding wavelet coefficients possess the highest energy-to-entropy ratio.

3.2 Embedded System

Normally, the bearing fault diagnosis system can be structured in two categories: the PC-based system and the embedded system. These two different systems are compared in Table 1 in term of the hardware, software and development platform. It can be seen that compared to the PC-based system, the embedded system has smaller size, lower cost and lower power consumption. Although many existing bearing fault diagnosis applications were achieved in the PC system, the industry-oriented performance of the embedded system is proved to be reliable and effective. Therefore, the embedded system is chosen in the design of our system.

Table 1 Comparison between the embedded system and the PC system

	The embedded system	The PC system
CPU	The embedded processor(ARM,DSP)	CPU
Storage devices	The flash chip or EPPROM	The hard-disk
Input devices	The touch screen and keyboard	The mouse and keyboard
Output devices	The LCD screen	The computer monitor
Operating systems	Linux, WinCE, u C/OS-II,Vxwork(need the porting of operating systems)	Windows, Linux(don't need the porting of operating systems)
Drivers	The driver to support each device should be written or ported	The driver to support each device already exists in the operating system
Development platforms	The cross-compilation on a service computer	Developing and debugging on itself

Many ARM microprocessors, including ARM7, ARM9 and ARM11, can be used for signal processing and system control. Considering the high cost of the ARM11, ARM7 and ARM9 are the most general microprocessors in industrial applications. In our design, not only the system control but also the signal processing algorithm should be implemented in the ARM chip. The instruction set of ARM9 has 5 degrees pipeline, while the ARM7 only has 3 degrees pipeline. The difference between the pipelines of the two ARM microprocessors demonstrates the advantage of the ARM9 and is shown in Figure 4. As a result, a S3C2440A ARM9 chip is chosen as the microprocessor of the control and algorithm processing module, while an EP2C8Q208C FPGA chip is used to control the data acquisition. In the design, the serial port has been chosen for data transmission between the FPGA chip and the ARM chip.

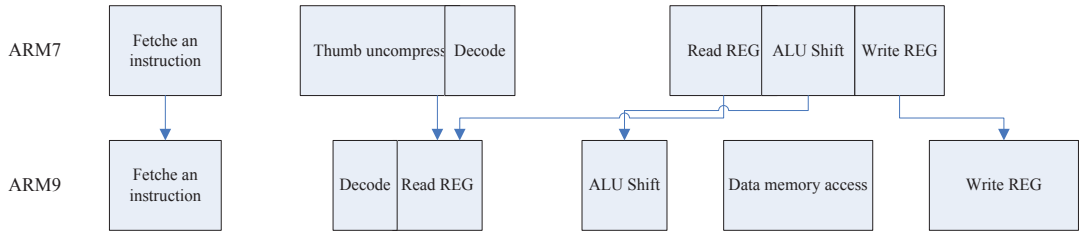

Fig. 4 Illustration of the difference between the pipelines of ARM7 and ARM9

3.3 Software Design

The system software includes two major sections as follows: the ARM program and the FPGA program. The software architecture is shown in Figure 5.

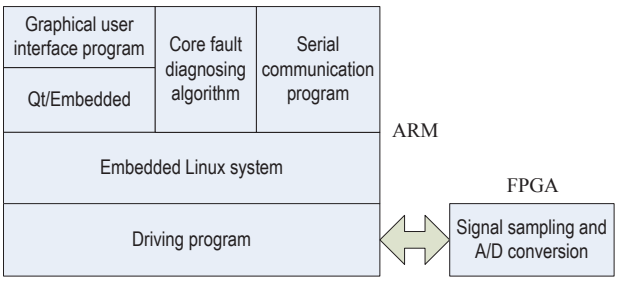

Fig. 5 The software architecture of the whole system

3.3.1 The ARM Application Program

The ARM application program, designed by the information mechanism, is based on the operating system: Linux. Different embedded operating systems, including Vxwork, WinCE, uC/OS-II can be chosen. Since these systems are neither free nor open source, software development on them is not convenient. Due to its low cost and convenience of customization, Linux has been used in many ARM-based systems [17-18]. The advantages of the embedded Linux over other embedded operating systems include license free, a stable kernel, a wide support, and the ability to modify and redistribute the source code. Therefore, we choose the embedded Linux system as the operating system of the ARM chip.

The whole ARM application program can be divided into the application program and the driving programs, which is shown in Figure 6. In the application program coded in C++, three processes: the graphical user interface (GUI) program, the serial communication program and the core fault diagnosing algorithm program are completed, then the multi-process is set up. Furthermore, the driving programs include the serial port driving program, the storage devices driving program and the LCD touch screen driving program, which support the application program to exchange data with the underlying hardware.

Three main graphical user interface development platforms can be used and shown in Table 2. The MicroWindows platform can provide a complete graphical service, but it has many redundant graphical algorithms. Compared to the MiniGUI platform, the Qt/Embedded platform has more complete function modules. For the graphical user interface design of our system, on the Qt/Embedded platform, we can not only use many exiting widgets but also customize our own widgets to construct the main window of the application program. Therefore, the Qt/Embedded platform is chosen to design the GUI of our embedded system. To present a user-friendly human-machine interface, some aspects, including ease of operation, visual appearance, and the demanding of different users, must be taken into account. Figure 7 shows the designed graphical user interface of the embedded bearing fault diagnosis system. The main window shown in Figure 7 allows an operator to adjust input parameters for the core diagnosis algorithm to achieve an accurate bearing fault detection, such as the initial value, the ending value and the steps of the wavelet center frequency f_c , and the sampling time Furthermore, the soft keyboard is displayed in the main windows, which allows the operators for changing the input parameters conveniently. In addition, the machine operator can press the start button to start the serial communication program. When switched to the serial communication program, the bearing vibration data saved in the FPGA core is transmitted to the ARM core through the serial port, following the RS-232 communication protocol. According to the value of the sampling time, the serial communication program switches to the core fault diagnosing algorithm program automatically. The program of the core fault diagnosing algorithm mainly achieves the function of FFT, IFFT and the Morlet wavelet transform. Subsequently, the enveloping spectrum of the processed bearing vibration signal is displayed on the LCD touch screen.

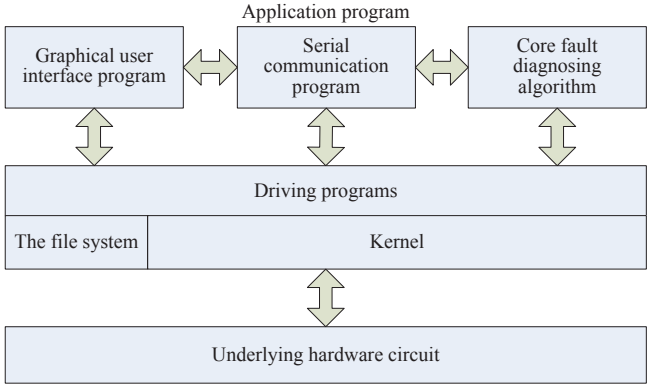

Fig. 6 The relationship between the application and the underlying hardware circuit

Table 2 Comparison among MicroWindows, MinGUI and Qt/Embedded

MicroWindows	1) It provides the most complete graphical service. 2) It is based on the C/S structure. 3）It supports many kinds of external devices to input. 4) It has many redundant graphical algorithms.
MiniGUI	1) It is the compact development platform. 2) It can support the WinCE operating system. 3) It lacks some function modules
Qt/Embedded	1) It is a professional software development kit to design an embedded graphical user interface. 2) It provides many widgets and allows the customization of widgets.

3.3.2 The FPGA Application Program

The operation of data sampling and transmission is controlled by the software codes residing in the FPGA core. The software codes are divided into four modules as follows: ADS7841_module, fifo0, tx_top_ce ontrol_module and tx_module, which are all realized in the Verilog HDL language. These modules fulfill the following tasks: a) The FPGA core controls and drives the ADS7841 A/D chip to convert analog signals to digital format; b) The FPGA core stores the digital data to be processed by the ARM core; c) The FPGA core initializes the serial port; d) The FPGA core not only sends the digital data to the ARM core but also receives the instruction from the ARM core to control the data acquisition. Figure 8 illustrates the code implementation for data acquisition.

Fig. 7 The graphical user interface displayed on the touch LCD screen

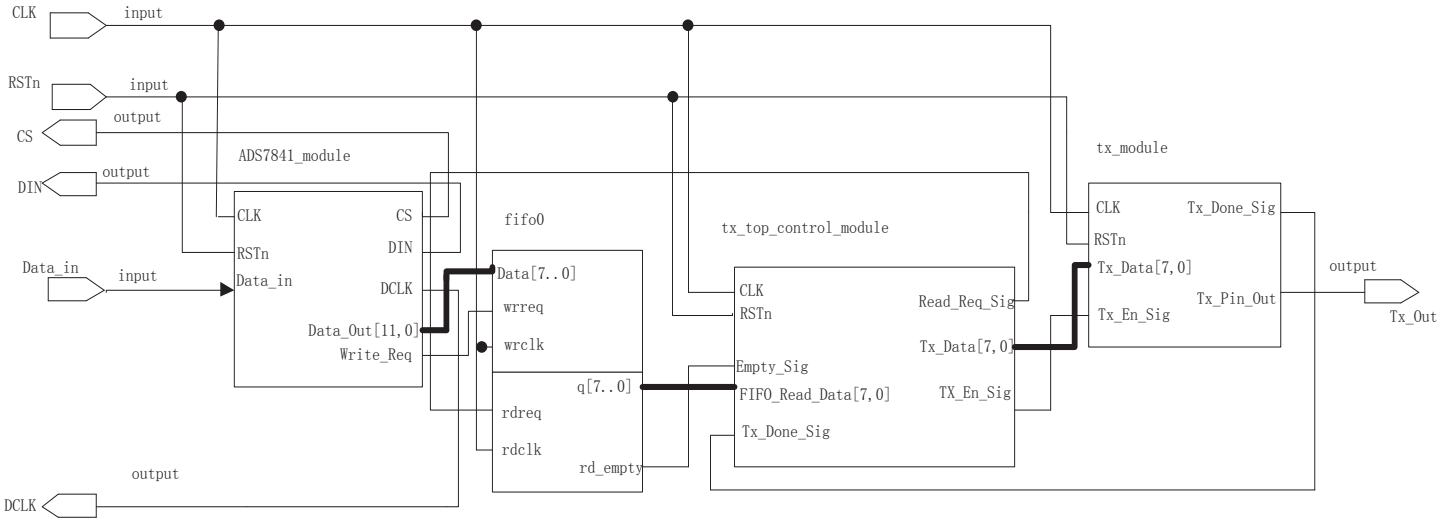

Fig. 8 The code for data sampling and transmission

4. Experimental Verification

The embedded bearing fault diagnosis system was set up as shown in Figure 9. To verify the effectiveness of the designed embedded system for bearing fault diagnosis, an experiment was conducted on a ball bearing with a 0.1 mm diameter hole on its outer raceway. The bearing was run at 300 rev/min, and was connected to the designed diagnosing system. The sampling frequency is 20 KHz and sampling time is 1 second. Based on the geometrical parameters and the rotational speed of the bearing, the bandwidth parameter f_b can be set as 800 Hz. Through the graphical user interface of the system displayed on the LCD touch screen, the initial value, the ending value and the changing step of the Morlet wavelet center frequency f_c changing range were set to 1200 Hz, 9600 Hz and 40 Hz, respectively. After pressing the start button, the bearing vibration signals were continuously acquired, and subsequently processed to indicate the bearing fault statue. The enveloping spectrum of the processed bearing vibration signal was shown on the LCD touch screen. As shown in Figure 10, two major peaks were clearly shown at the 80 and 160 Hz frequency lines. The 80 Hz and 160 Hz components represent the repetitive frequency of the bearing due to the structural defect on the outer raceway and its harmonics. This demonstrated that the designed bearing fault diagnosing system is able to clearly identify the existence of the structural defect for diagnosis purpose.

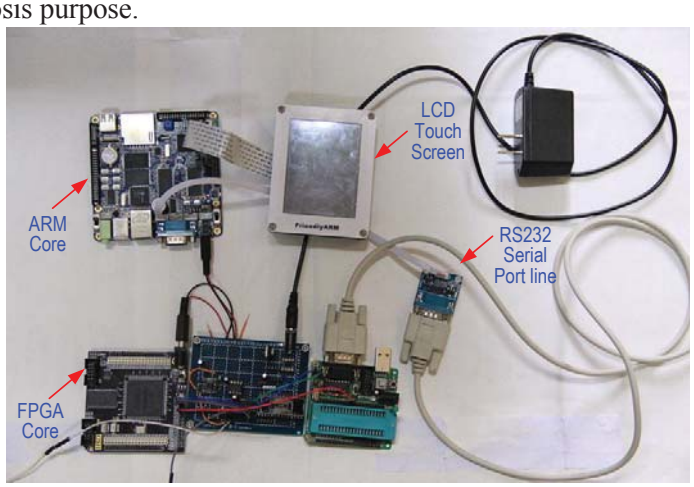

Fig. 9 The embedded bearing fault diagnosing system

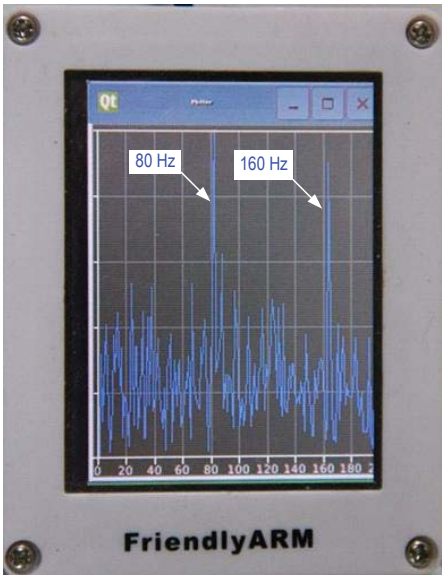

Fig. 10 The embedded bearing fault diagnosing system

5. Conclusion

This paper has introduced design and implementation of an embedded bearing fault diagnosis system. The embedded bearing fault diagnosing system has following advantages: 1. Selection of the embedded system makes the designed system portable with good expansibility and low development cost; 2. Through combining the ARM core with the FPGA core, the operational efficiency of the system is enhanced effectively; 3. The QT-based

graphical user interface of the designed system, combined with the LCD touch screen, enables a user-friendly human-machine interface. Experimental evaluation, conducted on a ball bearing with seeded fault, has demonstrated that the embedded bearing fault diagnosing system has met the design requirements, and is able to detect bearing defects. The designed system presents a new tool that enables effective and reliable diagnosis of the bearing fault.

Acknowledgment

This work has been supported by the National Natural Science Foundation of China (No. 60874022 and No. 51175080)

References

[1] T. X Zhang and X. J Guo. Design and Application of Fault Diagnosis System of Rolling Bearings, *Bearing*, No. 7, pp. 28-30, 2005.

[2] H. L Wu, S. N Zhu, X. F Wan and R. Z Lin. *A New Virtual Instrument System of Rolling Bearing Fault Diagnosis*, Scientific Instrument, 2002.

[3] Tsai Nan-Chyuan, King Yueh-Hsun and Lee Rong-Mao. Fault Diagnosis for Magnetic Bearing Systems, *Mechanical Systems and Signal Processing*, Vol. 23, pp. 1339-1351, 2009.

[4] Changting Wang and Robert X. Gao. A Virtual Instrumentation System for Integrated Bearing Condition Monitoring, *IEEE Transactions on Instrumentation and Measurement,* Vol. 49, No. 2, pp. 325-332, 2000.

[5] Bilal Akin, Seungdeog Choi, Umut Orguner and Hamid A. Toliyat. A Simple Real-Time Fault Signature Monitoring Tool for Motor-Drive-Embedded Fault Diagnosis Systems, *IEEE Transactions on Industrial Electronics*, Vol. 58, No. 5, pp. 1990-2001, May 2001.

[6] Guoqiang Liu. A Portable Vibration Test & Diagnose System on the Rolling Bearing Based On TMS320VC5402, *Journal of Vibration and Shock*, Vol. 25, No.3, 2006.

[7] L. Wang, Q. K Han and M. Zhang. An Embedded Intelligent Monitoring System for Rotating Machinery Vibrations, *Proceedings of the SPIE-The International Society for Optical Engineering*, Vol. 6794 , pp.67941D-1-6, Dec 2007.

[8] S. Zhang , Y. Yang and Q. K Han . The Application of Fault Diagnosis Algorithm Based on Neural Netwok in Embedded System, *Microcomputer Information*, Vol. 31, pp. 38-39, 2009.

[9] Sang Kwon Lee and Jung Soo Lee. Design of Adaptive Filter for Health Monitoring on a Gearbox, *Key Engineering Materials*, Vol. 321-323, pp. 1237-1240, 2006.

[10] Y. F Xu, J. Z Hu, M. P Jia and B. L Zhong. Research on the Embedded Condition Monitoring and Fault Diagnosis System for The Rotation Machine, *Journal of Southeast University(Natural Science Edition)*, Vol. 6, pp. 34, 2004.

[11] Michael Barr. *Embedded Systems Glossary*, Neutrino Technical Library, 2007.

[12] Heath, Steve, *Embedded systems design*, Elsevier Publishers, 2002.

[13] Sheu Yung-Hoh, Dai Yu-Ping and Fu Duen-Shiang. Embedded USB Homecare Internet System, *Proceedings of the 2010 IEEE Asia Pacific Conference on Circuit and System(APCCAS)*, pp. 442-445, 2010.

[14] Wang Xionggui and Huang Tinglei. Development of Embedded Multiparameter Biomedical Monitoring System, *Proceedings of the First International Symposium on Test Automation & Instrumentation*, Vols 1-3, pp. 1191-1195, 2006.

[15] Pavel Ana Brandus and Buiu Catalin. Development of An Embedded Artificial Vision System for an Autonomous Robot, *International Journal of Innovative Computing Information and Control*, Vol. 7, No. 2, pp. 745-762, 2011.

[16] J. J Zhou and J. H Zhou . Research on Embedded Digital Image Recognition System Based on ARM-DSP, *2009 2ND IEEE International Conference on Computer Science and Information Technology*, Vol.1, pp.524-527, 2009.

[17] J. Wan, Y. Yuan and T. Y Wang . Research and Development of A Portable Data Acquisition and Analysis System Based on ARM and DSP, *2ND IEEE International Conference on Advanced Computer Control (ICACC 2010)*, Vol.4, pp. 32-36, 2010.

[18] L. Z Jiang, J. H Sun and Y. R Xiang. 2008 International Workshop on Education Technologu and Training and 2008 International Workshop on Geoscience and Remote Sensing, Vol. 2, pp. 813-816, 2009.

[19] R. Gao and R. Yan. Multi-scale Enveloping Spectrogram For Vibration Analysis in Bearing Defect Diagnosis. *Tribology Intetnational*, Vol. 42, No. 2, pp. 293-302, 2009.

[20] Peter W. Tse, Y. H. Peng and Richard Yam. Wavelet Analysis and Envelope Detection For Rolling Element Bearing Fault Diagnosis-Their Effectiveness and Flexibilities, *Journal of Sound and vibration*, Vol. 123, pp. 303-310, 2001.

[21] Ho. D and Randall RB. Optimization of Bearing Diagnostic Techniques Using Simulated and Actual Bearing Fault Signals. *Mechanical System and Signal Process*, Vol. 14, No. 5, pp. 763-788, 2000.

[22] Shyh-Jier Huang and Cheng-Tao Hsieh. High-Impedance Fault Detection Utilizing A Morlet Wavelet Transform Approach, *IEEE Transactions on Power Delivery*, Vol. 14, No. 4, pp. 1401-1410, October 1999.

[23] J. Lin and M. J. Zuo. Gearbox Fault Diagnosis Using Adaptive Wavelet Filter, Mechanical Systems and Signal Processing, Vol. 17, No. 6, pp. 1259-1269.

[24] R. Gao and R. Yan. Harmonic Wavelet-based Data Filtering For Enhanced Machine Defect Identification, *Journal of Sound and Vibration*, pp. 3203-3217, 2010.

International Journal of Comprehensive Engineering
Part B, 2(1), 61-66, 2013
Doi: 10.14270/IJCE2013.2.1.b61
Regular paper

ISSN 2186-2680
e-ISSN 2186-2656
www.iace-journal.org

Intelligence Diagnosis Method for Structure Faultof Rotating Machinery

Jia Pan[1], Huaqing Wang[1, #], JianfengYang[1, #],Wenbin Liu[1] and Peng Chen[2]

[1]School of Mechanical & Electrical Engineering,BeijingUniversity of Chemical Technology, Beijing, 100029, China
[2]Graduate School of Bioresources, Mie University, Tsu, 514-8507 Mie, Japan

[#] Corresponding author: wanghq_buct@hotmail.com; yjf01@263.net. Tel.: +86-10-64443037;

Abstract: Rotating machineryis wildly used in industrial production. The fault diagnosis technology has played a very important role for quality and life of machines. This paper presents an intelligent diagnosis method for structure fault of rotating machinery using the principal component analysis and the BP neural network to detect faults and distinguish fault types. In this paper, the principal component analysis is used to reduce details of time-domain symptom parameters for the training of the BP neural network. The BP neural network, which used for condition diagnosis of roller bearing, can obtain good convergence using the symptom parameters acquired by the principal component analysis when learning, and can automatically distinguish fault types when diagnosing. Practical examples are provided to verify the efficiency of the proposed method.

Keywords: Rotating Machinery, Fault Diagnosis, Rrincipal Component Analysis, BP Neural Network.

Received:May 5,2012 /Accepted: Nov. 6,2012 / Published: Apr. 8,2013

1. Introduction

Rotating machinery is widely used as kind of mechanical equipment in industrial sector which is generally applied to the machinery such as aero engine, gas turbines. This kind of equipment will produce good economic benefit when operated under safe, stable long cycle and full load condition. However, due to the limitation of working conditions and the service life, it usually appears all sorts of different fault. It even leads to serious accident, significant economic loss and endanger personal safety sometimes. Therefore, it has become the security problem to be solved that how to monitor and analyses rotor system timely and accurate, as well as forecast the fault occurred as early as possible.

In the condition diagnosis of rotating machinery, the utilization of vibration signals is effective in the detection of faults and discrimination of fault type, because signals carry dynamic information about the machine state. Condition diagnosis depends largely on the feature analysis of vibration signals [1-4].However, feature extraction for fault diagnosis is difficult because the vibration signals measured at any point of the machine often contain strong noise. Furthermore, diagnostic knowledge is ambiguous because definite relationships between the symptoms and the fault types can not be easily identified [5, 6]. Therefore, there is a need for a reliable, fast automated diagnosis method. Neural networks (NN) have potential applications in auto-mated detection and diagnosis of machine failures [7]. However, NN usually will converge slowly, when the training symptom parameters have the same values in different states [8-12]. This paper proposes a method of condition diagnosis structure fault of rotating machinery using the principal component analysis and the BP neural network to detect faults and distinguish fault types to improve the efficiency and accuracy of the fault diagnosis. Practical examples of fault diagnosis for rotor system have verified that the proposed method is effective.

2. Intelligence diagnosis of structure fault of rotating machinery

The traditional diagnosis methods and theory have larger limitations for complex process and fault, abrupt faults and highly automated equipment. Intelligence diagnosis methods especially neural network, which not depended on the control object and mathematical model, have a good advantage of solving these problems.

Otherwise, as too many of the training sample parameters inputted, it will cause the training with slow convergent speed and low identification accuracy when we use neural network alone. Therefore, attribute reduction usually works before using neural network to make pattern recognition in order to improve recognition accuracy and efficiency. This paper proposes the way of the principal component analysis, to reduce details of symptom parameters for the training of the neural network, which process shown as Fig. 1.

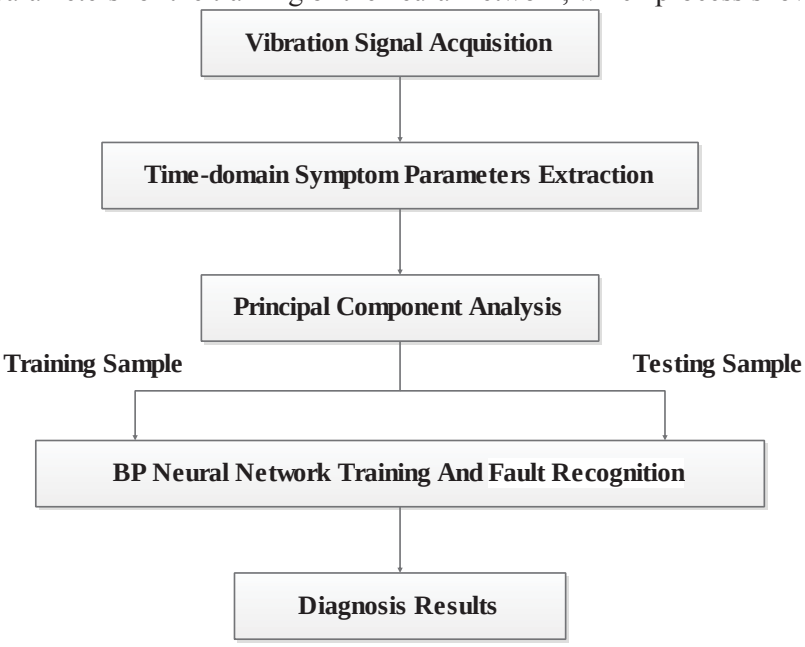

Fig. 1Process of proposed method

2.1 Symptom Parameters Extraction

For automatic diagnosis, symptom parameters are needed that can sensitively distinguish the fault types. A large set of symptom parameters has been defined in the pattern recognition field [13]. Here, the dimensional and non-dimensional in the amplitude domain, commonly used for the fault diagnosis of rotor system, are considered. Using the normalized signals, the 11 symptom parameters in the amplitude domain are calculated as follows, respectively.

$$p_1 = \frac{1}{N}\sum_{i=1}^{N} x_i \text{(M e a n v a} \tag{1}$$

$$p_2 = \sqrt{\frac{1}{N}\sum_{i=1}^{N} x_i^{\,2}} \text{(Root mean square)} \tag{2}$$

$$p_3 = \frac{1}{N-1}\sum_{i=1}^{N}\left(x_i - \bar{x}\right)^2 \text{(Variance)} \tag{3}$$

$$p_4 = \sqrt{\frac{1}{N-1}\sum_{i=1}^{N}\left(x_i - \bar{x}\right)^2} \text{(Standard deviation)} \tag{4}$$

$$p_5 = \max\left(\left|x_i\right|\right) \text{(Peak value)} \tag{5}$$

$$p_6 = \frac{1}{N}\sum_{i=1}^{N}\left|x_i\right| \text{(Absolute mean value)} \tag{6}$$

$$p_7 = \sqrt{\frac{1}{N}\sum_{i=1}^{N} x_i^2} \Big/ \frac{1}{N}\sum_{i=1}^{N}|x_i| \text{(Shape factor)} \tag{7}$$

$$p_8 = \max\left(|x_i|\right) \Big/ \sqrt{\frac{1}{N}\sum_{i=1}^{N} x_i^2} \text{ (Crest factor)} \tag{8}$$

$$p_9 = \max\left(|x_i|\right) \Big/ \frac{1}{N}\sum_{i=1}^{N}|x_i| \text{(Impulse factor)} \tag{9}$$

$$p_{10} = \max\left(|x_i|\right) \Big/ \frac{1}{N}\sum_{i=1}^{N}\sqrt{|x_i|} \text{ (Clearance factor)} \tag{10}$$

$$p_{11} = \frac{1}{N}\sum_{i=1}^{N}\left(\frac{x_i - \bar{x}}{\sigma}\right)^4 \text{ (Kurtosis value)} \tag{11}$$

2.2 Principal Component Analysis (PCA)

Principal component analysis (PCA) is a mathematical procedure that uses an orthogonal transformation to convert a set of observations of possibly correlated variables into a set of values of linearly uncorrelated variables called principal components [14]. The number of principal components is less than or equal to the number of original variables. This transformation is defined in such a way that the first principal component has the largest possible variance, and each succeeding component in turn has the highest variance possible under the constraint that it be orthogonal to the preceding components. Principal components are guaranteed to be independent only if the data set is jointly normally distributed. PCA is sensitive to the relative scaling of the original variables. PCA is mathematically defined as an orthogonal linear transformation that transforms the data to a new coordinate system such that the greatest variance by any projection of the data comes to lie on the first coordinate (called the first principal component), the second greatest variance on the second coordinate, and so on.

2.3 BP Neural Network (BPNN)

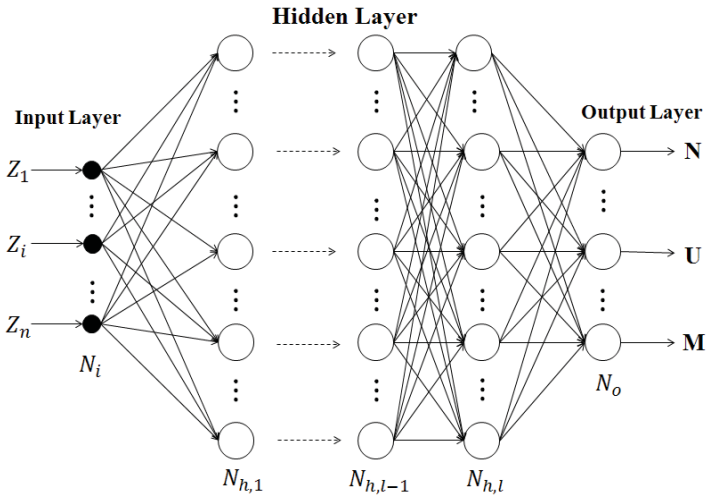

Fig. 2 The construction of BPNN

BP neural network is a multilayer feed forward neural network model. The BP neural network is composedof the input layer, output layer and one or more hidden layer. In theory, BP network with three layers can complete the classification of arbitrary complexity [15]. BP algorithm is a kind of training algorithm with teacher which the learning process including the forward calculation in network internal and error back propagation. In forward calculation, a characteristic vector of training samples is inputted to neural network and gets a real output after forward spread calculation of neural network. Then it will compare this output with the expected

sample output. If there is a deviation, it will turn to back propagation process and return the deviation from the original contact pathways. It will reduce the error through adjusting the contact values of each layer neurons and turn to positive propagation process again. This process will not stop until the error less than or equal to the allowable value. The construction of normal BP neural network is shown as Fig. 2.

3. Experimental Verification

Fig. 3 shows the rotor test rig for diagnosis. Foursensorsare used to measure vibration signals for the diagnosis. The vibration signals are measured at a rotational speed of 600 rpm (10Hz). The sampling frequency is 1 KHz, and the sampling time is 40s or 400 cycles.

The experiments collected vibration signals in three conditions which are normal (N), unbalance (U) and misalignment (M) fault. After collecting, the time-domain data are divided into 20 parts each containing 2,000 (20 cycles) samples to calculate the symptom parameters. Then the symptom parameters of each part are calculated respectively. Finally, the original characteristic matrixes of three different conditions are divided into 2 groups averagely and making the data of first and second groups together respectively form the sample and test data. The first step of PCA is normalizing the original features data. The partial sample and test data after standardization process are shown in Table 1.

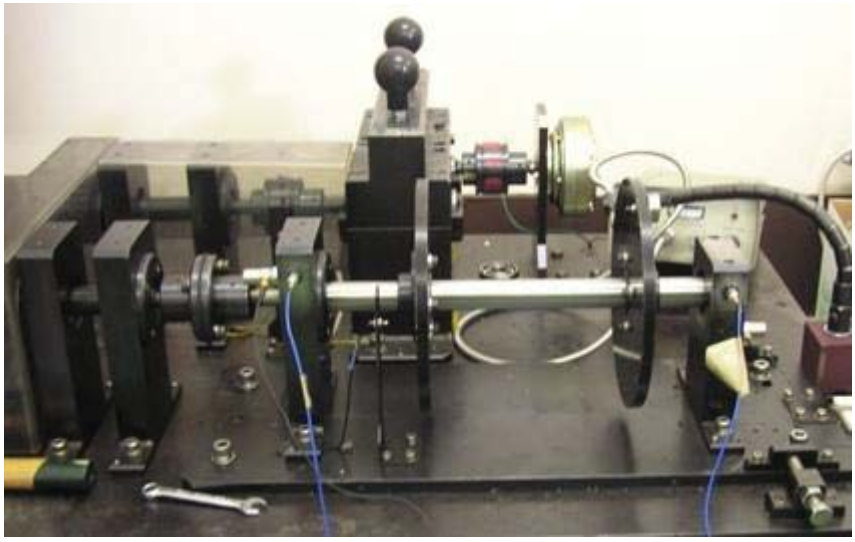

Fig. 3Therotortest rig for diagnosis

Table 1 Data after standardization process

	Sample Data					Test Data				
	1	2	…	29	30	1	2	…	29	30
Mean	0.552	0.279	…	0.350	-0.298	1.703	-2.368	…	-0.610	-0.817
RMS	0.906	0.876	…	-1.389	-1.367	0.997	0.919	…	-1.358	-1.339
Var.	1.011	0.960	…	-1.331	-1.325	1.172	1.034	…	-1.322	-1.316
…	…	…	…	…	…	…	…	…	…	…
CF	-0.337	-0.413	…	0.345	2.545	-0.276	-0.414	…	0.431	4.116
KV	-0.334	-0.399	…	0.365	2.551	-0.279	-0.414	…	0.459	4.111

Table 2Data after PCA process

	Sample Data					Test Data				
	Z1	Z2	…	Z6	Z7	Z1	Z2	…	Z6	Z7
1	-4.101	6.121	…	-0.825	-0.465	-4.160	6.271	…	-0.895	-0.474
2	-3.951	5.884	…	-0.793	-0.465	-3.936	5.900	…	-0.762	-0.458
…	…	…	…	…	…	…	…	…	…	…
29	-6.215	7.370	…	-1.975	-0.407	-6.490	7.726	…	-1.935	-0.416
30	-11.17	13.44	…	-4.118	-0.603	-15.36	18.66	…	-4.702	-0.716

After getting the standardization characteristic matrix, the second step is making eigenvalue decomposition to the relevant matrix of it, in order to get the projection matrix which namely the transformation matrix. Then we choose the front 7 principal component as the transformation matrix based on accumulative contribution rate (99.99%). At last, we multiply the original features matrix with the transformation matrix to get the

characteristic matrix after reduction, which are named as Z1 to Z7. The partial sample and test data after PCA process are shown in Table 2.

In this paper, the numbers of the input layer, hidden layer and output layer for the BP neural network are 7, 10 and 3 based on the actual situation. When setting precision as 0.015, training accuracy reaches the requirements precision at 13841 which process shown in Fig. 4(a).Moreover, training accuracy reaches the requirements precision at 15716using BPNN without reduction which process shown in Fig.4(b). Table 3 shows the partial diagnosis results for each state which the recognition rate is 100%. According to the test results, the probability grades output by the BPNN after PCA process show the correct judgment in each state. On the other hand, the recognition rate is only about 83.33% of BPNN without reduction. Therefore, the BPNN can precisely distinguish the type ofrotorsystem with structure fault, more efficiency and accuracy on the basis of the symptom parameters of vibration signal after PCA process.

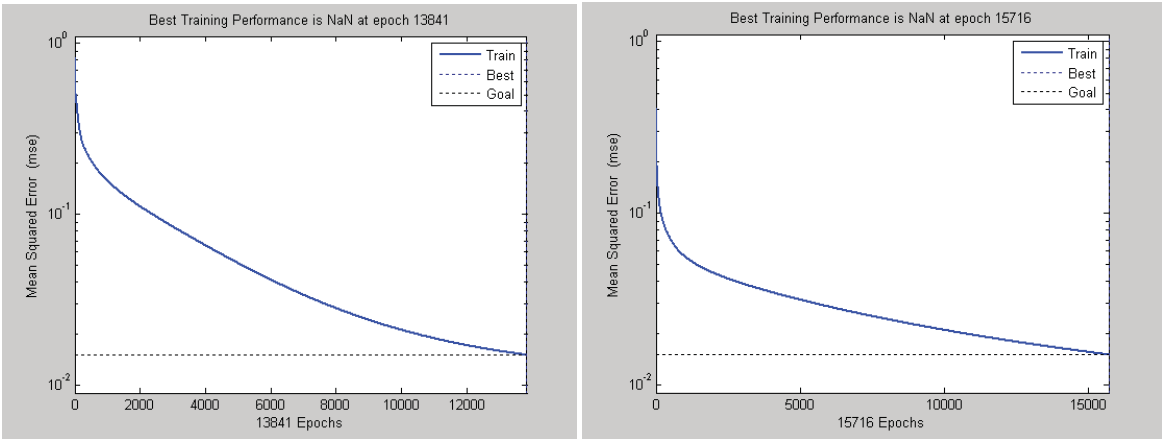

(a) (b)

Fig. 4 Training process of BPNN

Table 3 Verification results

	Possibility grade in each state outputted by BPNN			State judgment
	N	U	M	
1	0.7418	0.2108	-0.0284	Normal
…	…	…	…	…
11	0.2915	0.8100	-0.0065	Unbalance
…	…	…	…	…
21	-0.0187	0.1179	1.5528	Misalignment
…	…	…	…	…
30	0.7060	-1.0041	1.8032	Misalignment

4. Conclusion

In order to effectively diagnose faults and discriminate fault types for rotating machineryat early stages, this paper proposes an intelligent diagnosis method for structure fault of rotating machineryusing features of vibration signals. The diagnosis approach is constructed on the basis of the principal component analysis and the BPNN. The diagnosis knowledge used for BPNN learning can be acquired by the principal component analysis. The BPNN can faster converge when learning, and when diagnosing canautomatically distinguish fault types with higher accuracy. This method is suitable for different type of rotating machinery and has been successfully applied to the condition diagnosis of a rotor test rig.

Acknowledgements

This project is supported by National Program on Key Basic Research Project (Grant No. 2012CB026000),National Natural Science Foundation of China (Grant No.51075023, 51135001)and National Key Technologies R&D Program (Grant No. 2011BAK06B02), and Fundamental Research Funds for the Central Universities (Grant No. ZZ1124)and SRF for ROCS, SEM.

References

[1] J. Lin and L.S Qu. Feature Extraction Based on Morlet Wavelet and Itsapplication for Mechanical Fault Diagnosis, *Journal of Sound and Vibration*, Vol. 234, No. 1, pp. 135-148, 2000.

[2] B. Liu and S. F Ling. On the Selection of Informative Wavelets for Machinery Diagnosis, *Mechanical Systems and Signal Processing*, Vol. 13, No. 1, pp. 145-162, 1999.

[3] MatuyamaH. Diagnosis Algorithm, *Journal of JSPE*, Vol. 75, No. 3, pp. 35-37, 1991.

[4] H. Q Wang and P. Chen. Sequential Condition Diagnosis for Centrifugalpump System Using Fuzzy Neural Network, *Neural InformationProcessing-Letters and Reviews*, Vol. 11, No. 3, pp. 41-50, 2007.

[5] H. C Pusey. Machinery Condition Monitoring, *Journal of Sound andVibration*, Vol. 34, No. 5, pp. 6-7, 2000.

[6] T. Mitoma, H. Q Wang and P. Chen. Fault Diagnosis and Condition Surveillance for Plant Rotating Machinery Using Partially-linearized Neural Network,*Computers & Industrial Engineering,*Vol.55, No. 4, pp. 783-794, 2008.

[7] Samanta B and K. R Al-Balushi. Artificial Neural Network Based Fault Diagnostics of Rolling Element Bearings Using Time-Domain Features, *Mechanical Systems and Signal Processing*, Vol.17, pp. 317-328.

[8] H. Q Wang and P. Chen. Intelligent Diagnosis Method For A Centrifugal Pump Using Features of Vibration Signals, *Neural Computing &Applications*, Vol. 18, No. 4, pp. 397-405,2009.

[9] H. Q Wang and P. Chen. Fault Diagnosis of Centrifugal Pump Usingsymptom Parameters in Frequency Domain, *Agricultural EngineeringInternational: The CIGR E-journal*, Vol.11, pp. 1-14, 2007.

[10] Saxena A and A.Saad. Evolving an Artificial Neural Network Classifierfor Condition Monitoring of Rotating Mechanical Systems, *Applied Soft Computing*, Vol. 7, No. 1, pp. 441-454, 2007.

[11] Samanta B and K. RAl-Balushi. Artificial Neural Network Based Faultdiagnostics of Rolling Elementbearings Using Time-Domain Features, *Mechanical Systems and Signal Processing*, Vol. 17, No. 2, pp. 317-328, 2003.

[12] R. Q Li, J. Chen and X. Wu. Fault Diagnosis of Rotating Machinery Usingknowledge-Based Fuzzy Neural Network, *Applied Mathematics andMechanics*, Vol. 27, No. 1, pp. 99-108,2006.

[13] Fukunaga K. *Introduction to Statistical Pattern Recognition*, Academic Press, London.

[14] Rafael C, Gonzalez and Richard E. Woods. *Digital Image Processing*, Addison Wessley Publishing Company, 1992.

[15] Horn IKK and St inchcombem. Whiteh Multilayer Feed-forward Networks are Universal Approx im ators, *Neural Networks*, Vol.12, No. 5, pp. 359-366, 1989.

International Journal of Comprehensive Engineering
Part C, 2(1), 67-77, 2013
Doi: 10.14270/IJCE2013.2.1.c67
Regular paper

ISSN 2186-2680
e-ISSN 2186-2656
www.iace-journal.org

Numerical Calculation of Stainless Steel Stamping Well Pump Based On Regression Orthogonal Test

Weidong Shi, Chuan Wang [#], Qiaorui Si, Jing Xu and Desheng Zhang

Research Center of Fluid Machinery Engineering and Technology, Jiangsu University, Zhenjiang, 212013, China

[#] Corresponding author: wangchuan198710@126.com; Tel.: 086-13236381128

Abstract: Combined with the hydraulic design, regression orthogonal test and Computational Fluid Dynamics, this research concentrated on improving the efficiency of stamping well pumps. An L_{18}（3^7）orthogonal test was designed with seven geometrical parameters and three levels including impeller outlet slope, blade outlet placed angle, blade inlet placed angle, blade outlet width, impeller blade number, guide vane blade number and guide vane inlet width. 18 programs were designed. Well pumps at rated point in the whole flow field were simulated through the standard model, SIMPLEC algorithm and second-order upwind scheme by Fluent. The influence law of geometrical parameters on efficiency and head were discovered by orthogonal analysis. Specifically, impeller outlet slope, blade outlet placed angle and blade outlet width exert the most significant influence on pump efficiency. 16 impellers were designed under the quadratic regression orthogonal test with these three factors. Through quadratic regression equation the function relationship between efficiency values and three factors was fit. As well as the analysis of the regression equation, the optimal combination of geometric parameters could be found and stainless steel stamping well pump with high efficiency could be designed. The result would be instructive to the optimization of stamping well pump that are designed by the impeller maximum diameter method.

Keywords: Stamping Well Pump, Numerical Calculation, Regression Orthogonal Test, Optimization.

Received: May 16,2012 / Accepted: Nov. 6,2012 / Published: Apr. 8,2013

1. Introduction

Submersible well pump are specially equipped for groundwater extraction in rural areas, factories, mines, water companies, geothermal development and oil fields [1]. Most pumps in the past were manufactured by casting process. Conventional casting pump is made by some complex manufacturing processes such as pattern making and machining. These processes will consume lots of power and material and emit a huge amount of toxic gas. Also in the mass production process of small pump, the dimensional accuracy and surface roughness can not be guaranteed due to the limitation of casting process. Stainless steel stamping well pump is produced by cutting through steel, stamping, drawing, wielding and other advanced technologies. All flow components are made through mechanical molds so that the shape and dimensional accuracy is easy to be guaranteed and the hydraulic performance of pump is stable. Therefore, stainless steel stamping well pump is gradually replacing casting well pump and becomes a mainstream product [2]. However, because of expensive cost of stamping mold, it's very necessary to provide excellent hydraulic mode for stamping well pump.

Currently, orthogonal test method has been widely used in the design of pump. Yuan Shouqi (1997) made an in-depth study for the relation between geometric parameters and performance of pump without overload and gave a set of functional theory and design method by using an $L_9(2^7)$ orthogonal test [3]. Using the orthogonal test design method, Wang Hongliang (2010) made a deep research which described the influence of the main geometric parameters of impeller on the new deep well pump characteristics. The important order of these parameters affecting the index of performance and the optimum orthogonal test were also obtained through the

analysis of range diagrams. Finally the new-type well pump's optimization design was realized [4]. Zhou Ling (2010) researched the guide vane and screened the key factors affecting the performance of guide vane by making an orthogonal test [5]. Therefore, orthogonal test method is a mature method of optimization, which is very suitable for the pump design.

Orthogonal test can use less number of tests to obtain better results, but optimization program obtained by orthogonal test can only be limited to the set level, but not necessarily the optimal solution within the test range. The key parameters of hydraulic components of well pump were analyzed through CFD and orthogonal tests, and the trends of geometric parameters which affected hydraulic performance of pump were found. Three main geometric parameters were selected. The function relationship between pump efficiency and three parameters was fitted by using quadratic regression equation. Through the analysis of the regression equation, the optimal combination of geometric parameters could be found and stainless steel stamping well pump with excellent performance could be designed. Therefore, quadratic regression equation helped to further deepen the basis of orthogonal test [6].

2. Hydraulic design

2.1 Hydraulic design of impeller

This paper selects 100XQJ stamping well pump, and the basic design parameters are as follows: Q=8m^3/h, single-stage head H=4.5m, rotation speed n=2850r/min, so specific speed $n_s = 3.65n\sqrt{Q}/H^{3/4} = 158$.

In view of the structural condition that the outer diameter of well pump is limited by well diameter, Lu Weigang (2006) studied a design method of well pump—the impeller maximal diameter design method, which expands the front cover of impeller to the edge of pump wall and makes the impeller diameter achieve maximum value while well diameter is invariable [7]. The impeller is in coordination with the return guide vane, which can shorten the axial length of well pump to the minimum.

In the design of ordinary pump, the impeller diameter is calculated based on the requirements of pump performance, but the impeller maximal diameter design method only provides rated flow at the maximum efficiency point and won't provide rated single-stage head, which hopes that the single-stage head is as high as possible, thereby reducing the series and costs of well pump. In this case the front cover diameter of impeller is 79.5mm. It is equal to the diameter of the pump spigot. The clearance is guaranteed by tolerance and the outlet of impeller is skewed, which is shown in Fig.1. After determining the front cover diameter of impeller, the other structural parameters of impeller can be designed. Details can be seen in document [8].

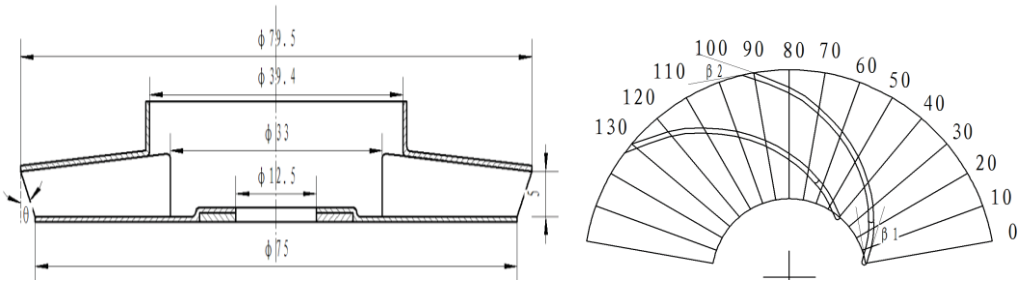

Fig. 1 Impeller

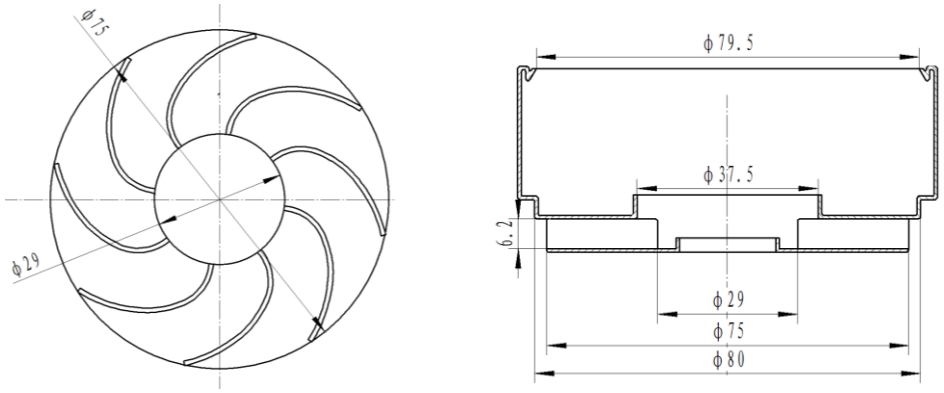

Fig. 2 Guide vane

2.2 Hydraulic design of guide vane

In order to significantly reduce y the production cost of stamping well pump, the common vaned diffuser is replaced by cylindrical return guide vane. That's because its axial length is short and its production process is very simple. The structure can be shown in Fig.2.

3. Orthogonal test design

3.1 Test purpose

Explore the law how geometric parameters influence the efficiency and head at rated point

3.2 Test factors

The theory head of pump can be got by Euler's equation, which is shown as follows:

$$H_t = \frac{u_2 v_{u2} - u_1 v_{u1}}{g} = \frac{u_2}{g}\left(u_2 h_0 - \frac{Q_t}{\pi D_2 b_2 \varphi_2 tg\beta_2}\right) - \frac{u_1 v_{u1}}{g} \tag{1}$$

And u_1、u_2 —impeller blade inlet and outlet peripheral speed; v_{u1}, v_{u2} —impeller blade inlet and outlet circumferential component of absolute velocity; g —acceleration of gravity; Q_t—theory flow; h_0—Stodala slip coefficient, $h_0 = 1-(\pi / z)\sin\beta_2$; φ_2 — impeller blade outlet exclusion coefficient, $\varphi_2 = 1-\frac{zs_{u2}}{\pi D_2} = 1-\frac{z\delta}{\pi D_2 \sin\beta_2 \sin\gamma}$; D_2 —impeller outlet diameter; β_2 —impeller blade outlet placed angle; Z — impeller blade number;

As can be seen from the above formula, the theory head of pump is only decided by impeller, but the efficiency of pump is jointly determined by impellers and guide vanes, so this orthogonal experiment integrates the structure parameters of impellers and guide vanes. The following seven geometric parameters are selected as test factors: D_{2min} (outer diameter of impeller rear floor), β_1（impeller blade inlet placed angle, β_2（impeller blade outlet placed angle, b_2 (impeller blade outlet width), B_3 (guide vane inlet width), Z_1 (impeller blade number), and Z_2 (guide vane blade number).

3.3 Test levels

According to the velocity coefficient method, relevant geometric parameters are determined and three levels are chosen, which is shown in Table 1.

Table 1 Orthogonal experimental factors

	Factors						
	A	*B*	*C*	*D*	*E*	*F*	*G*
Level	θ(°)	β_2(°)	b_2(mm)	B_3(mm)	β_1(°)	Z_1	Z_2
1	25	25	4	5.2	35	7	7
2	15	34	5	6.2	50	9	8
3	0	40	6	7.2	65	11	9

3.4 Determine the test program

According to the orthogonal table, list the test program, which is shown in Table 2. When test plan is finalized, tests must be done in strict accordance with the number order, which can not be altered arbitrarily.

4. Numerical simulation and result analysis

Considering 18 groups of impellers and guide vanes which are made from prototype manufacturing will incur high cost and will be subject to errors which are inevitably. In combination with consideration that current computational fluid dynamics (CFD) technology has been able to reflect truly the internal flow field distribution of centrifugal pumps and predict accurately the head, efficiency and shaft power of pumps at rated conditions [9]. Therefore, by using flow analysis results, we can forecast preliminarily whether the pump performances meet the design requirements.

Table 2 Test scheme

No.	*A*	*B*	*C*	*D*	*E*	*F*	*G*
1	25	34	4	6.2	65	7	7
2	25	25	6	5.2	50	9	8
3	25	40	5	7.2	35	11	9
4	15	25	5	6.2	50	9	9
5	15	34	6	7.2	65	7	8
6	15	40	4	5.2	35	11	7
7	0	34	6	6.2	50	7	7
8	0	40	5	5.2	35	9	8
9	0	25	4	7.2	65	11	9
10	25	25	6	7.2	35	11	8
11	25	40	4	5.2	65	7	9
12	25	34	5	6.2	50	9	7
13	25	34	4	7.2	35	7	8
14	25	25	5	6.2	65	9	7
15	25	40	6	5.2	50	11	9
16	15	25	6	6.2	65	7	9
17	15	34	4	7.2	50	11	8
18	15	40	5	5.2	35	9	7

4.1 Computational domain

Stainless steel stamping well pump is one of multi-stage pumps. Compared with single-stage pump, the structure of multi-stage pump is more complex and its flow characteristics are different. In the first impeller inlet of multi-stage pump the flow is usually irrotational while rotational in the other impeller inlet. Therefore, it's particularly important to select appropriate series when making numerical simulation for multi-stage pump. In scheme 1, four different series in a numerical simulation are selected and the efficiency and head at all series are shown in Table 3 and Table 4.

Table 3 Efficiency comparisons of different stages

Series (n)	1	2	3	4
The first-stage efficiency (%)	54.65	54.97	54.82	54.84
The second-stage efficiency (%)		57.53	57.61	57.61
The third-stage efficiency (%)			57.65	57.63
The fourth-stage efficiency (%)				57.69
The total efficiency (%)	50.68	54.29	55.23	55.21

Table 4 Head comparisons of different stages

Series (n)	1	2	3	4
The first-stage head (m)	3.918	3.940	3.930	3.931
The second-stage head (m)		3.784	3.766	3.771
The third-stage head (m)			3.768	3.788
The fourth-stage head (m)				3.798
The average head (m)	3.633	3.731	3.733	3.734

As can be seen from Table 3 and Table 4, the efficiency and head of the first-stage in different stages are almost the same. When the series is $n \geq 2$, there is little difference between the second stage and the following, but the difference is big compared with the first stage. It is also consistent with the fact that the flow in the first impeller inlet of multi-stage pump is usually irrotational while rotational in the other impeller inlet. Taking into account that increase of stage will bring about more grid number, thereby demand computer with higher performance, so select two-stage model to study and take the efficiency as well as head of the second stage as a performance prediction. The model consists of inlet section, two impellers, two guide vanes and outlet section. The solid models are respectively established and assembled together in Pro-E, which is shown in Fig.3.

4.2 Mode mesh

This mesh generation is completed by using special preprocessing software—Gambit, which is considered to be one of the best commercial CFD software preprocessor. In the whole mode unstructured tetrahedral mesh are used and the mesh of impeller and guide vane can be seen in Fig.4. The mesh generation process is more complicated, but it has excellent flexibility, especially for flow computational problem of complex boundary. In theory, with the increase of the mode grid number, the solution caused by the grid will be gradually reduced until it disappears. But the more the grid number, the slower the computing speed, thus considering the configuration of the computer and the computing time, grid number can not be too much. For the above hydraulic model, five different grid numbers of numerical simulations are selected; the results are shown in Table 5.

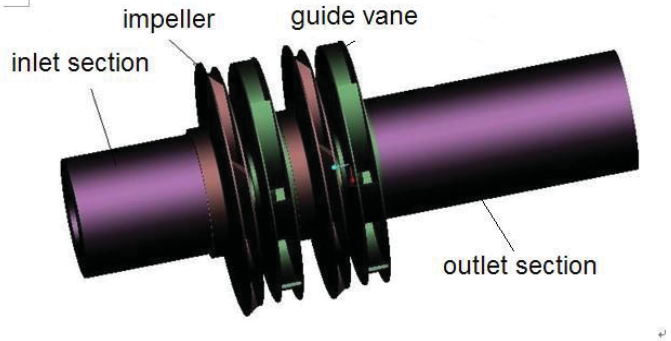

Fig. 3 Solid model of stamping well pump

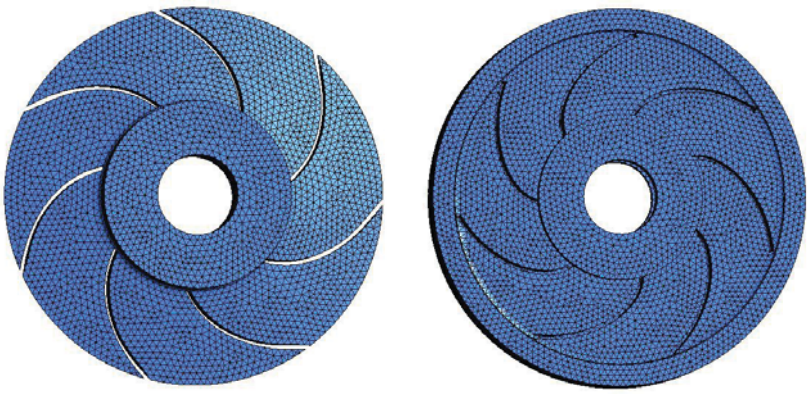

Fig. 4 Mesh of impeller and guide vane

Table 5 Grid independent analysis

Parameters	Grid size (mm)				
	1.0	1.2	1.4	1.6	1.8
Grid number	1594021	981844	671122	469287	350031
Efficiency η (%)	57.55	57.53	57.53	56.95	56.73
Single head H (m)	3.793	3.788	3.784	3.723	3.671

As can be seen from Table 5, when the grid size is large, the efficiency and single head at rated point are relatively small. If the grid size is less than 1.4mm, with the decrease of grid size, the efficiency and single head almost remain invariable. Taking into account the coordination of computing time and accuracy, 1.4mm of grid size meets the requirements, so the grid size of following studies is 1.4mm.

4.3 Boundary conditions and control equations

When making simulation calculations by CFD, standard k-ε turbulence model control equations and SIMPLEC algorithm are used. Besides, momentum, turbulent kinetic energy and turbulence dissipation rate all adopt second order upwind. Moreover, standard pressure item is selected. In order to accelerate convergence, various relaxation factors employ 0.3. The inlet and outlet of pump respectively adopt velocity inlet and outflow, the solid wall is not slip, namely relative velocity w=0.

4.4 Results and analysis

Through CFD 18 groups of impeller and guide vane are simulated in the whole flow field. The efficiency and single head at rated point are selected as evaluation index. The results are shown in Table 6 below.

Table 6 Summary of orthogonal test results

No.	1	2	3	4	5	6	7	8	9
H/m	3.78	4.33	5.28	4.48	4.54	4.10	4.71	4.87	3.79
η/%	57.53	59.41	58.96	60.15	53.68	53.33	53.37	55.44	53.13
No.	10	11	12	13	14	15	16	17	18
H/m	3.76	3.85	4.76	4.18	4.40	5.49	4.63	4.42	4.75
η/%	59.68	55.13	59.62	59.81	56.68	55.01	53.92	52.53	54.91

In order to analyze how the selected seven factors affected the performance of pump and find the main factors, the results of orthogonal test are studied by the range analysis. The calculated process is as follows:

The head index at rated point of column 1:

$$K_{1A}=3.78+4.33+5.28+3.76+3.85+4.76=25.27$$
$$K_{2A}=4.48+4.54+4.10+4.18+4.40+5.49=27.19$$
$$K_{3A}=4.71+4.87+3.79+4.63+4.42+4.75=27.17$$

In the formula, K_{1A}, K_{2A}, K_{3A} respectively show the sum of simulation result when factor A is 1, 2, and 3. To make comparison with A of different levels, k is introduced.

$$k_{1A}=25.27/6=4.29;\ k_{2A}=27.73/6=4.53;\ k_{3A}=27.47/6=4.53$$

In the formula, k_{1A}, k_{2A}, k_{3A} respectively show the single head at rated point when factor A is 1, 2, and 3. The calculation methods of the remaining six columns are the same as that of the first column, and the results are filled in Table 7.

'R' in each column can be obtained by the maximum of k_{1A}, k_{2A} and k_{3A} minus the minimum of k_{1A}, k_{2A} and $k_{3A.}$ For example: R_A=max $\{k_{1A}, k_{2A}, k_{3A}\}$ -min $\{k_{1A}, k_{2A}, k_{3A}\}$ =4.53-4.29=0.24.

Table 7 Range analysis of head at rated point

H/m	A	B	C	D	E	F	G
K_1	25.76	25.39	24.12	27.39	26.94	25.69	26.17
K_2	27.19	26.39	28.54	26.76	28.19	27.59	26.43
K_3	27.17	28.34	27.25	25.97	24.99	26.84	27.52
k_1	4.29	4.23	4.02	4.57	4.49	4.28	4.36
k_2	4.53	4.40	4.76	4.46	4.70	4.60	4.41
k_3	4.53	4.72	4.54	4.33	4.17	4.47	4.59
R	0.24	0.49	0.74	0.24	0.53	0.32	0.23

Table 8 Range analysis of efficiency at rated point

η/%	A	B	C	D	E	F	G
K_1	350.33	346.47	334.46	333.23	343.13	334.44	333.06
K_2	341.16	337.54	347.26	342.77	341.59	347.71	343.93
K_3	325.33	332.78	333.68	340.79	332.07	334.64	339.8
k_1	58.39	57.75	55.74	55.54	57.19	55.74	55.51
k_2	56.86	56.26	57.88	57.13	56.93	57.95	57.32
k_3	54.22	55.46	55.61	56.80	55.35	55.77	56.63
R	4.17	2.29	2.27	1.59	1.76	2.21	1.79

The size of range reflects the role of various factors in the orthogonal test. Large range indicates that this factor change d in the test spectrum making a more important impact on the efficiency or head, and this factor is usually an important factor. According to the size of range in Table 7 and Table 8, primary and second factors can be found which are shown in Table 9.

Table 9 Influence order of geometric parameters to performance

Index	High-Low						
H	b_2	β_1	β_2	Z_1	θ	B_3	Z_2
η	θ	β_2	b_2	Z_1	Z_2	β_1	B_3

For a single factor, the factor A has the influence order on head as $A_2A_3A_1$ and efficiency as $A_1A_2A_3$; the factor B has the influence order on head as $B_3B_2B_1$ and efficiency as $B_1B_2B_3$; the factor C has the influence order on head

as C_2 $C_3C_1$and efficiency as C_2 C_3C_1; the factor D has the influence order on head as $D_1D_2D_3$ and efficiency as $D_2D_3D_1$; the factor E has the influence order on head as $E_2E_1E_3$ and efficiency as $E_1E_2E_3$; the factor F has the influence order on head as $F_2F_3F_1$ and efficiency as $F_1F_3F_2$; the factor G has the influence order on head as $G_3G_2G_1$ and efficiency as $G_2G_3G_1$.

To sum up, the best combination of head is $A_2B_3C_2D_1E_2F_2G_3$; and the best combination of efficiency is $A_1B_1C_2D_2E_1F_2G_2$.

The purpose of this orthogonal experiment is that, under the premise of satisfying single head, the maximum efficiency at rated point can be obtained. The best efficiency combination of $A_1B_1C_2F_2G_2E_1D_2$ namely impeller outlet slope θ=25°, blade outlet placed angle β_2=25°, blade outlet width b_2=5mm, impeller blade number Z_1=9, guide vane blade number Z_2=8, blade inlet placed angle β_1=35° and guide vane inlet width B_3=6.2mm. Through CFD the performance of the pump are predicted that the single head and efficiency respectively are 4.61m and 61.41%. Compared with 18 results in Table 6, the efficiency is significantly improved and the optimal solution is not included in those 18 programs, which fully embodies the advantages of orthogonal test.

5. Quadratic regression orthogonal test methods

Quadratic regression orthogonal test methods are also response surface methods, which use quadratic regression equation to fit the function relationship between each factor and response value. Through the analysis of the regression equation, the optimal combination of geometric parameters can be found. It's a statistical method to solve multi-variable problems [10-11].

5.1 Test factors

Through the analysis of seven factors ahead by orthogonal test, the conclusion came out that the impeller outlet slope θ, blade outlet placed angle β_2 and blade outlet width b_2 were the most three important factors affecting the efficiency of stamping well pump. In this study, response surface method was adopted to analyze the relationships between these three factors、β_2 (15°～40°) 、b_2 (3mm～8mm) 、θ (0°～45°) and test indicators (efficiency) within the range. The other four factors were selected by orthogonal optimal level: Z_1=9、Z_2=8、β_1=35°、B_3=6.2mm. Then, 16 impellers were designed.

5.2 Level code of factors

Star arm length formula is as follow: (Proof process can be seen in document [12]

$$r = \sqrt{\frac{\sqrt{(m_c + 2m + m_0)m_c} - m_c}{2}} \tag{2}$$

In the formula: r — star arm length; m_c — the number of two level test

m — the number of factors; m_0 —the number of zero level test

As the number of factors is equal to 3, if the number of zero level test takes 2, the number of two level test $m_c=2^3=8$. According to formula (1), star arm length r=1.287.

Because the range of factor x_1 is 15°~40°, it can be calculated that zero level x_{10}=27.5° and changing interval Δ_1=(40-27.5)/1.287=9.71. So the up level x_{12}=27.5+9.71=37.21° and the down level x_{22}=27.5-9.71=17.79°. Similarly, the codes of blade outlet width b_2 *and* impeller outlet slope θ are also calculated shown in Table 10.

Table 10 Factors and levels

Design variable z_i	Natural variable x_i		
	x_1（β_2）/°	x_2（b_2）/mm	x_3（θ）/°
Up star arm r	40	8	45
Up level 1	37.21	7.44	39.98
Zero level 1	27.5	5.5	22.5
Down level -1	17.79	3.56	5.02
Down star arm -r	15	3	0
Change interval Δ_i	9.71	1.94	17.48

5.3 Orthogonal combination design

As the number of factors is equal to 3, the orthogonal table $L_8(2^3)$ is selected. Then, the number of zero level test takes 2, the number of two level test $m_c=2^3=8$, and the number of star test 2m=6, which are shown in Table 11. Finally, 16 groups of hydraulic model are designed through the last calculation value of other geometrical factors.

Table 11 Test programs

No.	z_1	z_2	z_3	β_2/°	b_2/mm	θ/°
1	1	1	1	37.21	7.44	39.98
2	1	1	-1	37.21	7.44	5.02
3	1	-1	1	37.21	3.56	39.98
4	1	-1	-1	37.21	3.56	5.02
5	-1	1	1	17.79	7.44	39.98
6	-1	1	-1	17.79	7.44	5.02
7	-1	-1	1	17.79	3.56	39.98
8	-1	-1	-1	17.79	3.56	5.02
9	1.287	0	0	40	5.5	22.5
10	-1.287	0	0	15	5.5	22.5
11	0	1.287	0	27.5	8	22.5
12	0	-1.287	0	27.5	3	22.5
13	0	0	1.287	27.5	5.5	45
14	0	0	-1.287	27.5	5.5	0
15	0	0	0	27.5	5.5	22.5
16	0	0	0	27.5	5.5	22.5

Efficiency of these 16 groups well pump are gained by numerical simulation, and it forms quadratic regression equation of efficiency on β_2, b_2, θ, namely $y=f(x_1, x_2, x_3)$. Although this regression equation is nonlinear, if x_1x_2, x_1x_3, x_2x_3, x_1^2, x_2^2, x_3^2 were regard as six variables respectively, the above three- variable quadratic regression equation becomes nine- variable linear equation. Regression coefficients can be determined using "Regression" tool in Excel, as well as the significance of the regression equation. This method can not only greatly reduce the workload, but also improve the accuracy of the calculation.

Firstly, the raw data are handled properly. Values of x_1x_2, x_1x_3, x_2x_3, x_1^2, x_2^2, x_3^2 need to be calculated, which are shown in Table 12.

Table 12 Regression analysis of raw data

N0.	x_1	x_2	x_3	x_1x_2	x_1x_3	x_2x_3	x_1^2	x_2^2	x_3^2	y/%
1	37.21	7.44	39.98	276.84	1487.66	297.45	1384.58	55.35	1598.40	57.32
2	37.21	7.44	5.02	276.84	186.79	37.35	1384.58	55.35	25.20	53.60
3	37.21	3.56	39.98	132.47	1487.66	142.33	1384.58	12.67	1598.40	55.14
4	37.21	3.56	5.02	132.47	186.79	17.87	1384.58	12.67	25.20	49.47
5	17.79	7.44	39.98	132.36	711.24	297.45	316.48	55.35	1598.40	59.64
6	17.79	7.44	5.02	132.36	89.31	37.35	316.48	55.35	25.20	57.58
7	17.79	3.56	39.98	63.33	711.24	142.33	316.48	12.67	1598.40	38.49
8	17.79	3.56	5.02	63.33	89.31	17.87	316.48	12.67	25.20	28.79
9	40	5.5	22.5	220.00	900.00	123.75	1600.00	30.25	506.25	57.26
10	15	5.5	22.5	82.50	337.50	123.75	225.00	30.25	506.25	59.14
11	27.5	8	22.5	220.00	618.75	180.00	756.25	64.00	506.25	58.38
12	27.5	3	22.5	82.50	618.75	67.50	756.25	9.00	506.25	40.41
13	27.5	5.5	45	151.25	1237.50	247.50	756.25	30.25	2025.00	59.47
14	27.5	5.5	0	151.25	0.00	0.00	756.25	30.25	0.00	53.51
15	27.5	5.5	22.5	151.25	618.75	123.75	756.25	30.25	506.25	60.53
16	27.5	5.5	22.5	151.25	618.75	123.75	756.25	30.25	506.25	60.53

5.4 Quadratic regression equations

Enter the regression dialog box, fill in the content, and the results are as follows.

Partial regression coefficients b_i: -88.13，2.71，31.95，0.75，-0.29，-0.0018，-0.035，-0.015，-1.78，-0.008. Therefore, the expression of regression equation shows:

$$y=-88.13+2.71x_1+31.95x_2+0.75x_3-0.29x_1x_2-0.0018x_1x_3-0.035x_2x_3-0.015x_1^2-1.78x_2^2-0.008x_3^2 \quad (3)$$

5.5 Significance test of the regression equations

4.5.1 F-test

Through the regression analysis in the Excel, variance is show in Table 13. F=15.40, which is greater than the corresponding critical value $F_{0.01}$ (9, 6) = 7.98. Therefore, the linear regression of equation (1) is significant, which means there is remarkable regression relationship between efficiency and three factors.

Table 13 Variance Analysis Table

Difference	*SS*	*df*	*MS*	*F*	$F_{0.01}$（9，6）	Significance
regression	1243.14	9	138.13	15.40	7.98	**
Residual Error	53.8	6	8.97			
Summation	1296.94	15				

Note: *SS* — sum of squares; *df* — degrees of freedom; *MS* — mean square; *F* — test statistics

4.5.2 Multiple correlation coefficient tests

Multiple correlation coefficient R is equal to 0.979 through the regression analysis in the Excel. It is greater than corresponding critical value $R_{\min}$, which is equal to 0.896. So, the linear regression equation (2) fits well with the experimental data, which agrees with results of F- test.

5.6 Determine the optimal program

According to c extreme conditions:

$$\frac{\partial y}{\partial x_1}=0 \qquad \frac{\partial y}{\partial x_2}=0 \qquad \frac{\partial y}{\partial x_3}=0 \tag{4}$$

Solve equation (4):

$$2.71-0.29x_2-0.0018x_3-0.03x_1=0 \tag{5}$$

$$31.95-0.29x_1-0.035x_3-3.56x_2=0 \tag{6}$$

$$0.75-0.0018x_1-0.035x_2-0.016x_3=0 \tag{7}$$

Results: x_1=23.2，x_2=6.8，x_3=29.4.

When β_2=23.2°，b_2=6.8mm，the theoretical prediction of the efficiency of stamping pump reaches 62.8% according to formula (3). Modeling in accordance with the above geometric parameters, the numerical simulation value of efficiency equal to 62.98%, whose error is less than 1% compared with the theoretical prediction. It shows that the optimization of stamping stainless steel well pump is feasible using response surface methodology.

5.7 Test analysis of the optimum solution model

In order to validate the success of this optimization design in stainless steel stamping well pump, the optimal model of the program is entrusted to Taizhou Yongxin Pump Company to manufacture, and do performance experiment in the test stand of Product Quality Supervision Center for Irrigation and Drainage (Zhenjiang) ,which is owned to Research Center of Fluid Machinery Engineering and Technology, Jiangsu University .The test stand has been identified by the Ministry of Water Resources and Ministry of Machinery, and it is up to national 1 level and international A-level accuracy. The whole flow field simulations of the optimal mode are done in the five conditions (Q=4.8、Q=6.4、Q=8、Q=9.6、Q=11.2 m^3/h), and comparison of the predicted performance and experimental performance are shown in Fig.5.

It can be seen in Fig.5, simulation value and test value are consistent with fairly well in rated flow and high flow, and the variance is less than 1%. In small flow, the fluid in the impeller and guide vane is easy to produce flow separation and there are some differences between actual flow and simulating flow resulting in 2% deviation between simulation value and test value. Thus, the credibility of numerical simulation in the whole flow field is high, which can predict the performance of pump instead of doing experiment.

From the Fig.5, the efficiency of this pump reaches 61.36% at rated point, and single stage head reaches 4.85m. By looking up the well pump standard of People's Republic of China (GB/T 2816—2002), the efficiency of the pump 100QJ8 should be 53%. At the same time, the efficiency of the same pump produced by Grundfos is 60%, and the single head is only 4.0m. So the design of the stainless steel stamping well pump is successful.

Fig.6 shows the same type well pumps with 100mm of well diameter, 8m^3/h of flow, and 9 impellers. The left pump is the optimal pump of 100XQJ8-43/9, and the other one is international brand of 4SP8A-9. Table 14 shows the parameter comparisons of two pumps.

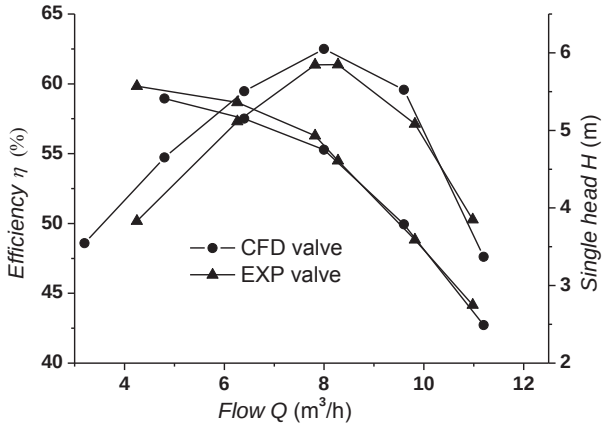

Fig. 5 Comparison chart of simulation and experimental value

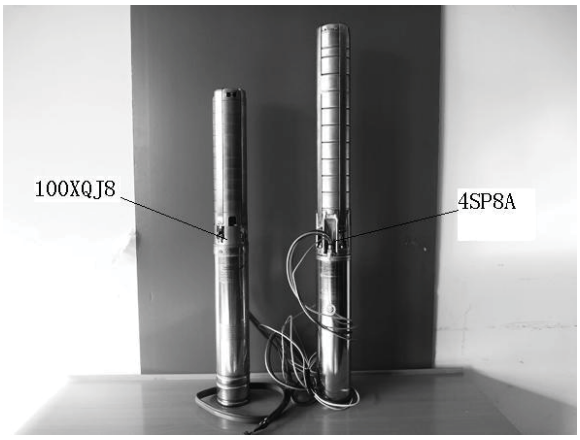

Fig. 6 Comparison of different pumps

Table 14 Parameters comparison of two pumps

Parameters	100XQJ8-43/9	4SP8A-9
Flow Q (m^3/h)	8	8
Total head H (m)	43	36
Single stage head H_i (m)	4.8	4
Efficiency η (%)	61.36	60
Out diameter(mm)	87	87
Length (m)	0.825	0.985
Price (￥)	1500	10000

6. Conclusions

(1) By using Fluent, 18 groups of stainless steel stamping well pump arranged by orthogonal combination are calculated in the whole flow field. Through the analysis of range of efficiency, this study establishes that the influence order of selected geometric parameters on efficiency is θ、β_2、b_2、Z_1、Z_2、β_1、B_3.

(2) Impeller outlet slope θ, blade outlet placed angle β_2 and blade outlet width b_2 are selected, which are most obvious parameters affecting the pump efficiency. The function relationship between pump efficiency and three parameters was fitted by using quadratic regression equation. Through the analysis of the regression equation, the optimal combination of geometric parameters could be found and stainless steel stamping well pump with excellent performance could be designed.

(3) From the results of test and simulation, numerical simulation in the whole flow field can accurately guide the design of the stainless steel stamping Well pump. It can help to design well pump with high efficiency and head by adopting impeller maximum diameter design method.

Acknowledgment

This article is completed under the careful guidance of Professor Weigang Lu and Professor Weidong Shi, so I would like to express my most sincere gratitude to them. Otherwise, this work was financially supported by the Priority Academic Program Development of Jiangsu Higher Education Institutions.

References

[1] W. D Shi, H. L Wang and X. J Yu. Development and Prospect of Deep Well Pump in China, *Drainage and Irrigation Machinery*, Vol. 27, No. 1, pp. 64-68, 2009.

[2] C. L Yao, C. H Wang , K. Li et al. Characters and Current Developments of Stamping and Welding Centrifugal Pump, *Manufacturing Automation*, Vol. 28, pp. 214-215, 2006.

[3] S.Q Quan. *Design Theory of Low Specific Centrifugal Pump*, China Machine Press, 1997.

[4] H. L Wang, W. D Shi, W. G Lu et al. Optimization Design of Deep Well Pump Based on Latin Square Test, *Transactions of the Chinese Society for Agricultural Machinery*, Vol. 41, No. 5, pp. 56-63, 2010.

[5] L. Zhou, W. D Shi, W. G Lu et al. Orthogonal Test and Optimization Design of Submersible Pump Guide Vanes, *Drainage and Irrigation Machinery*, Vol. 29, No. 4, pp. 312-315, 2011.

[6] G. H Liu, W. X Liu and H. P Qiao. Mathematic Simulation of Major Cultivation Factors for High Yield of Fodder Beet by Quadratic Orthogonal Regression Design, *Agricultural Research in the Arid Areas*, Vol. 23, No. 4, pp. 143-146, 2005.

[7] W.G Lu, Q. H Zhang and W. D Shi. Impeller Diameter Maximum Approach on Deep Well Pumps, *Drainage and Irrigation Machinery*, Vol. 24, No. 6, pp. 13-76, 2006.

[8] X. F Guan. *Pump Manual*, China Astronautic Publishing House, 1995.

[9] Golcu M, Pancar Y and Sekmen Y. Energy Saving in a Deep Well Pump with Splitter Blade, *Energy Conversion and Management*, Vol. 47, No. 5, pp. 638-651, 2006.

[10] J. Li, G. Wang, X. Lv et al. Nutritional Condition Optimization of Organic Solvent Resistance Lipase by Response Surface Methodology, *Biology Technology*, Vol. 20, No. 4, pp. 66-69, 2010.

[11] H. M Zhu and M. Zhao. Extraction and Ant-Oxidation Properties of Seabuckthom Pigment, *Chemistry and Industry of Forest Products*, Vol. 30, No. 4, pp. 78-84, 2010.

International Journal of Comprehensive Engineering
Part C, 2(1), 78-85, 2013
Doi: 10.14270/IJCE2013.2.1.c78
Regular paper

ISSN 2186-2680
e-ISSN 2186-2656
www.iace-journal.org

Insulating Packaging Solutions Based on Spherical Shell Model

Jing Qian [1, #] and Jiada Mo [2]

[1] School of Mechanical Engineering, Jiangnan University, Wuxi, 2140122, Jiangsu, China
[2]Department of Mechanical Engineering, University of Memphis, Memphis, 38117, TN, USA

[#] Corresponding author: qj639@163.com; Tel.: +86-510-8591-0562; Fax: +86-510-8591-0562

Abstract: The spherical shell model considering three heat-transfer modes is developed. Relationships among wall thickness, inside radius, package duration, ambient temperature, convection coefficients, emissivity of the insulated material surface and product size are developed and discussed. General conclusions are reached as to these variables and input parameters. Based on this model, the optimal insulating packaging solution is achieved by using 'minimum packaging cost' as an optimization target. This optimized design on the spherical shell model can be then transformed back to rectangular configurations by using the same rule used for transforming rectangular configurations to the spherical shell configuration. The comparison of results predicted from the present model with benchmark experimental data show satisfactory agreement in terms of packaging duration.

Keywords: Insulating Package, Heat Transfer, Spherical Shell Model, Packaging Solution.

Received: May 18,2012 / Accepted: Nov. 6,2012 / Published: Apr. 8,2013

1. Introduction

Insulating package can protect temperature-sensitive products and keep the temperature within an appropriate temperature range in varying temperature environments during shipping.

Lots of researchers have developed different mathematical models to predict the capability of the insulating package system which already existed [1][2]. Based on the existing insulating package systems, investigators developed expressions of the insulating package system R-value (thermal resistances) for determining heat transfer on a one-dimensional plane surface and subsequently for predicting the quantity of Phase Change Material (PCM) or the allowable shipping time which the insulating package system can provide under specific ambient temperature and desired product temperature[3][4]. Unfortunately, before shipping a temperature-sensitive product, neither the interrelated dimension of an insulated container nor the quantity of PCM is usually known. But all parameters of the insulating package system need to be determined by the designers to successfully protect the product.

Normally, all information given to the packaging designer is type of product, probably shipping time and ambient temperature. Base on these parameters the designer should determine the insulating container (material, size etc.) and the phase-change material (type of material, amount etc.). To realize the insulating packaging design, a spherical shell model has been developed (see Fig.1 and Eq.(1)and Eq.(2) as followed). The spherical shell model in this research has been confirmed by using finite element computer program and experiments [5][6]. This model is an appropriate tool to transfer a rectangular insulating container to a spherical shell which the inner volume of spherical shell model equals the inner volume of the rectangular container and the thickness in one equals that in the other. Research shows when the ratio of maximum and minimum side of rectangular container is not more than 2.5, the conversion model has enough accuracy for engineering design

$$r_i = \sqrt[3]{L \cdot W \cdot H / (\frac{4}{3}\pi)} \tag{1}$$

$$r_o = r_i + \Delta x \tag{2}$$

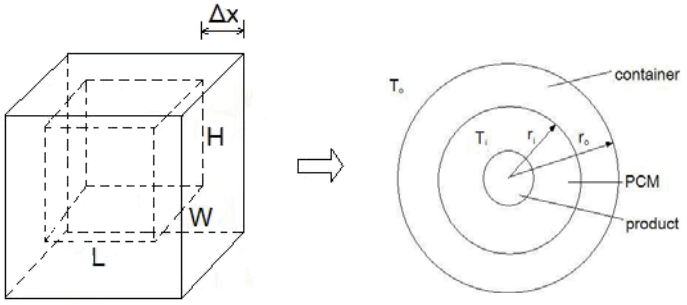

Fig. 1 Insulated package conversion model

Using the mathematical model developed in this research, effects of different parameters on thermal capability of the insulating package are discussed, and insulating packaging solutions are achieved.

2. Spherical shell models for packaging systems considering different heat transfer modes

To predict the effect of three different heat transfer modes (conduction, convection and radiation) for the insulating package, then three different models are developed as following. In this research, we suppose all the heat transfer is absorbed by phase change material.

2.1 Mathematical model only with conduction

When a mathematical model only considers conduction, the heat transfer rate through a spherical shell can be expressed as:

$$\frac{4\pi \cdot r_o \cdot r_i \cdot k \cdot (T_o - T_i)}{r_o - r_i} = m_{ice} \cdot \Delta H / t$$
$$= \frac{4}{3}\pi \cdot \rho \cdot (r_i^{\,3} - r_p^{\,3}) \cdot \Delta H / t$$

where ΔH is the latent heat of PCM in KJ/Kg, ρ is the density of the PCM in kg/m^3; r_p is the radius of the product (The principle of this transition is volume equaling) in s, t is duration of package (the melting time of PCM) in s, k is the thermal conductivity of the insulating material in $W/m\cdot{}^\circ C$, T_i and T_o are the inside and outside temperatures of spherical shell in $^\circ C$, r_i and r_o are the inside and outside radius of spherical shell in m, Δx is the thickness of container.

$$\Delta x = r_0 - r_i$$

Actually, r_i expresses the dosage of phase change material. The bigger the inside radius of spherical shell is, the more PCM used.

By manipulating above equations, the relationship between Δx and r_i can be achieved as:

$$\Delta x = \frac{3 \cdot r_i^{\,2} \cdot k \cdot (T_o - T_i) \cdot t}{\rho \cdot (r_i^{\,3} - r_p^{\,3}) \cdot \Delta H - 3 \cdot r_i \cdot (T_o - T_i) \cdot k \cdot t} \tag{3}$$

2.2 Mathematical model with external convection

In most cases, involving the distribution of insulating packages, the packages are located on the floor or on pallets which are in the warehouse or the distributing vehicle without any mechanical air-circulating device. For this reason, most of the convection heat transfers to and from insulating packages occur by natural convection.

When considering the external convection, the outside surface temperature of the insulating package is T_o and the ambient temperature is T_∞. T_o and T_∞ are different. With the spherical shell model, a heat transfer balance can be established to yield the following equation

$$Q = h_a \cdot A_o \cdot (T_\infty - T_o) = \frac{4\pi r_o r_i k(T_o - T_i)}{r_o - r_i} \tag{4}$$

where h_a is the average convection heat transfer coefficient on the surface in $w/m^2 \cdot °c$

Therefore, the temperature of outside surface T_o can be formulated as

$$T_o = \frac{r_i k T_i + h_a \cdot \Delta x \cdot (r_i + \Delta x) \cdot T_\infty}{r_i k + h_a \cdot \Delta x \cdot (r_i + \Delta x)} \tag{5}$$

Since all heat transfer flow through the insulated wall is absorbed by the phase change material, the following equation can be obtained:

$$Q = h_a \cdot A_o \cdot (T_\infty - T_o) = \frac{4}{3}\pi\rho(r_i^{\,3} - r_p^{\,3}) \cdot \Delta H / t$$

By applying Eq.(5) to the above equation, the final working equation（The relationship between Δx and r_i ）is obtained:

$$3 \cdot t \cdot h_a \cdot k \cdot r_i \cdot (r_i + \Delta x)^2 \cdot (T_\infty - T_i) - \rho \cdot \Delta H \cdot (r_i^{\,3} - r_p^{\,3}) \cdot [r_i k + h_a \cdot \Delta x \cdot (r_i + \Delta x)] = 0 \tag{6}$$

2.3 Mathematical model with external convection and radiation

When an insulating package is transported on a highway in summer, the inside temperature of the truck trailer can be over $60°C$. In this case, not only must convection be considered but radiation cannot be neglected.

With the combination of convection and radiation on the spherical shell model, the heat transfer from outside to inside of the insulating package can be expressed by the following equation:

$$\begin{aligned} h_a \cdot A_o \cdot (T_\infty - T_o) + \varepsilon\sigma A_o (T_\infty^{\,4} - T_o^{\,4}) &= \frac{4\pi r_o r_i k(T_o - T_i)}{r_o - r_i} \\ &= \frac{4}{3}\pi\rho(r_i^{\,3} - r_p^{\,3}) \cdot \Delta H / t \end{aligned} \tag{7}$$

From Eq.(7), the temperature of the outside surface on a spherical shell model T_o can be expressed as follows.

$$T_o = T_i + \frac{\rho \cdot (r_i^{\,3} - r_p^{\,3}) \cdot \Delta H \cdot \Delta x}{3t \cdot (r_i + \Delta x) \cdot r_i \cdot k} \tag{8}$$

Substituting Eq.(8) into Eq.(7), the following relation can be achieved:

$$\begin{aligned} &3t \cdot h_a \cdot (r_i + \Delta x)^2 (T_\infty - T_i - \frac{\rho \cdot (r_i^{\,3} - r_p^{\,3}) \cdot \Delta H \cdot \Delta x}{3t \cdot (r_i + \Delta x) \cdot r_i \cdot k}) \\ &+ 3t \cdot \varepsilon \cdot \sigma \cdot (r_i + \Delta x)^2 [T_\infty^{\,4} - (T_i + \frac{\rho \cdot (r_i^{\,3} - r_p^{\,3}) \cdot \Delta H \cdot \Delta x}{3t \cdot (r_i + \Delta x) \cdot r_i \cdot k})^4] \\ &= \rho \cdot (r_i^{\,3} - r_p^{\,3}) \cdot \Delta H \end{aligned} \tag{9}$$

Normally, the emissivity(ε in Eq.(9)) of EPS foam is 0.9. The other parameters in Eq.(3)、Eq.(6) and Eq.(9) are taken to be the same as the following:

$$t = 48hours; \quad h_a = 3.46w/m^2 \cdot °c; \quad T_\infty = 50°C; \quad \rho = 900Kg/m^3;$$
$$\Delta H = 335000\,J/Kg; \quad k = 0.042w/m \cdot °C; \quad T_i = 0°C; \quad r_p = 0.07m$$

Based on these three mathematical models with the same parameters, one can get these three curves in Fig. 2, which express the inside radius plotted against the thickness of the shell. These represent predictions based on the model of considering only conduction, convection, and combined convection and radiation, respectively.

Fig. 2 shows that, before the thickness of the shell reaches 20 mm, increasing the thickness of container can significantly decrease the inside radius of the shell (the quantity of the PCM as well). However, when the thickness of container is more than 40 mm all calculated solutions can be simplified as just considering conduction and ignoring the effect of convection and radiation.

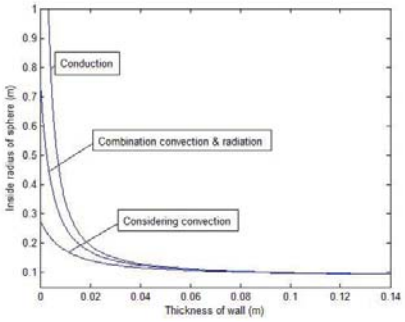

Fig. 2 Inside radius - thickness curves considering different heat transfer modes

3. General conclusions based on spherical shell model

In most cases, involving the distribution of insulating packages, the packages are located on the floor or on pallets which are in the warehouse or the distributing vehicle without any mechanical air-circulating device. For this reason, most of the convection heat transfers to and from insulating packages occur by conduction, natural convection and radiation.

When some parameters in Eq.(9) are fixed, some pictures are used to show how parameters change with consideration of external convection and radiation. In these pictures, the effects of different parameters for insulating package are discussed.

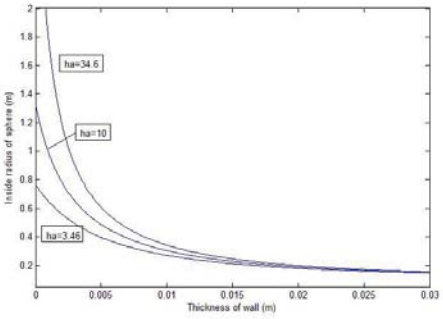

Fig. 3 $r_i - \Delta x$ Curves with h_a changed considering convection and radiation

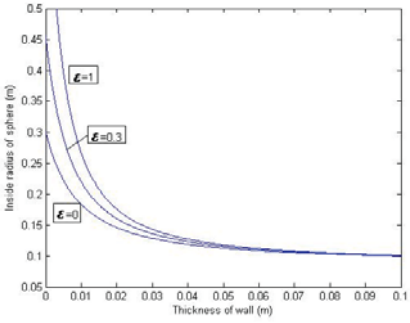

Fig. 4 $r_i - \Delta x$ Curves with ε changed considering convection and radiation

Fig. 3 shows that the convection coefficient is very sensitive to the inside radius of the shell when the thickness of the container is less than 5 mm. However, when the thickness of the container is over 20 mm, the effect of convection can be neglected.

Fig. 4 shows that usage of high emissivity material can play a significant role in reducing the quantity of PCM when the thickness of the shell is less than 40 mm. So a decrease in the effect of radiation can be achieved by covering the surface of insulating packge with high emissive material(such as aluminum foil). When $\varepsilon = 0$, this make a situation in which radiation is negligible. In fig. 4, it indicates that the outside radiation cannot be ignored when the thickness of the shell is less than 40 mm.

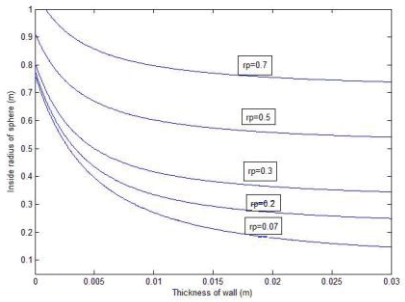

Fig. 5 $r_i - \Delta x$ **Curves with** r_p **changed considering convection and radiation**

Fig. 5 presents the $r_i - \Delta x$ curves as the size of the product changes. The result shows that the larger the product is, the greater is the amount of PCM needed.

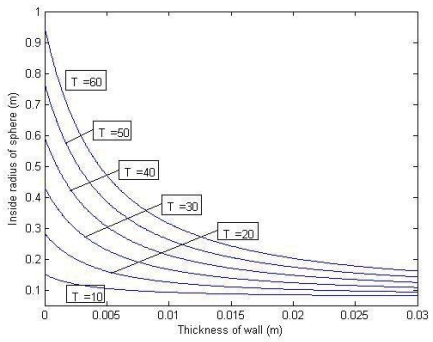

Fig. 6 $r_i - \Delta x$ **Curves with** T_∞ **changed considering convection and radiation**

Fig. 6 gives the $r_i - \Delta x$ curves when the ambient temperature is changed. It shows that at a higher ambient temperature, the heat gain of the package needs to be offset either with a thicker container or with a greater PCM dosage.

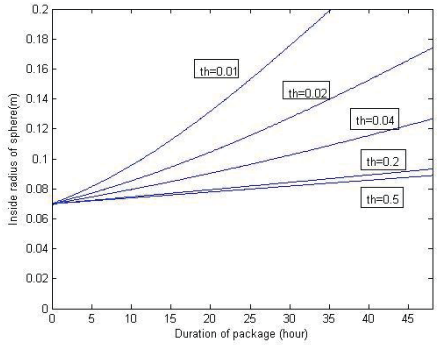

Fig. 7 $r_i - t$ **Curves with the thickness of the wall changed**

Fig. 7 shows that the longer duration a package needs, then the larger the inside radius of the shell needs to be, i.e. more PCM for a given product. The duration varies almost linearly with the inside radius of the shell. Again, a thicker shell can significantly reduce the dosage of PCM at first, whereas later increasing the thickness has less effect on the dosage of PCM when the thickness of the shell exceeds 40 mm.

4. Insulating packaging solutions

Based on the demands of a package (such as ambient temperature, shipping time and the size of product), the designer can apply the curve of $r_i - \Delta x$ (inside radius-thickness on spherical shell) for a set of given inputs. In this case the designer faces many options for inside radiuses and thicknesses. Each combination offers different package design solutions which can satisfy all the basic given requirements. However, if the designer wants to determine a single optional solution in terms of a set of specifics, then 'the minimum cost' rule is used as the optimized target. Lowest cost is the ultimate goal of the designer when the package can meet all of packaging functions. To simplify the explanation of the package solution, the single-wall spherical shell model is discussed in this section, with minimum packaging cost as an optimizing target for the insulating package design.

To reduce the cost of packaging is to reduce the cost of the package itself. In insulating packages, the packaging cost includes the cost of the packaging container and the PCM. In this case, the cost of the package can be expressed as follows:

$$\begin{aligned} Cost &= Cost \quad of \quad Container \quad + \quad Cost \quad of \quad PCM \\ &= Spherical \quad Shell \quad Mass \quad \times A \quad + \quad PCM\ Mass \quad \times \quad B \\ &= \frac{4}{3}\pi\rho_1(r_o^3 - r_i^3)\cdot A + \frac{4}{3}\pi\rho(r_i^3 - r_p^3)\cdot B \end{aligned} \tag{10}$$

where A is the cost of insulated material per unit mass. B is the cost of PCM per unit mass. ρ_1 and ρ are the density of the insulated material and PCM, respectively.

Therefore, to have an insulating package design, the procedure is:

1) Start from the curve of the inside radius-thickness of spherical shell ($r_i - \Delta x$). Eq.(9) provides the relationship between the inside radius r_i and the thickness of spherical shell Δx when both outside convection and radiation are considered.

2) Determine related parameters from the inputs in Eq.(9). To shorten the experiment time, assume the duration of the package is 24 hours (like domestic shipping). All parameters in the equation are shown as following.

$$t = 24hours; \qquad h_a = 5.485w/m^2\cdot{}^\circ c; \qquad T_\infty = 50^\circ C; \qquad \rho = 600Kg/m^3;$$
$$\Delta H = 335000\,KJ/Kg; \qquad k = 0.039w/m\cdot{}^\circ C; \qquad \varepsilon = 0.9 \qquad r_p = 0.075m$$

3) Generate the curve of the inside radius-thickness of spherical shell ($r_i - \Delta x$). Fig.8 shows the relationship between the inside radius and the thickness of the spherical shell when combination convection and radiation is considered for the above given set of inputs.

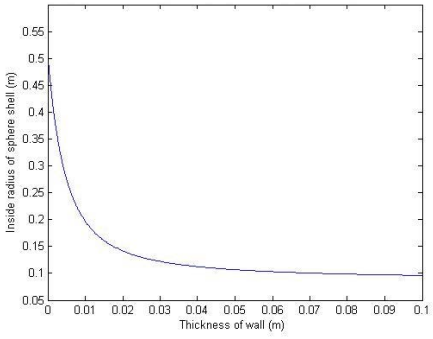

Fig. 8 Inside radius of shell – thickness of wall curve on package solution

4) Determine the design. After setting the optimizing target as the minimum cost, an additional relation can be created to determine the design condition on the curve. As indicated in the reference prices for insulated containers (such as EPS foam) on the website, the price of containers is \$6/kg and the price of broken ice is \$0.2/kg. Applying all the data to Fig. 8, one can derive the cost-thickness curve based on Eq.(9) as shown in Fig. 9.

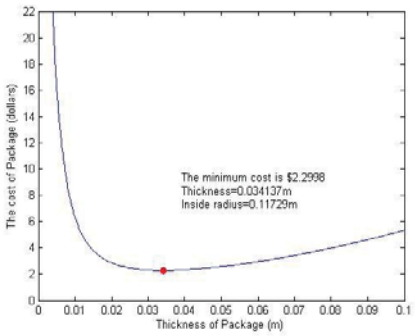

Fig. 9 Cost-thickness curve

Fig.9 shows that the minimum cost of package is $2.30 when the thickness of package is 34.1 mm and the inside radius of spherical shell is 117.3 mm from the given cost information of the materials. When $r_i = 0.1173m$; $r_p = 0.075m$, the quantity of ice can be calculated using this equation:

$$\frac{4}{3}\pi \cdot (0.11723^3 - 0.075^3) \cdot 600000 = 2988.8g$$

Therefore, not only is the design of the package complete, but the cost and the quantities of materials become available to users.

5) Return the spherical shell design to rectangular container design. It is well known that a spherical shell is not practical for packaging applications. The spherical shell model only serves as an analog for the purpose of packaging design. Designers should be able to transform the spherical shell back to a rectangular container. Let's begin with a cubic container with inside dimensions a. Based on the transforming principle developed in this research, the side a can be calculated by the following equation, equating the inner shell volume to the interior volume of the cube. Applying the optimized result of the inner shell radius, the inside side of sample cubic is:

$$a = (\frac{4}{3}\pi r_i^3)^{1/3}$$
$$= (\frac{4}{3}\pi \cdot 0.11723^3)^{1/3} = 0.1891m$$

To verify this optimized result, an experiment needs to be set up for the final container. Unfortunately, an exact dimension of the cubic container as given above is not available due to resource limitations. The radius of an available box (230x155x192x40mm) is 0.1178 m when it is transformed to the spherical shell. It exactly matches with the optimized result. But the thickness of the box is 40 mm, which is thicker than the calculated result (34.14mm). Using Fig. 8, when the thickness of container is 0.04m, the inside radius of spherical shell is 0.1134m and the quantity of broken ice is 2605 g. The box (230x155x192x40mm) is still a good choice because a thicker box can be considered as a safe factor for design. Therefore this box as an insulating container is chosen to be tested to verify the optimized design.

6) Verify package solution. A verification test is run on the chosen rectangular insulating container, loading the calculated amount of PCM (2988.8 g broken ice) into the container as a packaging prototype, setting up the experiment with ambient temperature, and obtaining the test data. The duration of the packaging system is selected to verify the modeling of the developed spherical shell model.

Fig. 10 shows the ambient temperature during the experiment. It can be seen that the ambient temperature is kept at 50 ℃.

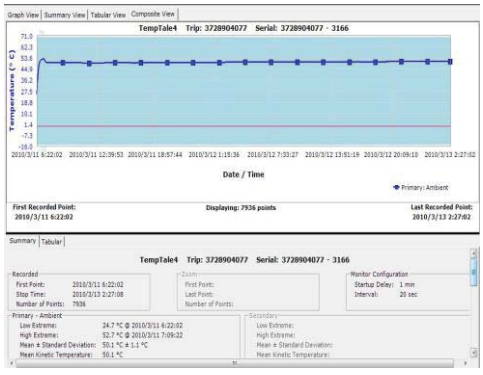

Fig.10 Ambient temperature on validation experiment

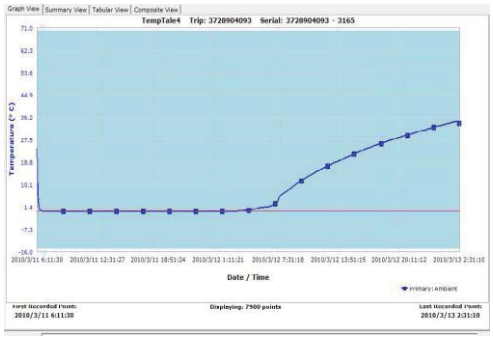

Fig. 11 Inside temperature on validation experiment

Fig. 11 shows the duration of the package is 25 hours and 5 minutes. Since the thickness of the rectangular container is greater than the thickness in the spherical shell model, the duration of the package in the experiment is 65 minutes longer. This demonstrates that the insulating package design is successful.

5. Conclusions and recommendations

In this research, a spherical shell model has been developed to simplify heat transfer analysis and the design of an insulating package. In general, when the thickness of container is more than 40mm, heat transfer calculation can be simplified as just considering conduction and ignoring the effect of convection and radiation.

The spherical shell model provides a working foundation for such a package design by transforming a rectangular insulated container to a spherical shell configuration. The closed form of the mathematical formulation for the various heat transfer modes through a spherical shell allows an analysis and optimization in the applications of insulating package design. The optimized package design under all given inputs is then transformed back to a rectangular configuration.

Applying the 'minimum cost' principle, a designer can decide the size of insulated container, the amount of PCM and the configuration of the packaging system from the general formulation of the solution of the spherical shell model. After this prototype packaging design is completed, a benchmark test has been set up and conducted to verify this theoretical solution.

As a result, this research work offers not only an effective mathematical model for the insulating package system, but also a unique transformation between the spherical and rectangular configurations, providing a straightforward tool, validated by benchmark experiments, for making insulating-package design for the packaging industry.

To confine or extend the current approach to more generic applications, the following recommendations should be made.

1) For those rectangular containers which are not suitable to apply the spherical shell model, a new model should be developed.

2) For further research work, the temperature variation during the phase change of PCM should be considered.

References

[1] S. P. Singh, Gary Burgess and Jay Singh. Performance Comparison of Thermal Insulated Packaging Boxes, Bags and Refrigerants for Single-parcel Shipments, *Packaging Technology and Science* ,Vol. 21, No. 2, pp. 25-35, 2007.

[2] Seung-Jin Choi and Gary Burgess. Practical Mathematical Model to Predict the Performance of Insulating Packages, *Packaging Technology and Science*, Vol. 20, pp. 369-380, 2007.

[3] Stavish, L. J. Designing Insulated Packaging for Perishable in vivo Diagnostics, *Medical Device and Diagnostic Industry*, Vol. 6, No. 18, pp. 105-108, 1984.

[4] Sanford cook. Thermo of Packaging, *Pharma /Device Packaging*, pp. 26-28, 1999.

[5] J. Qian. *Mathematical Models for Insulating Packages and Insulating Packaging Solutions*, Ph.D dissertation, Memphis, TN: The University of Memphis, 2010.

[6] X. J Guo and J. Qian. Spherical Shell Models for Insulating Packages Based on ANSYS. *Packaging Engineering*, Vol. 32, No. 5, pp. 43-48, 2011.

International Journal of Comprehensive Engineering
Part C, 2(1), 86-95, 2013
Doi: 10.14270/IJCE2013.2.1.c86
Regular paper

ISSN 2186-2680
e-ISSN 2186-2656
www.iace-journal.org

Development of a Kinetic Model for Predicting the Relative Humidity in Modified Atmosphere Packaging

Lixin Lu [1, 2, #], Jun Wang [1, 2], Hao Sun [1, 2]

[1] Department of Packaging Engineering, Jiangnan University, Wuxi, 214122, China;
[2] Key Laboratory of Food Packaging Techniques and Safety of China National Packaging Corporation, Wuxi, 214122, China

[#] Corresponding author: lulx@jiangnan.edu.cn; Tel.: +86-0510-82375036; Fax: +86-0510-82375036

Abstract: Adjusting and controlling the relative humidity (RH) inside package is crucial to ensuring the quality of modified atmosphere packaging (MAP) of fresh produce. In this paper, an improved kinetic model for predicting the RH in MAP was developed. The model was based on heat exchange and gases mass transport phenomena across the package, gases heat convection inside the package, and mass and heat balances accounting for the respiration and transpiration behavior of fresh produce. And then the model was applied to predict the RH in MAP of Fresh lentinula edodes (one kind of Chinese mushroom). A set of testing system was established to obtain the gas composition and relative humidity-temperature in MAP. Fresh lentinula edodes were packaged in different initial gas composition and sample mass, and stored for 40h at 8℃, 80% RH. The parameters of the respiration model for lentinula edodes were estimated, and the RH and temperature inside packages were measured during storage. The model equations were solved numerically using Adams-Moulton method to predict the RH in model packages. In general, the model predictions agreed well with the experimental data, except the model predictions were slightly high in the initial period. The effect of the initial gas composition on the RH in packages was notable. In MAP of lower oxygen and higher carbon dioxide concentration, the ascending rate of the RH was reduced, and the RH inside packages were saturated slowly during storage. The influence of the initial gas composition on the temperature inside package was not much notable.

Keywords: Fresh Produce, MAP, RH, Model, Respiration, Transpiration, Lentinula Edodes.

Received: May 20,2012/ Accepted: Nov. 6,2012 / Published: Apr. 8,2013

1. Introduction

MAP is an important technology which can efficiently maintain quality and extend shelf life of produce. However, most polymeric films used in MAP have lower water vapor permeation rates relative to larger respiration rates of fresh produce, excessively high RH inside package may occur, and it may lead to undesirable results such as moisture condensation, microbial growth, and shortened shelf life [1-4]. Some methods were adopted to reduce the RH inside the package for extending shelf life of produce [5-8].

Research on the mechanism of the RH change in MAP is very important for proper control of the RH and the quality of fresh produce. The RH in MAP is influenced by many factors such as respiration and transpiration of produce, the permeability of the packaging films, storage conditions, and packaging technology. Because of the RH inside the package with dynamic changes during storage, and the difficulty to accurately determine the respiration and transpiration process, little work has been done on predicting the RH in MAP.

It is critical to establish the kinetic model of produce respiration and transpiration in order to predict and control the change of the RH in MAP. Transpiration rate model in MAP system has not been well developed mostly because transpiration phenomena on product surface due to respiratory heat has not been well acknowledged at changing O_2 and CO_2 environment[9]. A model was developed predict the change of temperature and RH in MAP containing blueberry and moisture absorbent [9-10]. A simple model to predict the quality

changes of apples inside the packages was proposed [11]. Some effect factors and kinetic processes were neglected in above models, such as the temperature difference of the fresh produce, the package headspace and the surrounding, gases heat convection inside the package, and heat change caused by gas transmission across the package.

In MAP of non-respiring foods, several mathematical models for gas diffusion and sorption processes, and predicting the temperature change inside package were developed. Simpson proposed a model for gas diffusion and gas sorption processes [12], and then developed a model to predict consequences of temperature abuse on shelf life of pacific hake packaged in a MAP system [13] The model included simultaneous heat and mass transfer phenomena coupled with a predictive shelf-life model, and was solved using an explicit finite difference scheme. Simulated results were in good agreement with experimental results. Recently, these predictive models were successfully applied to study and determine the optimal conditions for packaging scallops in a modified atmosphere system [14].

In this study, an improved kinetic model for predicting the RH in MAP of produce was developed. The model was based on heat exchange and gases mass transport phenomena across the package, gases heat convection inside the package, and mass and heat balances accounting for the respiration and transpiration behavior of fresh produce. To verify the model, a set of testing system was established to measure the gas concentrations, RH, and temperature in MAP. The RH and temperature was valuated with experimental data of Fresh lentinula edodes (one kind of Chinese mushroom) packaged in modified atmospheres.

2. The Improved Kinetic Model for Predicting the RH in Map of Produce

Produce released respiratory energy during respiration In MAP. When releasing, respiratory heat partly is absorbed by produce leading to the rising itself temperature and part of heat is absorbed by free water of produce to vaporize water vapor. Meanwhile, the rest of respiratory heat releases to package.

According to law of heat conservation, a heat balance relation inside package can be represented as

$$Q_r = Q_p + Q_t + Q_g + Q_f + Q_e \tag{1}$$

where， Q_r is the respiratory heat of produce ($J \cdot h^{-1}$), Q_p is the heat absorbed by produce ($J \cdot h^{-1}$), Q_t is the heat absorbed by water vapor during evaporation ($J \cdot h^{-1}$), Q_g is the heat absorbed by gas inside package ($J \cdot h^{-1}$), Q_f is the heat absorbed by package ($J \cdot h^{-1}$), Q_e is the heat change caused by gas transmission across package ($J \cdot h^{-1}$).

2.1 Respiratory Heat of Produce

Considering the respiration heat of produce is the only internal heat, it could be described using the following respiratory equation [9]

$$C_6H_{12}O_6 + 6O_2 \rightarrow 6CO_2 + H_2O + 2816kJ \tag{2}$$

Respiration rate is generally described as O_2 consumption rate R_{O_2} or CO_2 evolution rate R_{CO_2}. Respiration rate of produce could be estimated using Michaelis-Menten type equations [15]

$$R_{O_2} = \frac{V_{m1}[O_2]}{K_{m1} + (1 + [CO_2]/K_{u1})[O_2]} \tag{3a}$$

$$R_{CO_2} = \frac{V_{m2}[O_2]}{K_{m2} + (1 + [CO_2]/K_{u2})[O_2]} \tag{3b}$$

where， R_{O_2} , R_{CO_2} are O_2 consumption rate , CO_2 evolution rate respectively ($ml \cdot kg \cdot h^{-1}$) , $[O_2]$, $[CO_2]$ are O_2, CO_2 concentration inside package respectively (%), V_{m1} ,V_{m2} are maximum O_2, CO_2 consumption rate

respectively ($ml \cdot kg \cdot h^{-1}$), K_{m1} , K_{m2} are Michaelis constants of O_2, CO_2 consumption respectively(%), k_{u1} , k_{u2} are inhibition constants in O_2, CO_2 consumption respectively(%).

The quantities of O_2 and CO_2 inside package are dynamic changeable in storage. On the basis of gas mass balance across the package, the change of O_2, CO_2 concentration inside package can be obtained [16]

$$\frac{d[O_2]}{dt} = (100)[\frac{P_{o_2} \cdot A_p \cdot p_{atm}(\frac{[O_2]_{out}}{100} - \frac{[O_2]_{in}}{100})}{z} - Ro_2 \cdot W_p]/V \tag{4}$$

$$\frac{d[CO_2]}{dt} = (100)[\frac{P_{co_2} \cdot A_p \cdot p_{atm}(\frac{[CO_2]_{out}}{100} - \frac{[CO_2]_{in}}{100})}{z} + Ro_{C2} \cdot W_p]/V \tag{5}$$

where， P_{O_2}, P_{CO_2} are film permeabilities to O_2, CO_2 respectively ($ml \cdot m \cdot m^{-2} \cdot h^{-1} \cdot atm^{-1}$), A_p is surface area of package (m^2), z is the thickness of package film (m), W_p is the mass of produce (kg), p_{atm} is the pressure of 1 atm , V is the free volume of package (ml).

Many researches indicate that respiratory quotient RQ （ R_{CO_2} / R_{O_2} ） changes between 0.7 to1.3. Therefore, respiration rates R of produce can be described by the average of O_2 consumption and CO_2 evolution rate [9, 11]

$$R = \frac{R_{CO_2} + R_{O_2}}{2} \tag{6}$$

Based on equation (2) - (6), the respiratory heat of produce in unit time can be represented as [9, 11]

$$Q_r = (\frac{2816}{6})RW_p \tag{7}$$

2.2 Heat Absorbed by Produce

The heat absorbed by produce results in the change of temperature of produce. The mass of produce may decrease because of evaporation. Considering it is insignificant to the initial mass of produce, the loss of mass is negligible in this study. So the heat absorbed by produce in unit time can be represented as [17]

$$Q_p = C_p W_p \frac{dT_p}{dt} \tag{8}$$

Where, C_p is the specific heat of surface tissue of produce ($J \cdot kg^{-1} \cdot k^{-1}$), T_p is the temperature on produce surface (k).

2.3 Heat absorbed by water vapor during evaporation

It is known that the heat absorbed by free water of unit mass to vaporize is definite in a certain condition. In unit time, the heat absorbed by water vapor during evaporation is (Song 2002, Kang 1989)

$$Q_t = L_m \lambda \tag{9}$$

Where, L_m is the rate of water evaporation from produce to package ($kg \cdot h^{-1}$), λ is coefficient of evaporation heat ($J \cdot kg^{-1}$).

2.4 The heat absorbed by gas inside package

The heat absorbed by gas inside package consists of the following processes:

(1) Gas around produce inside package absorbs heat and results in rise in temperature.

(2) The difference in temperature of gas between near and far away from the produce makes convection of gas inside package and result in exchange of heat.

2.4.1 Heat Absorbed by Gas Around the Produce

The heat absorbed by gas around the produce in unit time is expressed by [17]

$$Q_{g1} = W_s C_s \frac{dT_s}{dt} \tag{10}$$

Where, W_s is the mass of gas around the produce (kg), C_s is the specific heat of gas ($J \cdot kg^{-1} \cdot k^{-1}$), T_s is the temperature of gas around produce (k).

2.4.2 Heat Exchanged by Convection of Gas Inside Package

In the closed container, convection is natural heat releasing convection caused by the difference in temperature between gas near produce surface and free space inside package. Hence, Nusselt and Grashof rules could be used to describe the process.

It is well known that Nusselt number Nu is the function of Grashof number Gr and Prandtl number $\Pr$ on the condition of natural heat-releasing convection. To simpler geometric shapes, the following equations could be applied to deal with this problem in engineering [17]

$$Nu = \frac{HL}{k} = c(Gr_L \cdot \Pr)^m \tag{11}$$

Where, H is the coefficient of heat-exchange convection ($J \cdot h^{-1} \cdot m \cdot k^{-2}$), L is the qualitative length of Grashof number (m), k is the coefficient of heat-conduction of gas ($J \cdot h^{-1} \cdot m \cdot k^{-1}$), c is the proportion constant, Gr_L is the Grashof number when the qualitative length equals L, the value of exponent m, according to experience, is 1/4 for laminar flow and 1/2 for overfall flow[17].

To simplify analysis, a series of experimental formulas have been proposed. For example, on the condition of the natural convection inside the vertical or horizontal closed cylinder， Nu can be expressed as [17]

$$Nu \equiv \frac{HD}{k} = 0.55 \cdot (Gr_L \cdot \Pr)^{1/4} \tag{12}$$

Where, D is the diameter of cylinder (m).

The coefficients of heat-exchanging convection H can be obtained from equation (11)

$$H = \frac{ck(Gr_L \cdot \Pr)^m}{L} \tag{13}$$

Therefore, the exchanged convective heat in unit time can be expressed as

$$Q_{g2} = HA(T_s - T_h) \tag{14}$$

Where, T_h is the temperature far away form the heat-releasing surface (k), namely the temperature of headspace gas inside package.

As a result, in unit time, the heat absorbed by gas inside package is written as

$$Q_g = Q_{g1} + Q_{g2} \tag{15}$$

2.5 Heat Absorbed by Package

The heat absorbed by package is caused by the heat transfer produced by the difference in temperatures between inside and outside of the package. To rigid package, it consists of the packaging bracket and sealed film, while the container is made up of films to soft package. For universality, rigid package is discussed in this study.

The heat absorbed by a rigid package in unit time can be represented as

$$Q_f = Q_{ft} + Q_{fm} = W_t C_t \frac{dT_t}{dt} + W_m C_m \frac{dT_m}{dt} \tag{16}$$

Where, Q_{ft}, Q_{fm} is he heat absorbed by packaging bracket, sealed film respectively ($J \cdot h^{-1}$), W_t, W_m is the mass of bracket, package film respectively (kg), C_t, C_m is the specific heat of bracket' material, sealed film respectively ($J \cdot kg^{-1} \cdot k^{-1}$), T_t, T_m is the temperature of bracket, sealed film respectively (k).

2.6 Heat Change Caused by Ggas Transmission Across the Package

Gas exchanges are existed across the packaging film because of the difference of gas pressures inside and outside package during storage. It results in the heat change inside package.

The gas energy is the sum of the internal energy and pressure static energy [18]. The internal energy of perfect gas, determined only by temperature, is produced by heat movement of gas molecules. Average movement energy $\mathrm{E_k}$ of single gas molecule has a direct ratio relationship with absolute temperature [18].

$$\mathrm{E_k} = \frac{i}{2} k_B T = \frac{i}{2} n \cdot R_c \cdot T \tag{17}$$

where, i is the free degree of gas molecule, k_B is Boltzmann constant ($1.38 \times 10^{-23} J \cdot k^{-1}$), R_c is gas constant ($8.314 J \cdot mol^{-1} \cdot k^{-1}$), T is the absolute temperature of gas (k), n is the mol number of gas (mol).

The pressure static energy $\mathrm{E_s}$ of gas can be described as [18]

$$E_s = n R_c T \tag{18}$$

The free degrees of CO_2, H_2O, O_2 molecule are 6, 12, 5 respectively [18]. Generally, the gas environment in MAP contains lower O_2 concentration, higher CO_2 and water vapor concentration relative to those of outside package. The energy which CO_2 and water vapor permeate out package in unit time can be describes as

$$\begin{aligned} Q_{g-out} &= (\frac{dn_{CO_2}}{dt} \times \frac{6}{2} + \frac{dn_{H_2O}}{dt} \times \frac{12}{2})\ \mathrm{R_c} T_h + (\frac{dn_{CO_2}}{dt} + \frac{dn_{H_2O}}{dt}) R_c T_h \\ &= (4\frac{dn_{CO_2}}{dt} + 7\frac{dn_{H_2O}}{dt}) R_c T_h \end{aligned} \tag{19}$$

where, n_{CO_2}, n_{H_2O} are the mol number of CO_2, water vapor permeating out package respectively.

Meanwhile, the energy which O_2 permeates into package in unit time can be denoted as

$$Q_{g-in} = \frac{7}{2} \frac{dn_{O_2}}{dt} R_c T_{out} \tag{20}$$

where, n_{O_2} is the mol number of O_2 permeating into package, T_{out} is storage temperature of package (k).

The heat change caused by gas transmission across the package is

$$Q_e = Q_{g-in} - Q_{g-out} \tag{21}$$

In terms of the results above, the heat balance relation in MAP can be represented as

$$RW_p(\frac{Q}{6}) = W_pC_p\frac{dT_p}{dt} + L_m\lambda + HA(T_s - T_h) + W_sC_s\frac{dT_s}{dt} + W_tC_t\frac{dT_t}{dt}$$

$$+ W_mC_m\frac{dT_m}{dt} + \frac{7}{2}\frac{dn_{O_2}}{dt}R_cT_{out} - (4\frac{dn_{CO_2}}{dt} + 7\frac{dn_{H_2O}}{dt})R_cT_h \quad (22)$$

2.7 Predicting the RH in MAP

There are two sources that cause the change of quantity of water vapor inside package:

(1) The mass of water vapor produced by transpiration of produce.

(2) The mass of water vapor penetrated out or into packages across the package film.

2.7.1 The Mass Change of Water Vapor Caused by Transpiration of Produce

The mass of water vapor produced by transpiration of produce in unit time, namely transpiration rate of water vapor, can be obtained according to equation (22) as follows:

$$L_m = [\frac{Q}{6}RW_p - W_pC_p\frac{dT_p}{dt} - HA(T_s - T_h) - W_sC_s\frac{dT_s}{dt} - W_tC_t\frac{dT_t}{dt}$$
$$- W_mC_m\frac{dT_m}{dt} - \frac{7}{2}\frac{dn_{O_2}}{dt}R_cT_{out} + (4\frac{dn_{CO_2}}{dt} + 7\frac{dn_{H_2O}}{dt})R_cT_h]/\lambda \quad (23)$$

2.7.2 The Mass Change of Water Vapor Penetrated Out or Into Packages Across the Package Film

The mass of water vapor permeating across the package in unit time is represented as [9]

$$\frac{dm_{H_2O}}{dt} = [\frac{P_{H_2O}\cdot A_p\cdot(p_{H_2O}^{out} - p_{H_2O}^{in})}{z}][\frac{0.018\,p_{atm}}{R_cT_h}] \quad (24)$$

where, m_{H_2O} is the mass of water vapor (kg), P_{H_2O} is the package film permeability to water vapor ($ml\cdot m\cdot m^{-2}\cdot h^{-1}\cdot atm^{-1}$), $p_{H_2O}^{out}$, $p_{H_2O}^{in}$ are the water vapor pressures outside and inside package respectively (atm).

2.7.3 The Change of the RH Inside Package

The changing rate of mass of water vapor inside the package, can be described as

$$\frac{dH_{in}}{dt} = \frac{L_m - \frac{dm_{H_2O}}{dt}}{W_a} \quad (25)$$

Where, H_{in} is the absolute humidity inside package ($(kg\cdot H_2O)\cdot(kg^{-1}\cdot dry\cdot H_2O)$), W_a is the mass of dry air inside package (kg).

The RH inside package can be denoted as:

$$RH_{in} = \frac{H_{in}}{H_{sp}} \quad (26)$$

Where, H_{sp} is the absolute humidity of saturated water vapor at corresponding temperature ($(kg\cdot H_2O)\cdot(kg^{-1}\cdot dry\cdot H_2O)$).

3. Predicting the RH in Map of Lentinula Edodes

3.1 Materials and Method

3.1.1 Fresh Lentinula Edodes and Packaging Film

Field-grown lentinula edodes used in this study was grown in Wuxi, China and harvested at the stage of maturity in March, 2008. Lentinula edodes were then transported to the laboratory within one hour. They were selected for similar in size and regular in shape.

The low-density polyethylene, 32μm thick (LDPE) (Shenda Flexible Packaging Material Co., Ltd.,China) was used for packaging film. The film permeabilities to O_2, CO_2 and H_2O were measured by gas permeability testers (Languang Instrument Ltd., China, Model BTY-B1,TSY-T, Test precision: 5%) under 8℃. The film permeabilities to O_2, CO_2, H_2O are 5.66×10^{-13} , 16.12×10^{-13} , 4.32×10^{-14} $ml\cdot m\cdot m^{-2}\cdot h^{-1}\cdot atm^{-1}$ respectively.

3.1.2 Testing System

Shown as Fig.1, the testing system consisted of four parts that were testing jar, intelligent measurement system of RH-temperature, adjustment system of RH-temperature and gas concentration analysis system. In order to measure the temperature, RH and gas concentrations inside the metal jar, one RH-temperature sensor (RH:10-100±2.0%, temperature:0-60±0.5℃) and one gas pump were fixed on the upper portion of the jar, and connected to intelligent measurement instrument of RH-temperature and gas concentration analysis instrument (Illinois Ltd, U.S.A., Model 6600, O_2 range: 0.001-100±0.2%, CO_2 range: 0.1-100±2.0%） respectively.

The testing jar can be closed with metal cap or packaging film in order to conduct the airtight or permeability packaging testing. After packaging, the testing jars were placed in adjuster of relative humidity-temperature (Qingshen Ltd, Taiwan, Model THS-D7C-100AS, temperature: 0-100±0.5℃，RH:20-100±2.0%) to be stored in a testing condition.

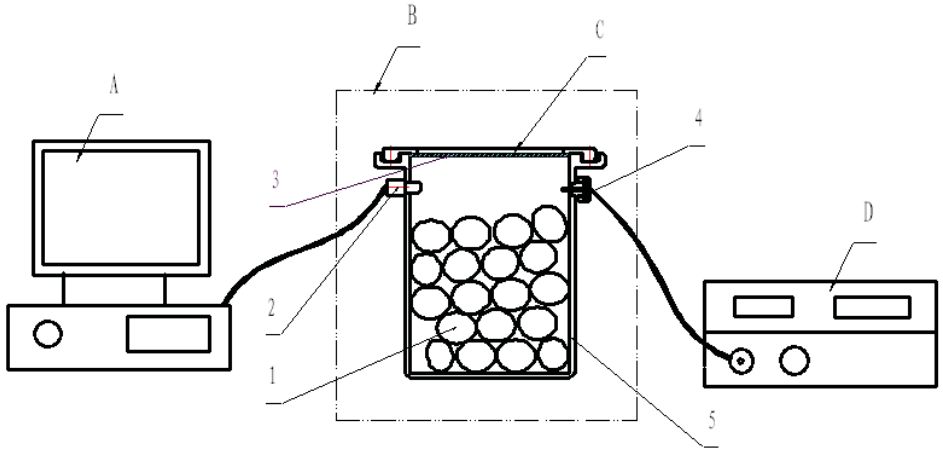

Fig. 1 Schematic of testing system (A, intelligent measurement system of RH-temperature ; B, adjust system of RH-temperature; C, testing jar; D, gas concentration analysis instrument; 1. samples; 2. sensor of RH-temperature; 3. sealed film/metal cap; 4. pump of gases; 5. jar body)

3.1.3 Estimation of respiration model parameter values

The samples and the jars were pretreated at 8℃, 80%RH for 4h. The normal air packages were applied to pack 570±10g of samples using testing jars, which were closed with metal caps. The packages were stored at 8℃, 80%RH for 48h. The concentrations of O_2 and CO_2 were measured every 2h. The parameter values of respiration rates were calculated according to closed system method [15]. The experiment was simultaneously repeated three times.

Respiration rate data from above experiments were to estimation of respiration model parameters values. Equation (3) was linearized as Equation (27) for the purpose of fitting the data [15]

$$\frac{1}{R_{O_2}}=\frac{1}{V_{m1}}+\frac{K_{m1}}{V_{m1}}\frac{1}{[O_2]}+\frac{1}{K_{u1}V_{m1}}[CO_2] \tag{27a}$$

$$\frac{1}{R_{CO_2}}=\frac{1}{V_{m2}}+\frac{K_{m2}}{V_{m2}}\frac{1}{[O_2]}+\frac{1}{K_{u2}V_{m2}}[CO_2] \tag{27b}$$

The multiple linear regression analysis for estimating the parameter values of respiration model was performed using the statistical software SAS.

3.1.2 Packaging and storage of the samples

First, normal air packages were applied to pack 480 ± 10, 700 ± 10 g of samples using test jars, which were closed with LDPE films of constant area 0.177m^2.

In the second test, modified initial gas composition (3.5%O_2/11.0%CO_2/85.5%N_2) packages were applied to pack 700±10g of samples using testing jars. Gas mixtures were conducted using a gas mix machine (Desen Packaging Machine Ltd., China, Model MA-35, CO_2, O_2, N_2 range: 0-90±1%). The machine used cylinders of compressed oxygen, carbon dioxide, and nitrogen to prepare the gas mixtures of any required proportions of oxygen, carbon dioxide, and nitrogen. Before packaged, the testing jars were flushed with the required gas composition (initial RH: 31%, temperature: 8℃) for five minutes through the lower valve of the jars, and then the samples were placed in jars. In the meantime, the flush was kept; finally the jars were closed with LDPE films.

The samples, testing jars were conditioned at 8℃, 80%RH for 4h before packaged. The packaging operation was conducted in a cold room at 8℃. All packages were stored at 8℃, 80% RH for 40h, with periodic sampling to measure the RH and temperature. Three replicates were used for each condition.

3.2 Model Simplification and Numerical Analysis

3.2.1 Simplification of the Kinetic Model

In terms of the above experiment conditions, the kinetic model can be simplified as following:

(1) Since the headspace of package is small, thermal equilibrium between the produce and the headspace is assumed to reach within a short time. Consequently the heat caused by gas convection inside package could be neglected, and the heat absorbed by gas inside the package in unit time can be simplified as [17]

$$Q_g = W_a C_a \frac{dT_{in}}{dt} \tag{28}$$

where, C_a is the specific heat of dry air inside the package ($J \cdot kg^{-1} \cdot k^{-1}$), T_{in} is the temperature of gas inside the package (k).

(2) Usually the temperature change inside package of produce is not notable [9]; its effect on the permeability of packaging film and the respiration model parameters can be ignored.

3.2.1 Numerical analysis

Based on the experimental conditions and corresponding parameters, the numerical analysis of the simplified kinetic model and corresponding equations was conducted using the Adams-Moulton method to obtain the change of RH inside package.

3.3 Results and Discussion

3.3.1 Respiration Model Parameter Values of Lentinula Edodes

The respiration rate data obtained from the closed system experiments were applied to fit equation (27). The estimated parameter values were presented in Table 1. The regression equation fitted the data well with the coefficient of determination $R^2 > 0.95$.

Table 1 Parameter estimates of respiration model for lentinula edodes at 8℃

Gas	V_m ($ml \cdot kg^{-1} \cdot h^{-1}$)	K_m (%)	K_u (%)	R^2
O_2	122.52	26.73	-88.30	0.9824
CO_2	110.81	30.11	-83.23	0.9575

3.3.2 Verification of the Kinetic Model

The model predictions were compared to the results of three sets of experiments. The experiments varied in product weight and initial gas composition.

Fig.2 and Fig.3 compared the model predictions and experiment data for 480,700g lentinula edodes and normal air packages respectively. The results showed that the RH inside packages rose rapidly. In the packages with the masses of 480, 700g, the RH inside packages reached saturation (100%RH) 12h, 10h later respectively. The main reason was that the gas exchange inside and outside the package was slow because of the initial gas of air and the respiration and transpiration rates were a bit higher. As the mass of produce increased, the quality of

vaporized moisture enhanced, the headspace decreased, and the rising rate of the RH quickened. Meanwhile the results showed good agreement between theoretical prediction and experimental results with a little higher theoretical result at the beginning of package and the time for RH to reach saturated state shortened about 1h mainly because of the simplification in theoretical analysis and neglects of influences of some factors on energy changes.

Fig.4 compared the model prediction and experiment data for 700g lentinula edodes and modified initial gas composition packages. Comparing with the package of same mass with initial gas of air, the increasing rate of the RH inside package was slowed down greatly. About 22h later, the RH reached saturation. The main reason is that modified atmosphere of low CO_2 and high O_2 decreased the respiration rates of produce and furthermore the transpiration rates were slowed down. This shows that initial gas composition could influence the RH inside package evidently. Similarly, the theoretical prediction agreed well with the experimental results.

The temperature change in three experimental conditions was shown in Fig.5. As a whole, the change of temperature inside packages was not much notable. During storage of 40h, corresponding to the experimental condition, the highest temperatures inside packages rose approximately 3.3℃, 4.3℃, 2.0℃ respectively. Meanwhile temperature inside packages decreased a little along with the prolonging of storage. This situation showed the respiratory heat of sample was mainly absorbed to vaporize water vapor and result in the RH inside packages rose rapidly. The slightly increase temperatures justified our simplification of the kinetic model.

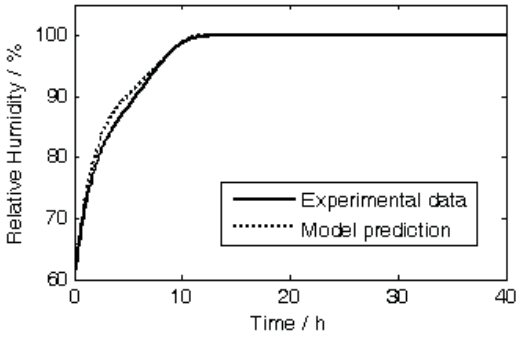

Fig. 2 Relative humidity in packages of lentinula edodes during storage (mass: 480g; initial gas composition:normal air)

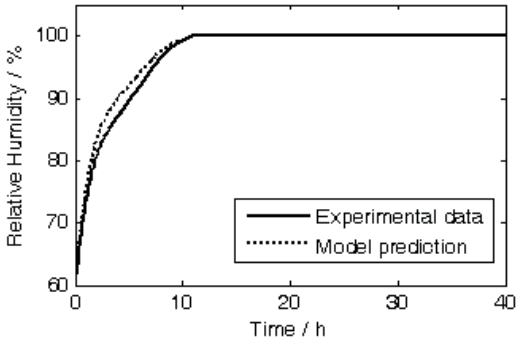

Fig.3 Relative humidity in packages of lentinula edodes during storage (mass: 700g; initial gas composition: normal air)

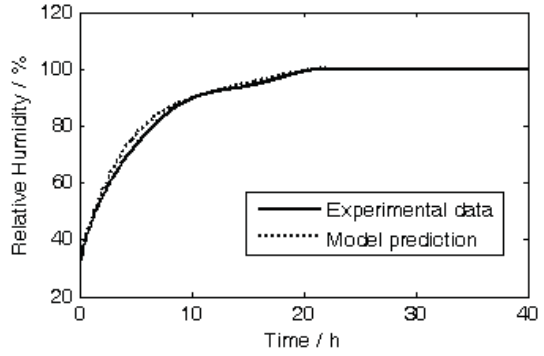

Fig.4 Relative humidity in packages of lentinula Edodes during storage (mass: 700g; initial gas composition: 3.5%O2/11.0%CO2/85.5%N2)

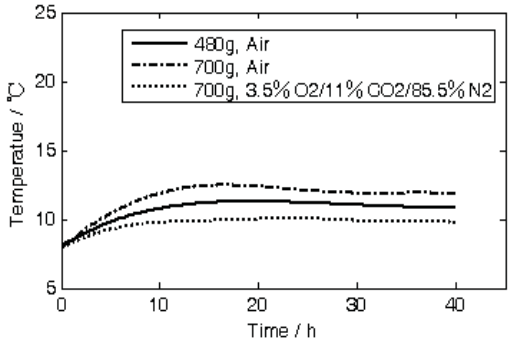

Fig. 5 Temperature in packages of lentinula edodes during storage

4. Conclusions

An improved kinetic model was developed to predict the RH in MAP of produce based on heat exchange and gases mass transport phenomena across the package, gases heat convection inside the package, and mass and heat balances accounting for the respiration and transpiration behavior of fresh produce. The experiments of MAP containing Fresh lentinula edodes were conducted to obtain the RH and temperature inside packages. The results showed that:

(1)As a whole, the model predictions agreed well with experimental results.

(2)Initial gas composition had notable influence on the RH inside packages.

(3)The change of temperature inside package and effect of initial gas composition on temperature were not much notable.

Acknowledgment

This work was supported by Ministry of Science and Technology and Ministry of Eduaction of the People's Republic of China, Innovation and Technology Fund of Jiangnan University.

References

[1] Lu L X. Theoretical Research Advances on Modified Atmosphere Packaging of Fruits and Vegetables, *Transactions of the CSAE*, Vol. 7, pp. 175-180, 2005.

[2] Kader AA , Zagory D and Kerbel EL. Modified Atmosphere Packaging of Fruits and Vegetables, *Critical Reviews in Food Science & Nutrition*, Vol. 28, No.1, pp.1-30, 1989.

[3] Deepak RR, Harinder SO and Bangali B. Modified Atmosphere Packaging and Its Effect on Quality and Shelf Life of Fruits and Vegetables-An Overview, *Journal of Food Science & Technology*, Vol. 39, No. 3, pp. 199-207, 2002.

[4] Cai M and Lu LX. Research on the Variation of Temperature and Humidity in Modified Atmosphere Packaging of Strawberry, *Packaging Engineering*, Vol. 26, No. 4, pp. 32-33, 2005.

[5] Villaescusa R and Gil MI. Quality Improvement of Pleurotus Mushroom by Modified Atmosphere Packaging and Moisture Absorbers, *Postharvest Biology & Technology*, Vol. 28, No. 1, pp. 169-179, 2003.

[6] Lee DS, Kang JS and Renault P. Dynamic of Internal Atmosphere and Humidity in Perforated Packages of Peeled Garlic Cloves, *International Journal of Food Science & Technology*, Vol. 35, No. 5, pp. 455-464, 2000.

[7] Varoquaux P and Gouble B. Films with Adjustable Permeability for Preservation of Fresh Fruit and Vegetable, *Industries Alimentaires et Agricoles*, Vol. 114, No. 3, pp. 133-136, 1997.

[8] Evelo RG and Horst J. Modified Atmosphere Packaging of Tomatoes: Controlling Gas and Humidity, *Packaging Technology & Science*, Vol. 9, No. 5, pp. 265-273, 1996.

[9] Song Y, Nick V and Yam K L. Modeling Respiration-Transpiration in a Modified Atmosphere Packaging System Containing Blueberry, *Journal of Food Engineering*, Vol. 53, pp. 103-109, 2002.

[10] Song Y, Lee DS and Yam KL. Predicting Relative Humidity in Modified Atmosphere Packaging System Containing Blueberry and Moisture Absorbent, Journal of Food Processing & Preservation, Vol. 25, pp. 49-70, 2001.

[11] Kang J S and Lee D S. A Kinetic Model for Transpiration of Fresh Produce in a Controlled Atmosphere, *Journal of Food Engineering*, Vol. 35, pp. 65-73, 1998.

[12] Simpson R, Almonacid S and Acevedo C. Development of a Mathematical Model for Map Systems Applied to Nonrespiring Foods, *Journal of Food Science*, Vol. 66 , No. 4, pp. 561-567, 2001.

[13] Simpson R, Almonacid S, Acevedo C and Cortes C. Mathematical Model to Predict Effect of Temperature Abuse in Map Systems Applied to Pacific Hake (Merluccius Australis), *Journal of Food Process Engineering*, Vol. 26, No. 5, pp. 413-434, 2003.

[14] Simpson R, Carevic E and Rojas S. Modelling a Modified Atmosphere Packaging System for Fresh Scallops (Argopecten Purpuratus), *Packaging Technology &. Science*, Vol.20, pp. 87‐97, 2007.

[15] Lee DS, Haggar PE, Lee J and Yam KL. Model for Fresh Produce Respiration in Modified Atmospheres Based on Principles of Enzyme Kinetics, *Journal of Food Sceienc*, vol. 56, pp. 1580-1585, 1991.

[16] Hayakwa K, Hening YS and Gilbert SG. Formulae for Predicting Gas Exchange of Fresh Produce in Polymeric Film Package, *Journal of Food Science*, Vol. 40, pp. 186-191, 1975.

[17] Pitts DD and Sissom Le. *Theory of Conduct Heat*, Scientific Press, Beijing, 2002.

[18] Ma WW. *Physics*, Scientific Press, Beijing, 2002.

International Journal of Comprehensive Engineering
Part C, 2(1), 96-105, 2013
Doi: 10.14270/IJCE2013.2.1.c96
Regular paper

ISSN 2186-2680
e-ISSN 2186-2656
www.iace-journal.org

Technological Access to the Immerging Global Issues: Population, Food, Energy and Environment

Rodrigo Pechon [1], Ho Jinyama [2], Nobutaka Ito [3]

[1]Research Fellow, Department of Environmental Science and Engineering, Faculty of Bioresources, Mie University, Japan
[2]Professor, Department of Environmental Science and Engineering, Faculty of Bioresources, Mie University, Japan
[3]Visiting Professor, Faculty of Engineering Chiang Mai University, Thailand

Abstract: Industrial development and advance technology created an impact of the world ecosystem. It leads to a huge increase in fossil fuel consumption and CO_2 emissions that being responsible of the rise in global temperature over the past several decades. Climate change could be the most immerging problem and threats in the near future. Rapid warming climate could seriously create longer and more intense heat waves and extreme weather events (floods, storms, droughts). The main challenges is how to provide more energy and food to the increasing inhabitants at the same time reducing pollution and green house gas emission thereby security of mankind existence. This article presents data and projections that overseen on the immerging global issues.

Keywords: Carbon Dioxide Emission, Climate Change, Energy, Food, Population.

Received: May 31,2012 / Accepted: Nov. 6,2012 / Published: Apr. 8,2013

1. Background

Drastic increase of the world population in recent decade creates many issues and concerned that apparently needed attention. Some of the serious issues are the rapid population growth, excessive energy utilization, thereby producing huge amount of carbon dioxide (CO_2). Develop countries has the big role in solving this phenomenon. Over the next two – three decades, concern over possible climate change caused by greenhouse gas emissions, primarily CO_2 from fossil fuel combustion may fundamentally change energy industries and markets, environment, life, and living standards continues to increase along with modernization. A major curb in global greenhouse gas emission particularly CO_2 will affect the global economy. CO_2 can easily be found by the combustion of fossil energy resources. Conversion of fossil fuel to energy causes CO_2 to be released into the atmosphere, which in turn contributes to general warming of the globe. Reduction of carbon dioxide emissions to prevent global warming is now a worldwide problem and the COP3 conference on global warming focus on this problem [1]. It further proposed to allocate reduced acceptable amounts of carbon dioxide emissions to each country, especially to advanced countries. The problem be tentatively countered with measures to be undertaken and headed by the develop countries.

In this context, investigative research on the technological access to the immerging global issues was conducted. We provide an overview of the main global issues such as; population, food, energy and CO_2 emission, present the motivation for research in this field, and give emphasis and summary of the current state of knowledge.

2. Global population

Global population issues have received inadequate attention and very surprising at the beginning of the 21st century how few population geographers work on global issues [2]. In 1999, world population reached 6 billion

and was recorded as growing at 1.33% per annum [2, 3, 4]. The United Nation Population Division anticipates that by 2050 the total will have risen to 8.9 billion (medium variant projection). Table 1 indicates population of the world and its major areas. Record shows that these have often been used to support the view that a crisis will stem from trends in global population [5, 6, 2], global energy utilization, global food consumption. An estimated 78 million people are now added each year, compared with a record high of 86 million between 1985 and 1990 [2]. However, rates of population growth in Africa are the highest in the world, with a near-doubling over 1995 population levels projected by 2025, and close to a tripling likely by 2050 [7, 8].

Table 1 Population of the world and its major areas, 1750-2150

Major Area	*1750*	*1800*	*1850*	*1900*	*1950*	*1999*	*2050*	*2150*
			A. Population Size (millions)					
World	791	978	1 262	1 650	2 521	5 978	8 909	9 746
Africa	106	107	111	133	221	767	1 766	2 308
Asia	502	635	809	947	1 402	3 634	5 268	5 561
Europe	163	203	276	408	547	729	628	517
Latin America and the Caribbean	16	24	38	74	167	511	809	912
Northern America	2	7	26	82	172	307	392	398
Oceania	2	2	2	6	13	30	46	51
			B. Percentage distribution					
World	100	100	100	100	100	100	100	100
Africa	13.4	10.9	8.8	8.1	8.8	12.8	19.8	23.7
Asia	63.5	64.9	64.1	57.4	55.6	60.8	59.1	57.1
Europe	20.6	20.8	21.9	24.7	21.7	12.2	7.0	5.3
Latin America and Caribbean	2.0	2.5	3.0	4.5	6.6	8.5	9.1	9.4
North America	0.3	0.7	2.1	5.0	6.8	5.1	4.4	4.1
Oceania	0.3	0.2	0.2	0.4	0.5	0.5	0.5	0.5

In 2000, the United Nations estimated that the world's population was growing at an annual rate of 1.14% (or about 75 million people), down from a peak of 88 million per year in 1989. By 2000, there were ten times as many people on Earth as there were in 1700. According to data from the CIA's 2005–2006 World Factbooks, the world human population increased by an average of 203,800 people every day in the mid-2000s [9]. The CIA Factbook increased this to 211,090 people every day in 2007, and again to 220,980 people every day in 2009.

On October 31, 2011, a first baby born was counted as the 7 billionth. Amid the millions of births and deaths around the world each day, it is impossible to pinpoint the arrival of the globe's 7 billionth occupant. But the U.N. chose Monday to mark the day with festivities worldwide, and a series of symbolic 7 billionth babies being born.

Another transformation growth in the 20th century has been population ageing, in 1999 there were 593 million persons age 60 years or over in the world, comprising 10 percent of the total world population. By 2050, this figure will triple to nearly 2 billion older persons, comprising 22 percent of the world population. This massive changing age structure will have wide-range social and economic consequences, affecting such factor as economic growth, savings and investment, labor supply and employment, pension schemes, and health and long-term scheme. While once limited to develop countries, concern for the consequences of ageing has spread to developing countries.

China, meanwhile, having the most world populous nation reaching at 1.34 billion people, said it would stand by its one-child policy, a set of restrictions launched three decades ago limiting most urban families to one child and most rural families to two. "Overpopulation remains one of the major challenges to social and economic development," Li Bin, director of the State Population and Family Planning Commission, told the official Xinhua News Agency. He said the population of China would hit 1.45 billion in 2020 [10]. There won't be enough young Chinese to support its enormous elderly population. While India, with 1.2 billion people, is expected to overtake China around 2030 when the Indian population reaches an estimated 1.6 billion. It took

until 1804 for the world to reach its first billion people, and a century more until it hit two billion in 1927. The 20th century, though, saw things begin to cascade: three billion in 1959; four billion in 1974; five billion in 1987; six billion in 1998.

Total population has been steadily increasing but world agricultural population is minimal as shown in Fig. 1. An 11.03% increase in total population projection in 2010 - 2020 and 1.29% world agricultural populations. Asian agricultural population is higher than the rest of the group.

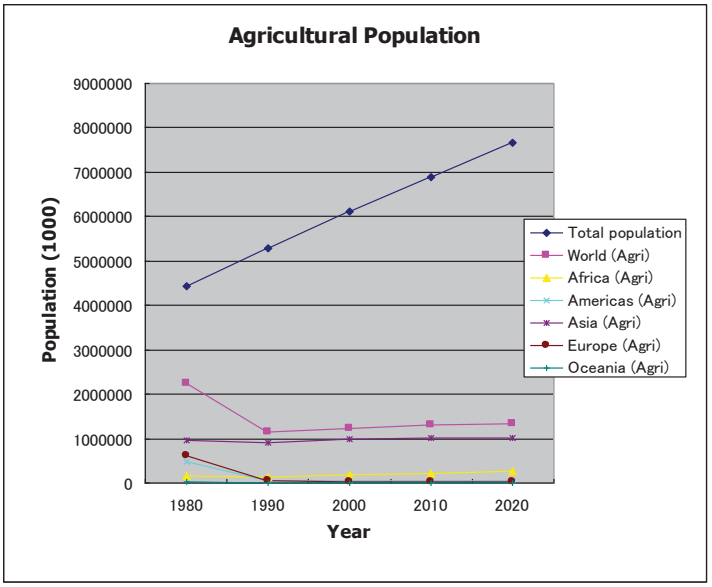

Fig. 1 World population in comparison with agricultural populationby geographical grouping, 1980-2020.

3. Global food

Food production in the developing countries would need to almost double. This implies significant increases in the production of several key commodities. For instance, annual cereal production would have to grow by one billion tons, meat production by over 200 million tons to a total of 470 million tons in 2050, 72 percent of which produced in developing countries, up from the 58 percent in 2009 [11]. Feeding the world population adequately would also mean producing the kind of foods that are lacking to ensure nutrition security.

Demand for cereals for both human food and animal feed uses are projected to reach some 3 billion tones by 2050. The advent of biofuels has the potential to change some of the projected trends and causes world demand to be higher, depending mainly on energy prices and government policies. The demand for other food products that more responsive to higher incomes in developing countries (such as livestock and dairy products, vegetable oil and others) will grow much faster than the cereals. Fig. 2 shows the cereal production by geographical grouping in 1970-2009. Mainly, Oceania is the leading producer of cereal followed by Europe. In 2009, Oceania contributed 53.09 percent of the total cereal production.

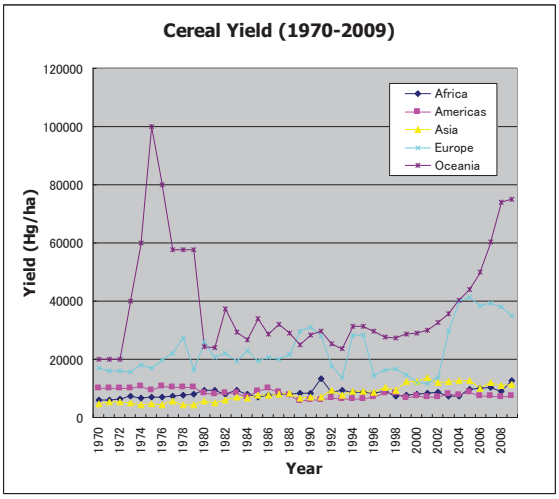

Fig. 2 World cereal yield by geographical grouping, 1970-2009

Regional Prospective defines wide difference both in agricultural production commodities and yields for major crops. Africa relies mainly on maize, Asia relies on rice and Americas (Northern, Central, South and Caribbean) and Europe relies on other cereals. Maize yields in Africa are generally low (fig. 3) and rate increase are also alarming in comparison to the other geographical grouping. This scenario should be taken care of and should be improved. Increasing those yields gave solutions of massive Africa's population growth. United Nation [8] and Population Reference Bureau [7] reported that rate of population in Africa is the highest in the world with a near double over 1995 and close to a triple by 2050. Africa would need to triple the yields by 2025 and pushed to quadruple them by 2050, assuming a 0.5 percent rate of per capita consumption growth to overcome nutritional insufficiency and a 1 percent rate annually of cultivated land expansion [12]. Thus, if not feasible the gap will have to be filled and solve by a massive increase in imports which many of the poorer African countries can ill afford.

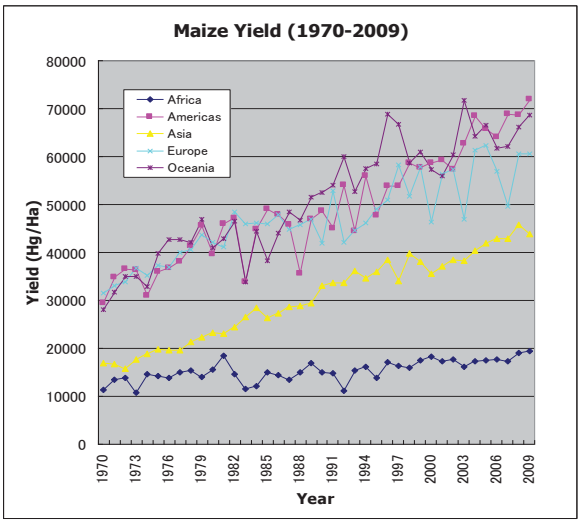

Fig. 3 World Maize yield by geographical grouping, 1970-2009

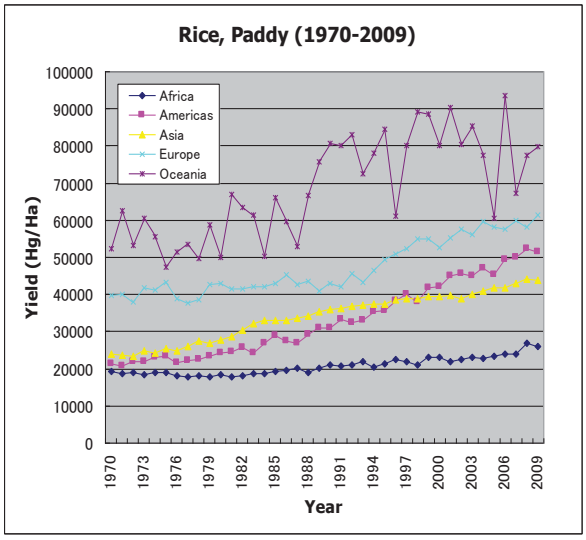

Fig. 4 World rice paddy yield by geographical grouping, 1970-2009

In tropical regions, high temperatures are the main constraint in rice production. Studies on rice productivity under global warming condition suggest that the yields and other crops decreases as the temperature increases. Climate change could bring about yield decrease between 10 to 36 percent and 10 to 30 percent of maize and sorghum respectively [13]. A yield decrease of 14.5 percent in summer crops in India using Hadley-coupled model [14]. The rice yield of dry season in the Philippines decreases by as much as 15 percent for each 1°C increase in the growing season mean temperature [15].Fig. 4 shows that Oceania is the leading rice producer by geographical grouping.

Temperature increase in subtropical and temperate areas may have a positive or negative effect on rice crops. Its increase would improve the crop establishment of rice in Mediterranean where cool weather usually causes

poor crop establishment [16]. On the other hand, an increase in temperature (16-21^{O}C) would reduce the beneficial effects on grain production of the low night temperature in Northern Japan [17].

4. Global energy

Global energy consumption increased 40 times between 1860 and 2005 to 435 Q/year, and is increasing by 1.5 percent yearly to reach 625 Q in 2025 [18, 19, 20]. Energy consumption of the United States is about 25 percent of the world's energy use, of which biofuels presently account for 3.5 Q/year [18]. The U.S. ethanol production was about 4 billion gallons in 2005, and the U.S. Energy Bill mandates a 3.5 billion gallons increase in the production by 2012 [21].

Numerous studies also addressed the role of global corporations in fostering climate change. They examine the global environmental practices of transnational corporations (TNCs) and their contribution to greenhouse gas emission [22, 23, 24]. Mason [22] focus on the emission patterns and environmental impact of TNC activity, focusing on the aluminum industry while Robbins [23] and UNCTC [24] found out that TNCs are major contributors to global emission of greenhouse gasses. Their studies provide important insights into the causes of climatic change. In addition, several studies have examined the effect of climate change on global agriculture trade, focusing mainly on the agricultural yield, commodity prices, and export and import for individual countries.

Climate changes will strike areas in developing countries mainly and elsewhere the most vulnerable regarding access to vital resources, food production, and economical development. The frequency of extreme meteorological events such as heat waves, floods, hurricanes, or even tsunami is predicted to be increasing in the future [25]. This phenomenon will affect greatly to our society. Developing countries is expected to bear the greatest losses from global warming, especially human life losses [26].

Renewable energy is usually defined as energy that comes from a resource that is naturally replenished. Renewable energy sources generally emit no or minimal greenhouse gas emissions. An estimate of about 16 percent of the global final energy consumption comes from renewable, with about 10 percent can be sourced out from traditional biomass, which is mainly used for heating, and about 3.4 percent from hydroelectricity. New renewable such as wind, solar, geothermal, small hydro and biofuels is accounted for 2.8 percent and are increasing very rapidly [27].

Some examples of renewable energy include:

a) Bioenergy (can be used in a number of ways to generate electricity, heat, or transport fuels from biological materials that store energy, such as wood, biogas, biofuel and others).

b) Geothermal energy (can be harnessed to generate electricity or provide direct heat). The thermal energy generated and stored in the Earth. Thermal energy is the energy that determines the temperatue of matter. Earth's geothermal energy originates from the original formation of the planet (20%) and from radioactive decay of minerals (80%) [28]. Geothermal power is cost effective, reliable, sustainable, and environmentally friendly [29].

c) Wind energy (which can be harnessed to drive wind turbines). The current primary strategy for wind is electricity generation. Wind energy is one of the fastest forms of electricity generation to build and bring online. It also has one of the lowest overall environmental impacts - using wind to generate electricity does not produce greenhouse emissions.

d) Hydro energy **(**generated from water flowing through turbines). Hydroelectricity produces no greenhouse gas emission in its operation, and the water stored in a dam can be turned into electricity. It is the electricity generated by hydropower, the production of electrical power through the use of the gravitational force of falling or flowing water.

e) Marine energy or ocean energy (such as wave, tidal, and ocean energy devices). The water movement in the world's oceans creates a vast store of kinetic energy, or energy in motion. This energy can be harnessed to generate electricity to power homes, transport and industries.

f) Solar energy (from the sun). Solar radiation is an abundant energy source which is free, non-polluting, and renewable. It can be used to generate electricity directly through photovoltaic panels which used semiconductor to generate electricity. Non-electrical storage systems permit direct solar heating of buildings and water. Storage has been combined with electricity generation in devices that use heated fluids to drive turbines and retain heat during periods of low sunshine.

Global renewable energy capacity grew at the rate of 10-60 percent annually for many technologies during the five-years of 2004 through 2009. For wind power and many others, growth accelerated in 2009 relative to the previous four years. More wind power capacities was added in 2009 than any other renewable technology [30].

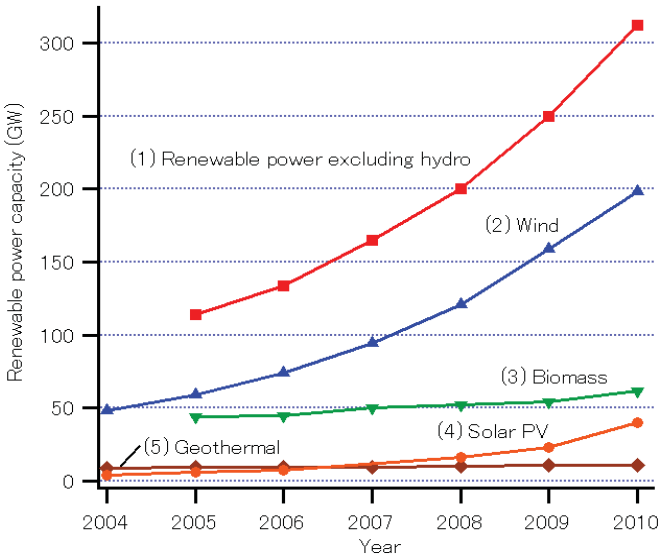

Fig. 5 Global renewable power capacities (excluding hydro)

An example of wind power utilization worldwide as shown in table 2, global wind power installation increases by 15,787 MW in June 2010. China is accounted 48.75 percent of the total installation. If the trend continues, China will surpass the US soon as expected.

Table 2 Wind Power Worldwide 2010

Ranking	Country	Total Capacity June 2010 [MW]	Added Capacity June 2010 [MW]	Total Capacity end 2009 [MW]
1	USA	36, 300	1, 200	35, 159
2	China	33, 800	7, 800	26, 010
3	Germany	26, 400	660	25, 777
4	Spain	19, 500	400	19, 149
5.	India	12, 100	1, 200	10, 925
6	Italy	5, 300	450	4, 850
7	France	5, 000	500	4, 521
8	UK	4, 600	500	4, 092
9	Portugal	3, 800	230	3, 535
10	Denmark	3, 700	190	3, 497
	Rest of the World	25, 500	2, 870	21, 698
Total		175, 000	16, 000	159, 213

5. Environment

Man-made sources of carbon dioxide include the burning of fossil fuels for heating, power generation and transport, as well as some industrial processes. Burning fossil fuels such as coal and petroleum is the leading cause of increased anthropogenic CO_2; deforestation is the second major cause. In 2008, 8.67 gigatons of carbon (31.8 gigatons of CO_2) were released from fossil fuels worldwide, compared to 6.14 gigatons in 1990 [31]. In 1751 to 1900 about 12 gigatons of carbon were released as a carbon dioxide to the atmosphere from burning of fossil fuels, whereas from 1901 to 2008 the Fig. was about 334 gigatons.

Other sources of CO_2 emission are natural. For example, the natural decay of organic material in forest and grasslands. Although the initial carbon dioxide in the atmosphere of the young earth was produced by volcanic activity, modern volcanic activity releases only 130 to 230 megatons of carbon dioxide each year [32], which is less than 1% of the amount released by human activities.

Global warming of the earth also created by releasing chemical substances into the environment, like global acidification and the growing hole in the ozone layer as shown in Fig. 6.

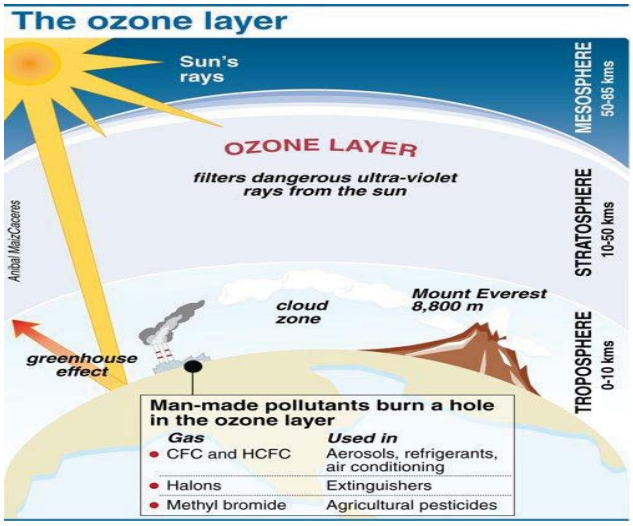

Fig. 6 A fact file shows how manmade pollutant affects ozone layer.

Ozone depletion describes two distinct but related phenomena observed since the late 1970's: a steady decline of about 4% per decade in the total volume of ozone in Earth's stratosphere (the ozone layer), and a much larger springtime decrease in stratostopheric ozone over Earth's polar regions. The greatest declines is almost 30% that occurs during winter and spring, when the stratospher is colder and temperature is lower [33]. Ozone depletion also explain much of the observed reduction in tratospheric and upper tropospheric temperatures [34]. The source of the warmth of the stratosphere is the absorptio of UV radiation by the ozone, hence reduced ozone leads to cooling. Some stratospheric cooling is also predicted from increases in greenhouse gases such as CO_2; however the ozone induced cooling appears to be dominant.

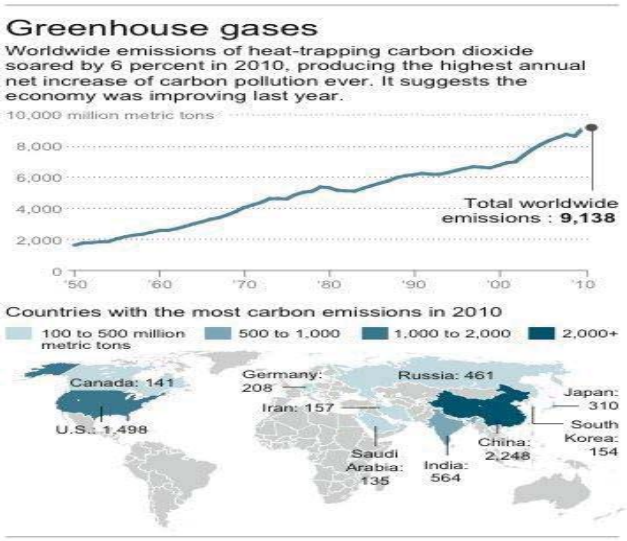

Fig. 7 Map shows 10 countries with most carbon emission in 2010 and last 50 years of world emission

Ecological modernization prospective suggests that the best way to solve environmental problems such as CO_2 emissions is through more economic development [35]. Carbon dioxide emissions are lowest in countries with the lowest and highest levels of economic development [36, 37]. New Zealand as an example uses about 3.4 billion liters of petrol and about 2.9 billion liters of diesel yearly. There energy strategy call for a 50% reduction of transport carbon emissions per capita by 2040 [38]. The legislation however stated that by 2012 only 3.4% of the energy content of transport fuels must be through biofuels with a slow ramp up from a mandatory ~0.53% from the middle of 2008. It is likely that 2050 goal will only be met by embracing a variety of emerging technologies. Furthermore, Packer [39] found out that worldwide aviation industries is a significant contributor of global CO_2 emissions (~2.0% of total global emission). Significant progress has been made also in demonstrating the impact of the hybrid gasoline-electric vehicles. These alternative vehicles will be essential in reducing worldwide CO_2 emissions from car and long-haul vehicles. Brazil on the other hand,

utilizes sugarcane as a main source of biofuels. Sugarcane produces 662 gallons of ethanol per acre per year. A gallon of ethanol is equivalent to 0.7 gallon of gasoline (mileage basis) consumption of the car [40].

The world pumped about 564 million more tons (512 million metric tons) of carbon into the air in 2010 than it did in 2009. That's an increase of 6 percent. That amount of extra pollution eclipses the individual emissions of all but three countries - China, the United States and India, the world's top producers of greenhouse gases.

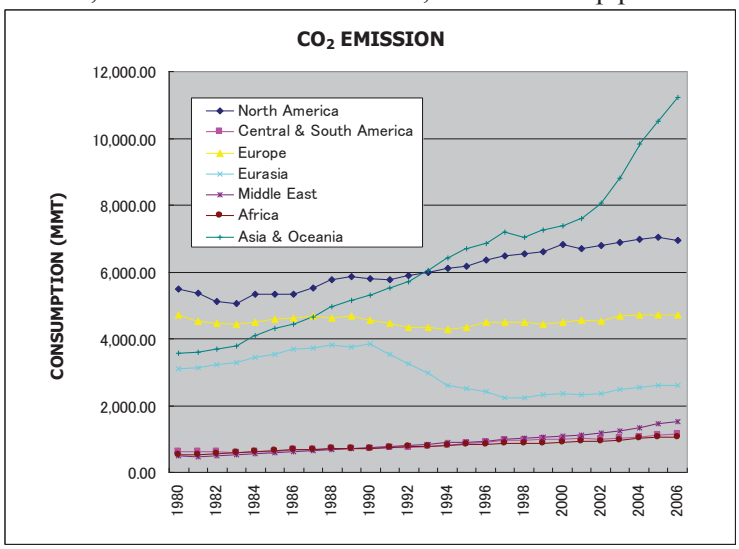

Fig. 8 World CO2 emissions from the consumptions and flaring of fossil fuels, 1980-2006.

Agriculture also contributed CO_2 emission. Agriculture directly releases into the atmosphere a significant amount of CO_2, methane (CH_4), and nitrous oxide (N_2O), amounting to around 10-12 percent of global atmospheric greenhouse gas emission annually [41]. Of global anthropogenic greenhouse gas emission in 2005, agriculture accounted for about 60 percent of N_2O and about 50 percent of CH_4, both of which have far greater global warming impact than CO_2. N_2O emission are mainly associated with nitrogen fertilizer and manure applied to the soils, as fertilizer are often applied in excess and not fully utilized by crops causing the surplus is lost to the atmosphere. Fermentative digestion by ruminant livestock also contributes to methane emissions, as does cultivation of rice in flooded condition [42]. If indirect contributions (e.g. land conversion to agriculture, fertilizer production and distribution, and farm operations) are factored in, it is estimated that the contribution of agriculture could be as high as 17-32 percent of global anthropogenic emission. In particular, land use change, driven by industrial production method, accounts for more than half of the total agricultural emissions. Conventional industrial agriculture is also heavily reliant on fossil fuels. The manufacture and distribution of synthetic fertilizers contributes a significant amount of greenhouse gas emissions, between 0.6-1.2 percent of the world's total emissions [43]. This is because the production of fertilizers is energy intensive and emits CO_2, while nitrate production also generates N_2O.

6. Summary

In general view, agriculture in develop countries after the industrial revolution, has tended to favor increase in energy input through the use of larger agricultural machines. Despite its negative societal and environmental implications, it has secured an adequate food supply for a rapidly increasing human population. In western countries, sustainable agriculture was adapted to reduce the environmental impact of agricultural production but global agricultural workforce continued to shrink that farm workers are responsible for greater areas of land for cultivation thus they opt to use larger and heavier equipments.

Industrial development leads to a huge increase in fossil fuel consumption and CO_2 emission, causing a dramatic increase in atmospheric CO_2 concentration. The increase is believed to be responsible for a significant rise in global temperature and has been linked to global warming. Climate change are the main reasons that increases the occurrence and intensities of natural calamities such as long drought, strong cyclone and hurricane, floods, rise in sea level, melting of arctic and even earthquake and tsunamis.

We strongly suggest that effective utilization of fundamental science and improved global governance to better management of food, water, energy security, ecosystem services and climate change for the estimated 9 billion people likely to be living on Earth in 2050. A key is improved communication between the scientific community which can provide scientific facts and solutions, the public, who need to better understand why and

how changes are necessary, and the government, which has at time been slow to embrace scientifically based solutions.

Acknowledgement

The authors gratefully acknowledge Japan Student Service Organization (JASSO) for the financial support extended in this research.

References

[1] Kyoto Protocol. Kyoto Protocol to the United Nations Framework Convention on Climate Change, 1997.
[2] Findlay, A. M. and Hoy, C.. Global population issues: towards a geographical research agenda, *Applied geography*, Vol. 20, No. 1, pp. 207-219, 2000.
[3] Cohen, J.E.. The human population: next half century, *Science*, Vol. 302, No. 5648, pp. 1172-1175, 2003.
[4] Fisher, G. and Heilig, G. K.. Population momentum and the demand on land and water resources, *Philosophical Transactions of the Royal Society of London. Series B: Biological Sciences*, Vol. 352, No. 1356, pp. 869-889, 1997.
[5] Furedi, F.. *Population and Development*, Cambridge: Polity, 1997.
[6] McNicoll, G. The United Nation long range population projections. *Population and Development Review*, Vol. 18, pp. 333-340, 1992.
[7] Population Reference Bureau. *Population Today*, Population Reference Bureau, Washington, DC, 1998.
[8] United Nations. *The sex and age distribution of the world populations: The 1996 revisions*. United Nations, New York, 1997.
[9] Current world population (ranked). Available: http://www.geohive.com/earth/populationl.aspx Retrieved 2011-10-25
[10] Gambrell, *J. Asia to Africa, '7 billionth babies celebrated'*, Associated Press, 2011. Available: *http://news.yahoo.com* (accessed 11.01.11)
[11] Global Agriculture towards 2050. High level expert forum. How to feed the world 2050, Rome, October 12-13, 2009.
[12] Harris, J.M. and Scott, K.. Carrying capacity in agriculture: global and regional issues, *Ecological Economics* ,Vol. 29, pp. 443-461, 1999.
[13] Chipanshi, A. C., et. al.. Vulnerability assessment of maize and sorghum crops to climate change in Bostwana, *Climate Change*, Vol. 61, pp. 339-360, 2003.
[14] Mohandrass, S. et. al.. Rice production in India under the current and future climate. In R.B. Mathews, M.J. Kroff, D. Bachelet and H.H. van Laar, eds. Modeling the impact of climate change on rice production in Asia, pp. 165-181. United Kingdom, CAB International, 1995.
[15] Peng, S., et. al.. Rice yield decline with higher night temperature ffom global warming. In E.D. Redona, A. P. Castro and G. P. Llanto, eds. Rice integrated crop managemet: Towards a rice check system in the Philippines, pp.46-56. Philrice, Nueva Ecija, Philippines.
[16] Ferrero, A., Nguyen and V. N.. The sustainable development of rice-based production system in Europe, *IRC Newsl*., Vol. 54, pp. 115-124, 2004.
[17] Matsushima, S. and Tsunoda, K.. Analysis of developmental factors determining yield and application of yield prediction and culture improvement of lowland rice XLV. Effects of temperature and its daily range in different growth stages upon the growth, grain yield, and constitutional factors in rice plants. *Proc. Crop Sci. Soc*, Vol. 26, pp. 243-244, 1958.
[18] Weisz, P. B.. Bad choices and constraints on long-term energy supplies. *Phys. Today* , Vol.57, No. 7, pp. 47-52, 2004.
[19] Energy Information Administration. *Annual Energy Outlook: With projection to 2025*, Washington, DC, 2004.
[20] Vorholz, F.. Greenfuels, Deutschland 2, 7, 2006.
[21] Energy Policy Act. *Title XV (Ethanol and Motor Fuels), Subtitle A (General Provisions), Section 1501*, Washington, DC, 2005.
[22] Mason, M.. A look behind trend data in industrialization. *Global Environmental Change* Vol.7, No.2, pp. 113-127, 1997.
[23] Robbins, P.. TNCs and global environmental change, *Global Environmental Change*, Vol. 6, No. 3, pp. 235-244, 1996.
[24] UNCTC. *Climate Change and Transnational Corporations*, United Nations, New York, 1992.

[25] Intergovernmental Panel on Climate Change (IPCC), Climate Change 2007: The physical science basis. Contribution of the working group I to the fourth assessment report of the PICC. Available: *Htpp//www.ipcc.ch (2007)*.

[26] Fearnside, P.M.. Saving tropical forests as a global warming countermeasure: an issue that divides the environmental movement, 2001.

[27] REN 21. Renewable Energy Policy Network for the 21st Century. Renewables 2011: Global status report. pp. 17, 2011.

[28] Turcotte, D. L. and Schubert, G.. *Geodynamics (2nd ed.)*, Cambridge University Press, Cambridge, England, UK, 2002.

[29] Glassley W. E.. *Geothermal energy: Renewable energy and the environment*. CRC Press, 2010. Han, X. and Chatterjee. Impacts of growth and structural changes on carbon dioxide emissions of developing countries, *World Development* , Vol. 25, pp. 395, 1997.

[30] REN 21. Renewables 2010 Global Status report, 2010.

[31] Global carbon budget, 2009. Available:Igmacweb.env.uea.ac.uk.

[32] Gerlach, T. M.. Present-day CO_2 emission from volcanoes, *Eos, Transactions American Geophysical Union* , Vol. 72, No. 23, pp. 249-255, June 4, 1991.

[33] http://en.wikipedia.org/wiki/Ozone_depletion.

[34] Climate Change. Working group I: The scientific basis, *Intergovenmental Panel on Climate Change Group I*. 2001. Chapter 6.4 Statospheric Ozone, 2001.

[35] Grossman, G., Krueger, A.. Economic growth and the environment, *Quarterly Journal of Economics* Vol. 110, pp.353-77, 1995.

[36] Shandra J. M., London, B., Whooley, O. P. and Williamson J. B.. International Non-governmental Organizations and carbon dioxide emission in the developing world: A quantitative, cross-national analysis. *Sociological Inquiry*, Vol. 74, NO. 4, 2004.

[37] Kuznet, S.. *National income and capital formation: A preliminary report*, Arno Press, New York, 1975.

[38] MED. *The New Zealand Energy Strategy to 2050-Powering our Future*, Ministry of Economic Development, 2007.

[39] Packer, M.. Algal capture of carbon dioxide; biomass generation as a tool for greenhouse gas mitigation with reference to New Zealand energy strategy and policy, *Energy Policy* , Vol. 37, pp. 3428-3437.

[40] Baruch, J. J.. Combating global warming while enhancing the future. *Technology in Society*, Vol. 30, pp. 111-121, 2008.

[41] Smith, P., Martino, D., Cai, Z., Gwary, D., Janzen, H., Kumar, P., McCarl, B., Ogle, S., O`Mara, F., Rice, C., Scholes, B. and Sirotenco, O.. Agriculture. pp. 497-540, 2007. In B. Metz, O.R. Davidson, P.R. Bosch, R. Dave and L.A. Meyer (eds.). *Climate Change 2007: Mitigation. Contribution of Working Group III to the Fourth Assessment Report of the Intergovernmental Panel on Climate Change*, Cambridge University Press, Cambridge, UK and New York, USA.

[42] Ching, L. L., Eduards, S., Scialabba and N. E.. *Climate change and food system resilience in Sub-Saharan Africa. 183-197*, Food and Agriculture Organization of the United Nations, Rome, 2011.

[43] Bellarby, J., Foereid, B., Hastings, A., and Smith, P.. *Cool Farming: Climate impacts of agriculture and mitigation potential*, Greenpeace International, Amsterdam, 2008.